MICROWAVE CIRCUIT ANALYSIS OF MULTI TRANSMON QUBIT SYSTEM

MSC ELECTRICAL ENGINEERING THESIS

MICROWAVE CIRCUIT ANALYSIS OF MULTI TRANSMON QUBIT SYSTEM

MSC ELECTRICAL ENGINEERING THESIS

Jonathan GNANADHAS

MSc in Electrical Engineering, Signals and Systems

Thesis Supervisors:

prof. dr. A. Yarovoy	Delft University of Technology
dr. ir. S.N. Nadia	QuTech, TNO

Thesis Committe:

prof. dr. A. Yarovoy	Delft University of Technology
prof. dr. L. Dicarlo	Delft University of Technology
prof. dr. B.J. Kooij	Delft University of Technology

CONTENTS

1

INTRODUCTION

1.1. BACKGROUND OF RESEARCH

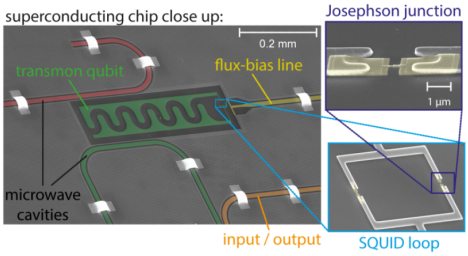

Figure 1.1: Electron microscope image of a transmon qubit [1]

The quest to design a realizable quantum computer is a dream for many for the past few decades. Quantum computing is different from the classical computer, which is based on the principle of quantum superposition and entanglement. At a moment, a quantum computer that has each qubit designed to be a 2 state system, having n qubits, can be in any state that is a superposition of 2^n states. This creates a potential to perform large scale computations in a short period of time, compared to the classical computer, which is always in one of the 2^n state. It has been successfully demonstrated to solve problems such as prime factorization using Shor's algorithm [2], Grover search and Deutsch–Jozsa quantum algorithms [3], on a quantum computer.

At the moment, one of the promising designs is the transmon qubit [4], which is a superconducting qubit is the focus of this work. Quantum systems built with atomic systems such as nuclear or electron spins provide good coherence time, since they are weakly coupled to the environment. However, this presents a problem in manipulation and control. The superconductor qubits on the other hand has a relatively shorter coherence time, but presents excellent coupling with the external environment [5]. This

can be exploited for measurement and control. In addition, the scalability of the superconducting qubits offers a significant advantage over other designs. The transmon qubit is constructed by using superconducting material placed on a dielectric material as the substrate. The device is fabricated by spluttering the superconducting material on top of the dielectric substrate, according to the intended Coplanar Waveguide (CPW) design and the structure is typically enclosed in a metallic structure that is grounded. A transmon qubit image taken by a electron microscopy is shown in figure 1.1. Since the materials and design components that are used to construct the quantum device, can be analyzed in classical electrodynamic theory, one can analyze several parameters in classical domain about the quantum device. For example, the qubit can be thought of as an anharmonic parallel LC oscillator and the capacitance can be modified and designed according to the geometry of construction. By varying the capacitance across the junction, one can design range of frequency of operation of the qubit, along with the inductance exhibited by the Josephson's junction. A resonator in a qubit chip is used to couple two qubits to each other, also used in measurement circuitry. The resonator can be modelled as an open circuited transmission line or short circuited transmission line, which is capacitively coupled in the circuitry. This can be entirely explained by classical electrodynamic theory for its operating parameters such as characteristic line impedance and resonant frequency.

1.2. RESEARCH PROBLEM

In order to analyze and design different components of our quantum chip, we need to understand the circuitry. In a multi qubit system, the interaction between the different components such as qubits and resonators needs to be analyzed carefully. It is of importance to analyze the interaction of these components with each other in order to design the parameters such as loaded resonator frequencies, coupling quality factors in the qubit system. This problem of understanding the interaction of circuit components such as resonators and computing their resonances is to be a focus of this work.

The external quality factor of the readout resonator that is used to measure the state of the qubit needs to be targeted accurately. This is important because the external quality factor determines the rate and resolution at which the measurements can be done. This problem statement calls for an understanding of the circuit parameters that influences the external quality factor of the readout resonator, has also been treated in this work.

1.3. RESEARCH APPROACH

The research approach to solve the problems faced is to analytically model the circuitry and also build an equivalent FEM 3D model. Using the FEM model, one can extract and target the desired operating parameters from the equivalent physical model. Figure 1.2 shows a 3D simulation model of a starmon qubit chip, which was designed, fabricated and measured prior to this thesis work. To construct a 3D FEM model of a transmon qubit, one need to model the superconductor material, that is done by using an equivalent surface impedance model. On applying this film property on the CPW construction, one can model the physical chip as an FEM model. However, FEM 3D simulations of

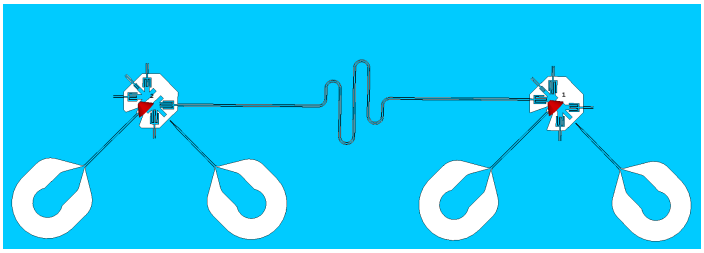

(a)

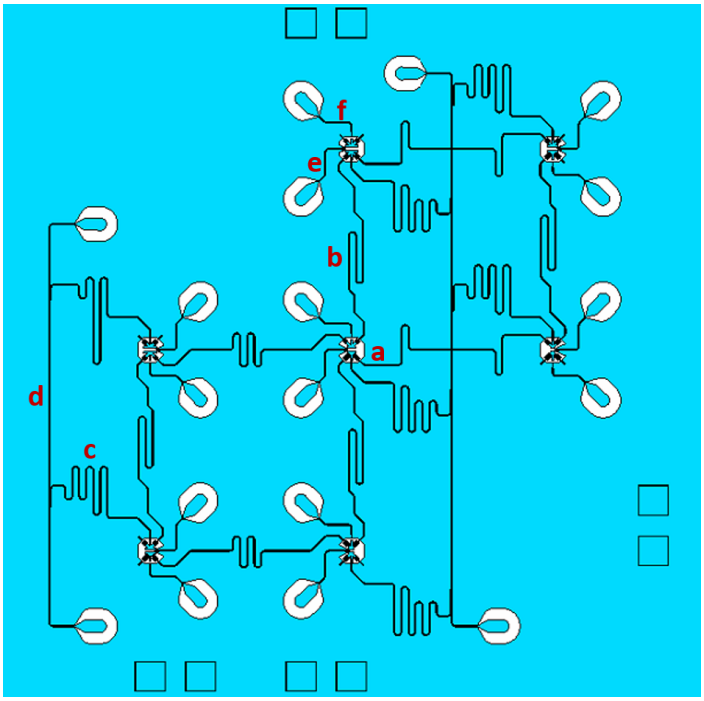

(b)

Figure 1.2: a. FEM simulation model of a 2 qubit system [6]. b. FEM simulation model of a Surface 7 layout [6] used in DiCarlo lab. The part marked with "a" is a qubit. "b" is the resonator that couples a qubit to another qubit. "c" is the resonator that is used to readout the state of the qubit. "d" is the feed line that is part of the qubit measurement circuitry, which is connected to the external measurement circuitry, "e" is the flux drive line, which is used to exert flux on the SQUID. "f" is the microwave drive line.

large qubit chips can be time consuming. Hybrid simulations involving a FEM model of a qubit unit cell and interconnecting them with circuit models of resonators and transmission lines was used to understand the loaded resonances of the bus resonators as well as to analyze the external quality factor of readout resonators for a qubit system. CST was the electromagnetic simulation tool primarily used in this thesis work, both for FEM and circuit simulation. The quantum chips reported in the thesis are all designed, fabricated and measured by QuTech (DiCarlo Lab) and Intel prior to this thesis project.

2

Components and Circuit Quantum Electrodynamics of a Transmon Qubit

The transmon qubit is primarily constructed with components such as Josephson's junction across a pair of charging islands and resonators built around it, used for interaction. The Josephson's junction along with the charging islands form a LC oscillator (anharmonic by construction), whose quantum states can be defined and constructed. This forms the "qubit" and the remaining circuitry such as capacitively coupled resonators, are built around it. These circuits built around a qubit are used to measure or to create an interaction with another qubit. This chapter focuses on explaining several basic components that's used in the construction and the circuit quantum electrodynamics of the transmon qubit.

2.1. Josephson's Junction

The Josephson's junction is used to provide a nonlinear inductor for the transmon qubit. It is a quantum mechanical effect in which two superconductors separated by a thin layer of insulator, allows the Cooper-pair electrons to tunnel across the junction. This flow of Cooper pair electrons constitute a supercurrent, which is described by the following equations [7].

$$I_J = I_0 sin(\delta)$$

$$V = \frac{\phi_0}{2\pi} \frac{d\delta}{dt}$$

where I_0 is the critical current parameter across the junction, V is the voltage cross the superconducting junctions, δ is the phase difference between the wave function of

the superconducting state on the left and right superconducting material and $\phi_0 = \frac{h}{2e}$ is the flux quantum. A derivation of the above equations is described in [8]. On differentiating I_J with respect to time and using the relationship of V and $\frac{d\delta}{dt}$, one can arrive at the relationship

$$\frac{dI_J}{dt} = \frac{I_0 2\pi V}{\phi_0} cos(\delta)$$

This relationship is of the similar form of the classical inductance, which is given by the current and voltage relationship $V = L\frac{dI}{dt}$. On defining a nonlinear inductance

$$L_J = \frac{\phi_0}{2\pi I_0 cos(\delta)}$$

it can be seen that the change in current with respect to time is non linearly related to the voltage across the superconducting sides by the inductance L_J. Furthermore, it can be seen that as δ tends to zero, the inductance is minimum, whereas, as the δ tends to $\frac{\pi}{2}$, the inductance becomes maximum. This can be used as a design parameter, i.e., by changing the flux across the junction, the inductance can be changed or tuned. This is necessary to tune the qubit to operate at a certain frequency.

The energy stored in the junction can be computed by

$$E(t) = \int_t^{-\infty} I(t)V(t)dt$$

If the Josephson's energy defined as $E_J = \phi_0 I_0$, then

$$E(t) = -E_J cos(\frac{2\pi\phi(t)}{\phi_0})$$

The non-linearity of the inductance provided by the Josephson's junction is essential to the qubit design. The non-linearity allow the Hamiltonian of the LC circuitry at the junction to be non-degenerate. This allows the energy levels of each state to be measured distinctly.

2.2. SQUID

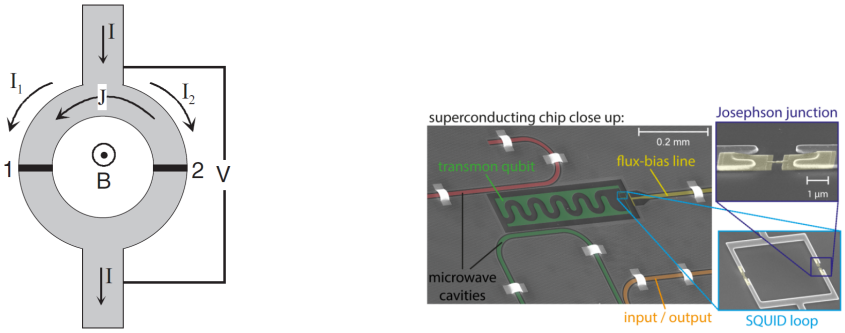

(a) (b)

Figure 2.1: a. A schematic of a SQUID, with two Josephson junction at both limbs, from [10]. b. Electron microscope view of a transmon qubit SQUID loop [1] .

Superconducting QUantum Interference Device (SQUID) is built using the principles of Josephson tunneling and flux quantization. It is constructed by a superconducting ring with Josephson's junctions (DC SQUID) at both limbs, shown in figure 2.1. The supercurrent that flows through the ring is limited by the Josephson's junctions and is limited to the sum of the critical currents through the junctions. The interfering superconducting wave function in both the limbs of the SQUID causes a magnetic flux, that modulates with a period of a flux quantum $\Phi_0 = \frac{h}{2e}$, where h is Planck's constant and e is the charge of an electron [10]. On applying an external field, the total magnetic flux through the SQUID can be represented as Φ, which has contributions due to the external field and the circulating current. If the phase differences at both the junctions is ϕ_1 and ϕ_2, n is an integer, then they are related as

$$\phi_2 - \phi_1 = \frac{2\pi}{\Phi_0}\Phi + 2\pi n$$

The phase difference δ defined here is the gauge invariant phase difference between the macroscopic wave function of the two superconductors across the Josephson junction. Using the external field Φ it allows the tuning of the transmon qubit to the required frequency by changing the Josephson energy, given by the relationship

$$E_J = E_{JMax}\left|\cos\left(\pi\frac{\Phi}{\Phi_0}\right)\right|$$

The Hamiltonian provided by the SQUID component can be represented for symmetric Josephson junctions across both limbs of the SQUID as [4]

$$\hat{H}_J = -E_J\cos(\hat{\phi})$$

where $\hat{\phi}$ is the gauge invariant phase difference between the wave functions of the two superconductors across the junction. However, due to fabrication techniques of date,

there could be a slight asymmetry formed at the junction. In case of asymmetric junctions, the Hamiltonian provided by the SQUID component can be written as

$$\hat{H}_J = -E_{J1}\cos(\hat{\phi}_1) - E_{J2}\cos(\hat{\phi}_2)$$

On defining an effective phase difference as $\phi = \phi_1 + \phi_2$, the Josephson energy as $E_{J\Sigma} = E_{J1} + E_{J2}$, junction asymmetry $d = \frac{E_{J2}-E_{J1}}{E_{J1}+E_{J2}}$, then the Hamiltonian can be written as [4]

$$\hat{H}_J = -E_{J\Sigma}\cos\left(\frac{\pi\Phi}{\Phi_0}\right)\sqrt{1 + d^2\tan^2\left(\frac{\pi\Phi}{\phi_0}\right)}\cos(\hat{\phi} - \phi_0)$$

where the phase ϕ_0 is given by the relationship $\tan(\phi_0) = d\tan(\frac{\pi\Phi}{\Phi_0})$. The dependence of ϕ_0 on the external field, allows an additional qubit control. However, the asymmetric junction can cause an additional qubit decay due to the flux fluctuations.

2.3. SUPERCONDUCTING QUBITS

The choice of superconductors stems from the requirement that the circuitry must have no or very minimal dissipation such that there is no energy loss. This one of the necessary condition for the preservation of the coherence [9]. Also, there must be very low noise. The requirement with the thermal noise is such that the energy 'kT' of thermal fluctuation is to be significantly less than the energy quantum $\hbar\omega_{01}$ associated with the qubit transition of 0 and 1 state. This calls for the operation of the qubit at very low temperature of 20 mK, built with superconducting material and operated at frequencies around of 5 to 20 GHz. There are various types of superconducting qubits that are discussed in [11]. In this section, first an LC quantum circuit is discussed and then a background material for transmon is discussed because in this thesis, analysis is done only with the transmon qubit type. A thorough description about transmon is discussed in [4].

2.4. LC QUANTUM DEVICE

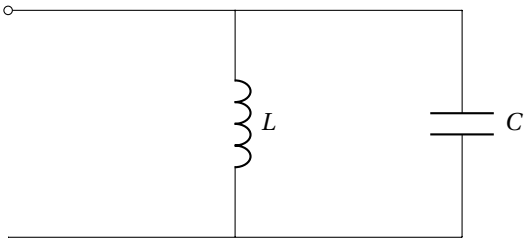

Figure 2.2: Parallel LC circuitry

The quantum description of a superconducting LC oscillator is briefly described in this section. The basic circuitry of a transmon qubit is an LC circuit upon which, peripheral components are added. However, it should be noted that a nonlinear inductive

component is used in a transmon qubit. The energy stored by a capacitor of capacitance C that contains a charge Q is given by

$$U_C = \frac{Q^2}{2C}$$

The energy stored by an inductor of inductance L, having the branch flux ϕ is given by

$$U_L = \frac{\phi^2}{2L}$$

where ϕ and Q are canonical variables obeying the commutation relationship $[\phi, Q] = i\hbar$. The Hamiltonian of the LC oscillator circuit can be written as

$$\hat{H} = \frac{\hat{\phi}^2}{2L} + \frac{\hat{Q}^2}{2C}$$

If annihilation and creation operators for such a LC oscillator system are defined as

$$[c, c^\dagger] = 1$$

the flux and charge operators can be written in terms of the annihilation and creation operators as

$$\phi = \phi_{ZPF}(c + c^\dagger)$$

$$Q = \frac{1}{i} Q_{ZPF}(c - c^\dagger)$$

The Hamiltonian of the LC oscillator system can be rewritten in terms of annihilation and creation operators as

$$H = \hbar\omega_0 (c^\dagger c + \frac{1}{2})$$

where the parameters resonant frequency ω_0, zero point flux operator ϕ_{ZPF}, zero point charge Q_{ZPF} and the characteristic impedance Z_0 are given by

$$\omega_0 = \sqrt{\frac{1}{LC}}$$

$$\phi_{ZPF} = \sqrt{\frac{\hbar Z_0}{2}}$$

$$Q_{ZPF} = \sqrt{\frac{\hbar}{2Z_0}}$$

$$Z_0 = \sqrt{\frac{L}{C}}$$

The term ZPF denotes zero point fluctuation. It corresponds to the parameter values at the lowest energy that the quantum system can take.

2.5. TRANSMON QUBIT

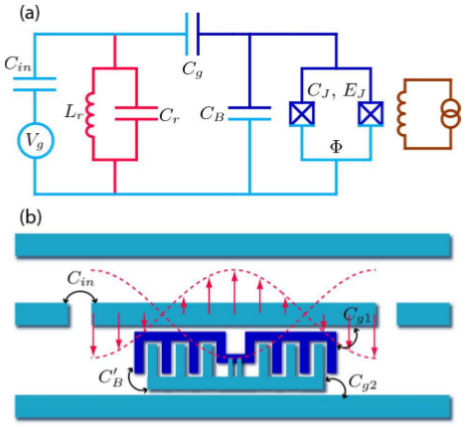

Figure 2.3: From [4] a. The equivalent circuit diagram of a transmon qubit coupled with a resonator. b. It's equivalent simplified schematic of a CPB, with a extended segment that can lead to the increase in C_g and C_B

The transmon is essentially a Cooper Pair Box (CPB) with a large capacitor in parallel such that the ratio of $\frac{E_J}{E_C}$ is large (in range of 50). A major disadvantage of the CPB design is that it is affected by the charge noise fluctuation. There is a charge insensitivity offered at the degeneracy point, but the charge offsets at the nearby charge fluctuators affects the CPB operation. This calls for an improvement in the design and the offshoot is transmon. The circuit diagram of a transmon is shown in 2.3.

It can be seen from the figure 2.3 that the transmon is constructed by LC circuit with a nonlinear inductor provided by the Josephson's junction with a charging pad, which provides the capacitance. The strategy for readout or measurement of a transmon qubit is by using a resonator, coupled with a capacitance. Also, the qubits can be coupled with each other using a resonator.

In the absence of the transmission line resonator, the Hamiltonian can be written in the form

$$H_{JC} = 4E_C(\hat{n} - n_g)^2 - E_J(\phi_{ext})cos\hat{\phi}$$

which is the Hamiltonian of the CPB. The effective offset charge n_g is given by

$$n_g = \frac{Q_r}{2e} + \frac{C_g V_g}{2e}$$

where V_g and C_g are the gate voltage and capacitance, whereas Q_r is the environment induced charge offset. However, the main difference between the transmon and the CPB is the addition of large capacitance seen from the junction. This is done by adding the capacitance C_B and C_G, shown in figure 2.3. This effectively leads to a smaller charging energy compared to the Josephson energy, i.e., $E_C << E_J$. The charging energy E_C is

given by

$$E_C = \frac{e^2}{2C_\Sigma}$$

where C_Σ is the effective capacitance seen across the junction, i.e., in figure 2.3, $C_\Sigma = C_J + C_B + C_g$. C_Σ might not be as simple as to be calculated in figure 2.3, for a qubit chip with multiple qubits. The capacitance across the junction for each individual qubits needs to be extracted through circuit analysis.

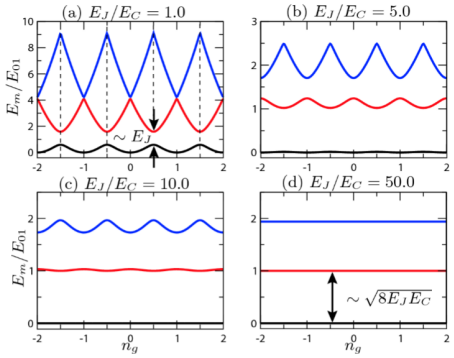

Figure 2.4: From [4] The Eigen Energies E_m of the Hamiltonian for m = 0,1,2, for different ratios of $\frac{E_J}{E_C}$ as a function of effective charge offset n_g.

It can be observed from Figure 2.4 that the there is a dependency of the anharmonicity and charge dispersion on the ratio $\frac{E_J}{E_C}$. Anharmonicity is important factor for the selective control of the transitions and is depicted in figure 2.4. The charge dispersion deals with the qubit sensitivity to the charge noise.

On the CPB design, the qubit is operated at specific sweet spots. From figure 2.4 a, it can be observed that by operating the qubit at $n_g = 1/2$, the sensitivity to noise is reduced. A large fluctuation can drive the system out of the sweet spot. However, it can be observed from Figure 2.4 b,c,d, that by increasing the ratio of $\frac{E_J}{E_C}$, there is an exponential decrease in the charge dispersion. This enables a qubit transition frequency that is stable with respect to charge noise. This gain in charge noise stability is a tradeoff with the anharmonicity. It is necessary to have sufficient anharmonicity to maintain the two level system and it dictates the lower bound on the duration of the control pulses. It can be noted that there is a reduction in anharmonicity in the transmon design with respect to CPB. However, this reduction in anharmonicity is by a weak power law, whereas the gain in the reduction of noise sensitivity is an exponential gain. If by definition, the absolute and relative anharmonicity is defined as

$$\alpha \equiv E_{12} - E_{01} \qquad \alpha_r \equiv \frac{\alpha}{E_{01}}$$

An analysis on the anharmonicity at $n_g = \frac{1}{2}$ is explained in [4]. It can be found by using perturbation theory, the anharmonicity asymptotically behaves as

$$\alpha \approx -E_C \qquad\qquad \alpha_r \approx -\sqrt{\frac{8E_J}{E_C}}$$

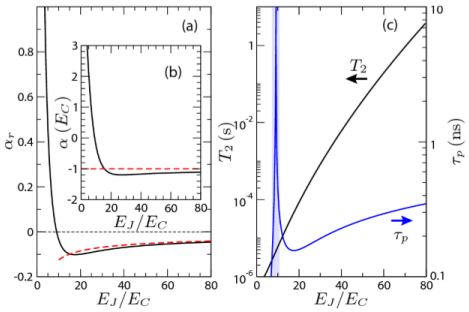

Figure 2.5: From [4] a. b are the absolute and relative anharmonicity. The solid and dashed lines represents the results calculated from exact solutions and pertabative results. It can be noted that a certain ratio of $\frac{E_J}{E_C}$, the anharmonicity crosses zero, or the antiharmonic barrier. c. Plot of Minimum pulse duration and dephasing time T_2 due to charge fluctuations. It can be noted that T_2 increases as ratio $\frac{E_J}{E_C}$ increases.

It can be found that the half wavelength resonator, coupled with the transmon qubit, can be modelled as a parallel LC circuitry. The equivalent circuit of a typical isolated transmon qubit circuitry is shown in Figure 2.3. On coupling the CPB structure to a resonator, coupled through a capacitive gate, one obtains the Jayes-Cummings Hamiltonian [4], which is of the form

$$H_{JC} = 4E_C(\hat{n} - n_g)^2 - E_J(\phi_{ext})cos\hat{\phi} + \hbar\omega_r \hat{a}^\dagger \hat{a} + \hbar g\hat{n}(\hat{a} + \hat{a}^\dagger)$$

where the terms $\hat{a}$ and $\hat{a}^\dagger$ are annihilation and creation operators of the resonator field, $\hbar\omega_r \hat{a}^\dagger \hat{a}$ is the energy of the resonator field and the term $\hbar g\hat{n}(\hat{a} + \hat{a}^\dagger)$ represents the coupling between the resonator and the qubit. It should be noted that the factor g is termed as the "coupling strength" between the transmon qubit and the resonator. It can be derived that the factor g is given by

$$g = 2\beta V^o_{rms}$$

where V^o_{rms} is the zero point voltage and β can be found to be a voltage ratio given by the ratio of the voltage on the capacitively coupled resonator to the voltage across the junction.

Qubit operations are carried out by using microwave pulses and the readout is done by the measurement of the amplitude and phase of the transmitted signal. The coupling between the resonator and the qubit provides the possibility to readout the state of the qubit. The state of the qubit is readout dispersively by detuning the resonator resonance

from the qubit resonance. If the detuning is larger than the coupling, then the Hamiltonian of a two level system [4] can be written as

$$\hat{H}_{eff} = \frac{\hbar(\omega_{01} + \chi_{01})}{2}\hat{\sigma_z} + \hbar(\omega_r - \frac{\chi_{12}}{2} + \chi\hat{\sigma_z})\hat{a}^\dagger\hat{a}$$

If detuning is represented as $\Delta = \omega_q - \omega_r$ i.e, difference between the qubit frequency and the resonator's resonance, then it can be shown that $\chi = \frac{g^2}{\Delta}$. On observing the Hamiltonian, it can be observed that the qubit is shifted by χ, known as Lamb's shift and the resonator experiences a shift $\omega_r \pm \chi$. The two level approximation involves restricting the transmon to the ground state and first excited state in the hilbert space. The terms $\hat{\sigma_x}$ and $\hat{\sigma_z}$ in the Hamiltonian are the pauli operators. It can be shown that the dynamics of the qubit interaction with the resonant cavity can be described by a strongly coupling regime, i.e., $g >> \kappa, \gamma'$. γ' describes the incoherent interaction with the continuum and κ describes the incoherent field damping in the cavity or its also known as the decay rate. In the following chapters a starmon qubit layout [6], which was designed and experimentally tested prior to this thesis project is used to analyse the bus resonator frequency and coupling quality factor.

3

CLASSICAL ELECTRODYNAMICS ANALYSIS OF A TRANSMON QUBIT

The 3D model of a transmon qubit can be characterized in the classical domain and FEM simulations can be performed to extract certain parameters. For instance, the charging energy E_c is given by (also explained in the previous chapter)

$$E_C = \frac{e^2}{2C_\Sigma}$$

If the capacitance across the junction can be computed, then the charging energy can be computed. Similarly, the Hamiltonian of two level system of a transmon coupled with a resonator given by [4]

$$\hat{H}_{eff} = \frac{\hbar\omega'_{01}}{2}\hat{\sigma_z} + \hbar(\omega'_r + \chi\hat{\sigma_z})\hat{a}^\dagger\hat{a}$$

where ω'_r, the resonance frequency of the resonator is of interest. Determination of the resonant frequency of a open circuited transmission line can be done in classical electrodynamic theory. The resonators that is used for coupling or readout are constructed using CPW transmission lines and the resonant frequency can be calculated by calculating the inductance and capacitance of the line, along with the length of the line [13]. However, from theoretical calculation, the capacitance seen across the edges of the resonator is not easy for a large circuitry with possible inductive components. But it can be computed by constructing the layout and then exciting the circuit and readout by using S parameters. By classical electrodynamic theory, several components such as capacitances for coupling, loaded resonance frequencies of resonators, line impedance of transmission lines, etc., can be computed. These parameters serve as design parameters and it is essential to model them correctly to target the design correctly in a physical system. In this chapter, a description of the surface impedance used to model the superconductor, inductance, capacitance due to the fields that propagate in the CPW structures are discussed using classical theory.

3.1. SURFACE IMPEDANCE

In this section, the surface impedance is explained from exploring the Maxwell's equations. The FEM simulation requires the superconductivity to be modelled as part of the material properties. The superconductivity can be modelled in the tool by using tabulated surface impedance, depending on the material. In this section, we explore the derivation of the surface impedance from the Maxwell's equations [12].

The field that is propagating is assumed to be of a complex form, i.e., $\vec{E} = Ee^{j\omega t}$. The curl of the magnetic field can be written as

$$\nabla \times \vec{B} = (\mu\sigma + j\omega\mu\epsilon)\vec{E}$$

This is valid when $\vec{J} = \sigma\vec{E}$. For a source-less medium

$$\nabla \times \vec{E} = -\frac{\partial \vec{B}}{\partial t}$$

On taking a curl on both sides of the equation leads to

$$\nabla^2\vec{E} = \mu\sigma\frac{\partial \vec{E}}{\partial t} + \mu\epsilon\frac{\partial^2\vec{E}}{\partial t^2}$$

Considering a wave of the structure $\vec{E} = Ee^{j\omega t}$

$$\nabla^2\vec{E} = j\mu\sigma\omega\vec{E} - \mu\epsilon\omega^2\vec{E} = k^2\vec{E}$$

on ignoring the displacement current, k can be written as

$$k = \sqrt{\mu\sigma\omega j}$$

If the propagation is only along one of the axis, lets say z, then

$$\frac{\partial^2\vec{E}}{\partial z^2} = k^2\vec{E}$$

which is a wave equation and is seen to be transverse in z. A solution of such an equation would be of the form

$$\vec{E} = E_0 e^{-kz}$$

The current that is produced by this field can be calculated by integrating the current density over the direction of propagation of this wave.

$$I = \int_0^\infty J dz$$

which can be written as

$$I = \int_0^\infty \sigma\vec{E} dz$$

or

$$I = \frac{\sigma \vec{E}}{k}$$

Considering the k to be of the a complex number scaled by a coefficient, the electric field and the current can be related to the impedance term

$$\vec{E} = Z_s I \qquad\qquad Z_s = (R_s + j\omega L_s)$$

where R_s is the surface resistance and L_s is termed as the surface inductance offered by the superconductor. The R_s is caused by the losses caused due to the electrons that are not cooper pairs, impurities etc. The L_s can be got for a thin film superconducting CPW structure as $\mu_0\lambda$ [16], where λ denotes the effective magnetic field penetration depth. If the conductivity can be written as $\sigma = \sigma_1 - j\sigma_2$, the permeability of the superconductor can be taken up as μ_0, the surface impedance in local limits can be written as

$$Z_s = \sqrt{\frac{j\omega\mu_0}{\sigma_1 + j\sigma_2}}$$

The components of the conductivity for superconductor can be calculated from [14].

3.2. FIELDS, INDUCTANCE AND CAPACITANCE OF CPW STRUCTURE

The technology used to implement the transmon qubit is CPW on a silicon dielectric. A typical CPW structure is shown in figure 3.1a. Specific components in a qubit system such as the resonators, feed line have a uniform CPW structure, which have electrical parameters such as capacitance and inductance per unit length can be predicted analytically. Insight on calculating parameters such as inductance and capacitance for CPW structures can be found in [16], [17] and [18]. A description about the structure of the fields can be found in [17]. This section explores the inductance and capacitance offered per unit length due to the fields propagating in the CPW structure.

3.2.1. GEOMETRICAL INDUCTANCE AND CAPACITANCE

In this section, we discuss the parameters for the CPW structure which is infinitely long, mounted on an infinitely large (h is infinite) dielectric material. The CPW dimension be such that the length of the center conductor is taken as 2a and the distance between the center conductor and the ground plane be taken as 2b. If the conductors are infinitely thin, then by conformal mapping technique [16], [17] the capacitance and inductance can be found. The capacitance per unit length can be deduced as

$$C = \frac{1+\epsilon_r}{2}\epsilon_0 \frac{4K(k)}{K(k')}$$

The inductance per unit length can be deduced to be

$$L = \mu_0 \frac{K(k')}{4K(k)}$$

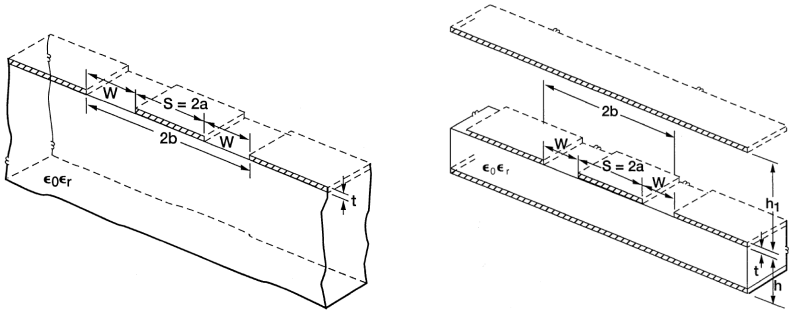

(a) (b)

Figure 3.1: CPW Geometry. a. A CPW structure from [17], with a central conductor width S, central conductor to ground plane width of W and thickness t, placed on a dielectric material of permittivity $\epsilon = \epsilon_0\epsilon_r$. b.Conductor Backed CPW.

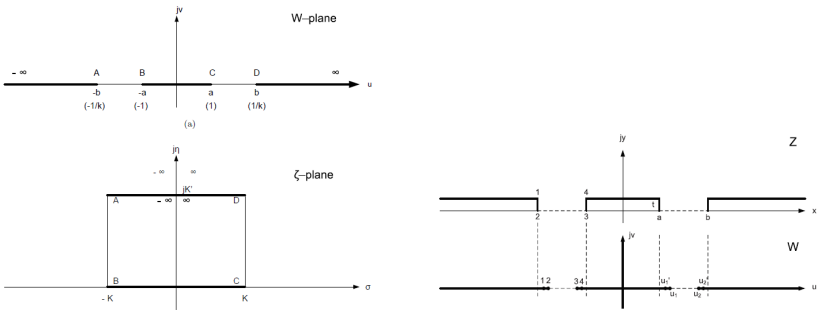

(a) (b)

Figure 3.2: CPW Conformal Mapping [16]. a. CPW Conformal Mapping of an infinitely thin CPW line. b. CPW Conformal Mapping of thickness t.

where K is an elliptic integral of first kind.

$$K(k) = \int_0^1 \frac{1}{\sqrt{(1-x^2)(1-k^2x^2)}} dx$$

$$K(k') = \int_1^{\frac{1}{k}} \frac{1}{\sqrt{(x^2-1)(1-k^2x^2)}} dx$$

However, although the thickness (t) of the CPW lines are very small in the orders of 200 nm typically, and the width (2a) of the CPW center strip is of order 12 um, a more relevant expression can be derived for thickness t « a, as derived in [16].The CPW structure in the z plane can be transformed on the w plane as shown in figure 3.2b. It can be found that as t is very small, then if

$$d = \frac{2t}{\pi}$$

$$u_1 = a + \frac{d}{2} + \frac{3\log 2}{2}d - \frac{d}{2}\log\left(\frac{d}{a}\right) + \frac{d}{2}\log\left(\frac{b-a}{a+b}\right)$$

$$u_2 = b - \frac{d}{2} - \frac{3\log 2}{2}d + \frac{d}{2}\log\left(\frac{d}{b}\right) + \frac{d}{2}\log\left(\frac{b-a}{a+b}\right)$$

k can be defined as a function of thickness t, as $k_t = \frac{u_1(t)}{u_2(t)}$ and $k'_t = \sqrt{1-k_t^2}$. It can then be found that the capacitance per unit length and the magnetic inductance per unit length can be given by the following expression [16]

$$C = \epsilon_0 \frac{2K(k_t)}{K(k'_t)} + \epsilon_r \epsilon_0 \frac{2K(k)}{K(k')}$$

$$L = \mu_0 \frac{K(k'_{t/2})}{4K(k_{t/2})}$$

3.2.2. KINETIC INDUCTANCE

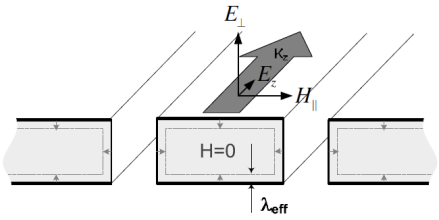

Figure 3.3: Field Components in a superconducting CPW [16]

On a superconducting CPW line, the field propagating is a Quasi-TEM with a small longitudinal component E_z. This component arises as a consequence of the magnetic field penetrates the surface of the superconductor for a depth of λ_{EFF} as shown in figure 3.3. The change in the penetrated magnetic field ($H_{||}$) with respect to time in the tangential direction (z) would give rise to the tangential electric field E_z. This can be seen by applying Maxwell's equations on the boundary. The following discussion on the kinetic inductance of a superconducting CPW can be found in [16].

The magnetic field outside the CPW is similar to the distribution for a conductor. However, it can be noted that there is an energy component pointed out by the Poynting

theorem in the direction normal to the superconducting surface due to the components E_z and $H_{||}$. The Poynting vector can be written as

$$S = \int_C (E^* \times H_{||}) dl$$

or

$$S = \int_C (E_z^* . H_{||}) dl$$

This energy is stored in an additional inductance other than the geometrical inductance provided by the dimensions of the CPW structure. The supercurrent due to Cooper pairs will carry this additional kinetic energy with is dependent on the material properties and the temperature of the environment. For a CPW made with a perfectly conducting material, it can be seen that the inductive component is only dependent on the geometrical structure. Whereas, for a superconducting material, the total inductance depends on the geometry and the kinetic inductance due to the material property. It can be written as

$$L = L_m + L_{KI}$$

Using transmission line theory, the dissipation factor and the inductive stored energy, the Poynting vector can be written as

$$\frac{1}{2} R I^2 = Re\Big(\int_C E_Z^* . H_{||} dl \Big)$$

$$\frac{1}{2} \omega L_{KI} I^2 = Im\Big(\int_C E_Z^* . H_{||} dl \Big)$$

In the previous chapter, the general case of the surface impedance was discussed. The surface impedance for a superconducting CPW $Z_S = R_S + j\omega L_S$, can be written as

$$Z_S = \frac{E_Z}{H_{||}}$$

It can be seen if a geometric factor g can be defined as

$$g = \frac{\int_C H_{||}^2 dl}{I^2}$$

Then on comparing the equations of the Poynting vector and the surface impedance model, the real and imaginary part of the surface impedance of a superconducting CPW can be written as

$$Z_S = g R_S + j\omega g L_S$$

or

$$Z_S = g R_S + g \mu_0 \lambda_{EFF}$$

The surface impedance of a superconducting CPW is the surface impedance of the general case but multiplied by a geometric factor. λ_{EFF} is the effective London's penetration depth, discussed in [16]. It is essential to determine the kinetic inductance in several component designs such as resonators, feed line, etc. The geometric factor has to be found by integrating the $H_{||}^2$ field component in a contour. The field outside the superconductive CPW is similar to a perfect electrical conductor (PEC) CPW and can be solved using Laplace equations. Approximate solutions for g is shown in [16], using conformal mapping. In dirty limits, the mean free path of electrons in the superconductors is much lesser than the magnetic penetration depth λ and the coherence length given by $\frac{\hbar v_f}{\pi\Delta(0)}$, where v_f is the Fermi velocity of the electrons. In extreme anomalous limits, where the magnetic penetration depth is less than the coherence depth, the magnetic penetration depth is given to be

$$\lambda = \sqrt{\frac{mc^2}{4\pi ne^2}}$$

where m is the mass of the conduction electron, e is the charge of the electron and n is the density of the conduction electrons.

3.3. HALF WAVELENGTH RESONATORS

Half wavelength resonators form an important component of a qubit. The readout and bus resonators can be modelled as half wave resonators. The impedance model of a half wavelength is discussed in this section and is useful to understand it. A half wavelength resonator can be modelled as open circuited transmission line. The input impedance of an open circuited transmission line can be written as

$$Z_{in} = Z_0 cot(\alpha + j\beta l)$$

This can be further expanded as

$$Z_{in} = Z_0 \frac{1 + j\alpha l tan(\beta l)}{\alpha l + j\tan(\beta l)}$$

where α is the attenuation constant, which is much less than 1 or tends to 0 for superconductors and β is propagation constant. If α can be rewritten as $\frac{\beta l}{2Q_i}$, then the above expression can be formulated as

$$Z_{in} = Z_0 \frac{2Q_i - j4Q_i^2 tan(\beta l) + j(\beta l)^2 tan(\beta l) + 2Q_i \beta l tan(\beta l)}{(\beta l)^2 + (2Q_i \tan(\beta l))^2}$$

Since Q_i is large, the above expression can be approximated as

$$Z_{in} \approx Z_0 \frac{1 - j2Q_i tan(\beta l) + \beta l tan(\beta l)}{2Q_i (tan(\beta l))^2}$$

or

$$Z_{in} \approx Z_0 \frac{-j}{tan(\beta l)}$$

The input impedance of a half wavelength resonator varies as a trigonometric function tan, in case of a high internal quality factor. This implies that there is a minimal loss inside the resonator per unit cycle. Since the material is made up of superconducting material and assuming negligible losses in terms of radiation and dielectric losses, one can assume this relationship holds in the transmon qubit resonator design.

3.4. STABILITY OF SUPERCONDUCTIVITY SURFACE IMPEDANCE MODEL

FEM simulations on superconductors involve constructing ports (discrete or waveguide) and modelling the superconductor with a tabulated surface impedance based on film properties. The electromagnetic FEM solver iteratively computes the S parameters. For the simulations to be stable, it is imperative to understand the stability of the model, such that the simulations can be successfully be performed. If the model is not stable, then the scattering parameters or S parameters would have difficulty in convergence. The surface impedance model of a superconductor consists of a resistive and a inductive component. The resistive component in the surface impedance is found to be very less compared to the inductive component and can cause instability. Hence, an analysis on the stability is necessary.

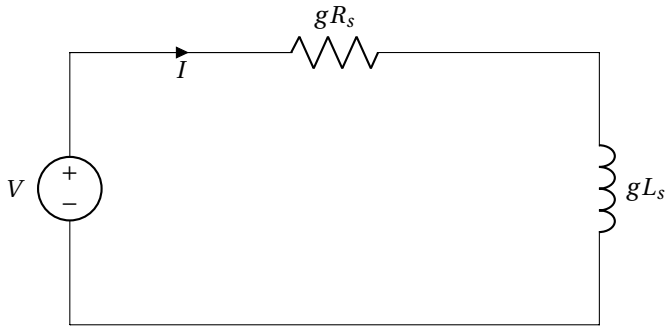

Figure 3.4: Superconducting model circuit under simulation

The surface impedance is converted to circuit parameter by a geometric factor 'g', which is dependent on the physical structure. In this section, a simple circuit is analyzed for stability. A resistance with resistance 'gR' connected in series with an inductor with inductance 'jgωL_s' is connected to a voltage source. It can be implied that the surface impedance of a superconductor, has a voltage component impressed upon it during the S parameter simulation. The equivalent circuitry is shown in 3.4. In order to understand further, the surface impedance for a wave propagating on a CPW line, can be rewritten as

$$Z_s = \frac{E_{tan}}{H_{tan}}$$

In figure 3.5, the tangential component of the field is marked as $E_{||}$. CPW lines are of

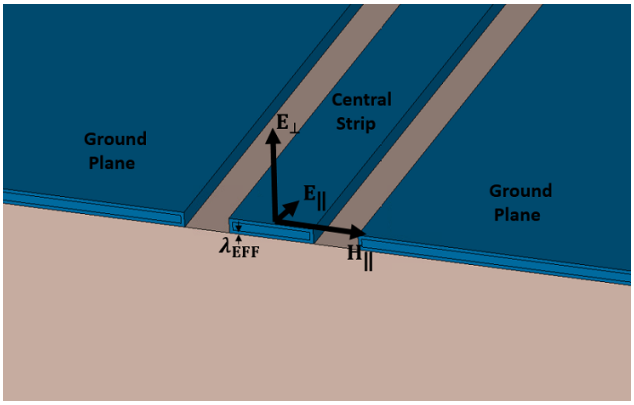

Figure 3.5: Field components in a superconducting CPW

interest in this work since the transmon qubit is built with CPW technology. In case of a PEC material, the $E_{tangetial}$ is zero and hence the surface impedance of a PEC can be considered as zero, i.e., there is no resistive nor inductive component. Since the tangential component is zero, there is no voltage that is impressed tangentially to create instability. In case of a superconducting CPW structures, the tangential component is not zero [16], which causes the surface impedance. It is used as the property for modelling the superconducting material in the FEM simulations. The tangential component is marked as $E_{\parallel}$ in figure 3.5, is due to the penetrating magnetic field on the surface of the superconductor. This tangential component of the field, can cause a voltage to be impressed on the surface impedance. With a very low resistive, but inductive surface impedance model, it can cause instability in simulations. To understand the stability, the model circuit shown in figure 3.4 is discussed below.

For the circuitry shown in 3.4, by using Kirchhoff's law, it can be shown the following differential equation holds.

$$L\frac{dI}{dt} + RI = 0$$

The inductance (gL_s) of the circuit is referred to as L and the resistance (gR) offered is referred to as R. By considering an initial condition of current equal to I_0, the circuit has a impulse response of

$$h(t) = I_0 e^{-\frac{R}{L}t} u(t)$$

For a bounded signal x(t) applied to a system, for stability to be ensured at its output, the convolution of the input and the impulse response of the system must be bounded. This can be represented as

$$|y(t)| = \int_{-\infty}^{\infty} |x(t-\tau)h(\tau)|d\tau$$

using triangle inequality,

$$|y(t)| \leq \int_{-\infty}^{\infty} |x(t-\tau)||h(\tau)|d\tau$$

if the input signal is bounded or has a norm of V_0, which is the case in the S parameter simulation, the above equation is given by

$$|y(t)| \leq V_0 \int_{-\infty}^{\infty} |h(\tau)|d\tau$$

This can be simplified as

$$|y(t)| \leq \frac{V_0 I_0 L}{R} \tag{3.1}$$

It can be understood from equation 3.1, the bounded output of the circuitry is directly proportional to the circuit inductance, initial voltage and current, is inversely proportional to the resistance of the circuitry. As $R \to 0$, the output of the circuit is not bounded, i.e., $y \to \infty$. This implies that the resistance has to be finite for the circuit to be stable, for a given inductance value. However, the superconductor model that is described by [14], shows that the resistance exhibited by superconductor is significantly less than the inductive component or tends to zero. However, this causes instability problems. This can be remedied by adding a larger component predicted by the Mattis Bardeen model, but the resistive component that is added is seen to that it does not cause significant attenuation or losses in the circuitry. This ensures stability in the computational results. However, its impact on circuitry needs to be analyzed. Also, from [15] it can be noted that, in order for the dielectric model of a superconductor to satisfy the Kramers–Kronig relationship, the superconducting model needs to be considered to be slightly lossy in limits. This is another perspective to be looked from.

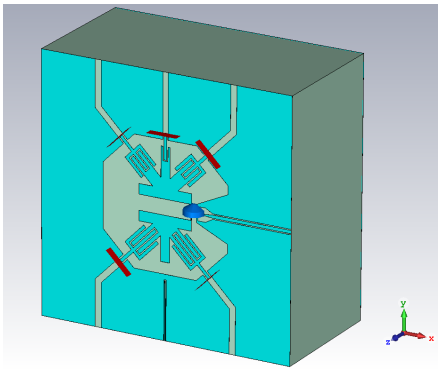

(a)

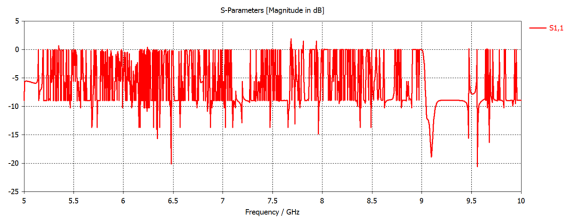

(b)

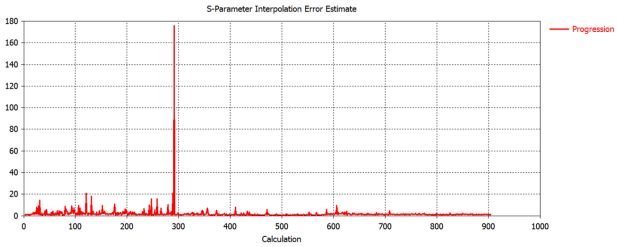

(c)

Figure 3.6: Instability analysis of S parameter simulations on a surface impedance superconducting qubit model. a. Qubit model [6] with several waveguide ports built with superconducting parts modelled with tabulated surface impedance model computed with [14] for NbTiN. The resistive component (in order 10^{-15} to 10^{-20}s) is much less than the inductive component. The surface inductance is taken as 2.5 pH/sq in this model. b. S_{11} parameter results from the model. The S parameter results from the simulation show abrupt fluctuations due to instability in the simulations caused by the model. c. Convergence based on S parameter interpolation error. There is a difficulty in obtaining the convergence and takes a large number of iterations. This can be inferred due to the instability caused by the surface impedance model.

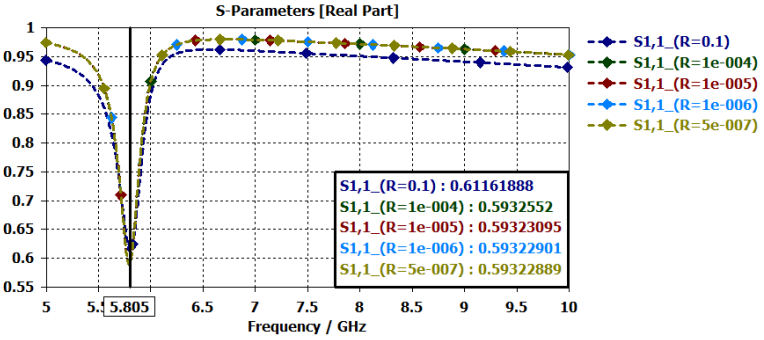

(a)

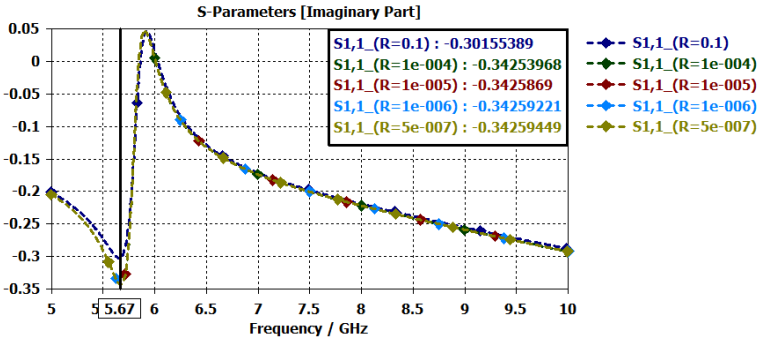

(b)

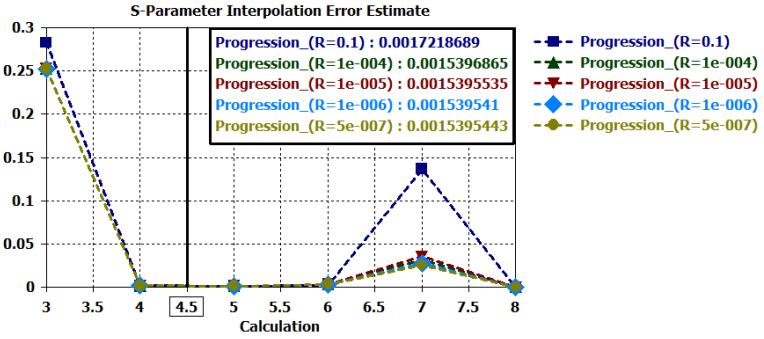

(c)

Figure 3.7: Stability analysis of S parameter simulations of a qubit model with a superconducting surface impedance. a. S_{11} parameter results from the qubit model simulation shown in figure 3.6a with adding resistance. It can be seen with respect to the previous figure 3.6a, the S parameters has a stable output. The output results does not deviate from a certain tolerance on going from a certain range of resistances of few order magnitude, i.e., for instance an increase in resistance of $1e^{-6}$ to $1e^{-5}$ has a change of $2e^{-6}$ in result magnitude for depth of resonance. However, the effect is severe, for the choice of resistance in the range of $1e^{-1}$ and above. This is primarily because of the attenuation constant, understood from the transmission line theory, becomes significant and plays a major role. The surface inductance is taken as 2.5 pH/sq. The model exhibits a stability on increasing the value of resistance to $5e^{-7}$ Ω /sq from 0. b. Convergence based on S parameter interpolation error with the added resistance. The convergence is stable compared to the previous model without added resistance.

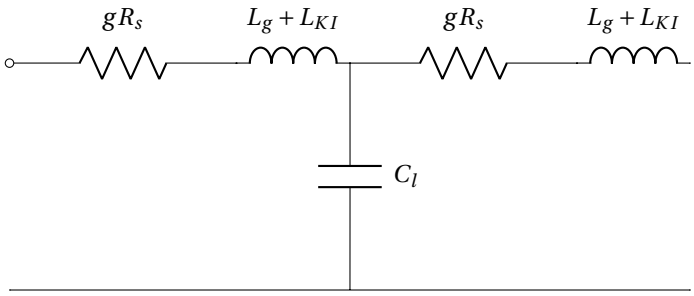

Figure 3.8: Superconducting Transmission Line

3.5. IMPACT OF RESISTIVE COMPONENT OF SURFACE IMPEDANCE

The interconnecting components between qubits such as bus resonators and the measurement circuitry are built using CPW lines. Superconducting CPW lines supports Quasi-TEM mode of propagation of electromagnetic waves in the region of qubit operation. To study the impact of an added resistance to the surface impedance model, an analysis of the transmission line circuitry with attenuation in focus, is done in this section. Also, in this work, the extraction parameters in the simulation primarily focuses on the resonators, its quality factors and the resonance frequency. Hence, limited considerations in circuit combinations are sufficient to understand the impact. Since the increased resistance is not part of an actual superconductor characteristics, care must be taken that the attenuation due to the added resistance does not change the circuit parameters.

3.5.1. CHARACTERISTIC LINE IMPEDANCE

A superconducting transmission line model is shown in figure 3.8. The inductive component seen by the wave is due to the CPW geometry and the kinetic inductance component due to the surface impedance of the superconductor. According to [16], the kinetic inductance is the surface impedance multiplied by a geometric factor gL_S. In addition to the inductive component, the impedance due to the resistive component adds up. If C_l is the capacitive component per unit length due to the CPW geometry and the dielectric on which the CPW is placed, L_g, L_K are the geometrical and kinetic inductance per unit length, the characteristic line impedance is given by

$$Z_0 = \sqrt{\frac{gR_s + j\omega(L_g + L_K)}{j\omega C_l}}$$

It can be seen if the resistive component added to the surface impedance to bring about stability in the simulation is small or $R_S << \omega(L_g + L_K)$, then the impact on the characteristic line impedance of the transmission line is minimal or negligible. This implies that the characteristic impedance of the transmission lines, such as a resonator will be unaffected in the case of a small attenuation.

3.5.2. PROPAGATION CONSTANT

The propagation constant of a superconducting transmission line is given by

$$\gamma = \alpha + j\beta$$

If the resistance and losses due to dielectric losses, radiation are minimal, then the propagation constant is given by

$$\gamma = j\beta \qquad\qquad \gamma = j\omega\sqrt{(L_g + L_{KI})C_l}$$

It can be inferred that if the gR_s is minimal, then the attenuation due to the added losses has minimal impact on the propagation constant.

3.5.3. IMPEDANCE OF A TRANSMISSION LINE RESONATOR

The input impedance of a transmission line resonator is given by

$$Z_{in} = Z_0 \frac{1 + j\alpha l \tan(\beta l)}{\alpha l + j\tan(\beta l)}$$

or

$$Z_{in} \approx Z_0 \frac{-j}{\tan(\beta l)}$$

The above equations convey that the line impedance of a transmission line does not change on adding an additional resistive component, if the attenuation caused by it is negligible or significantly less. It can also be shown that the attenuation of a CPW line on a dielectric substrate also depends on the radiation and dielectric losses in microwave frequencies. If the added resistance component exhibits attenuation much less than these components, then it does not make a difference in modifying the superconductor surface impedance model, from circuitry point of view on a resonator.

3.5.4. RESONANT FREQUENCY OF A TRANSMISSION LINE RESONATOR

The half wave resonators at the resonance can be approximated as parallel RLC circuitry at resonance. It can be found that the resonant frequency of the nth mode in the resonator is given by

$$\omega_n = \frac{1}{\sqrt{L_n C}}$$

where [13]

$$L_n = \frac{2L_l l}{n^2\pi^2}$$

$$C = \frac{C_l l}{2}$$

It can be inferred that the resistive component of the surface impedance does not play an influence at the resonant frequency of the resonant circuitry. L_l and C_l are the inductance and capacitance per unit length. The inductance per unit length consists of the geometrical inductance and the kinetic inductance, i.e., $L_l = L_g + L_k$. The geometrical inductance and the capacitance per unit length can be calculated analytically for a CPW line or computed using a FEM simulation. The analytical calculation is explained in the previous section 3.2.1. Using these parameters along with the unloaded resonance frequency of a resonator constructed with length l, one also can determine the kinetic inductance.

3.5.5. IMPACT ON QUALITY FACTOR OF A TRANSMISSION LINE RESONATOR

The internal quality factor of a transmission line resonator is influenced by the attenuation constant. According to [13], the internal quality factor is given by,

$$Q_i = \frac{n\pi}{2\alpha l}$$

If the attenuation caused by added resistance is minimal or is significantly less than the losses caused by the dielectric losses and radiation losses, then the Q_i is not significantly influenced. The effect of the internal quality factor is reflected on the S parameters by observing the depth of the resonant peaks. The bandwidth of the S parameters of a resonance is shown in figure 3.7. The width and depth of the resonance is unaffected when the tabulated surface resistance is changed from $1e^{-6}$ to $1e^{-5}$, an increase in resistance by a factor of 10. However, considerable change in the characteristics is observed when the tabulated surface resistance is set at $1e^{-1}$. The attenuation becomes considerable in the last case and the internal quality factor is affected, which is reflected in the depth of the resonance curve.

3.5.6. PHYSICAL IMPLICATION OF THE ADDED SURFACE RESISTANCE

The time varying magnetic field that penetrates the superconducting material causes an electric field, which causes the normal electrons to oscillate.

$$\nabla \times \vec{E} = \frac{d\vec{B}}{dt}$$

The added resistance could be considered in terms of an increased density of the normal electrons in the material that dissipates power or an added impurity, which loses more power and hence the increased resistance. This model can be seen only as an approximation to the real superconductor modelled in a FEM tool. Care needs to be taken such that the attenuation caused by the surface resistance needs to be small such that the circuit parameters remain unaffected.

4

Equivalent Circuit Model of a Qubit and Estimation of Parameters

The transmon qubit chip is built with a superconducting CPW, fabricated on a dielectric substrate and is housed in a metallic enclosure that is grounded. This physical construction of qubit system can be modelled as a 3D FEM structure and an electromagnetic simulation can be made to understand the circuit parameters. However, to understand or to design and predict the parameters, the equivalent circuit analysis is a very useful tool for characterization. The procedure to design the qubit system should be in such a way that the qubit design parameters are first described or requirements are laid out, then the physical geometry of the transmon qubit is changed or modified to implement the requirement. The circuit parameters can be extracted by DC or microwave FEM simulation and the effect of certain physical structure can be analyzed. On extracting the circuit parameters from a physical structure, one can construct lumped element models calculate analytically or numerically certain parameters such as charging energy, coupling factors, resonances of the equivalent physical system. The following sections describe procedures and methods to construct circuit models and extract circuit parameters such as phase velocity in resonators, estimate bus resonances and understand the impact of the interaction of the bus resonators with each other in a qubit system.

4.1. QUBIT UNIT CELL

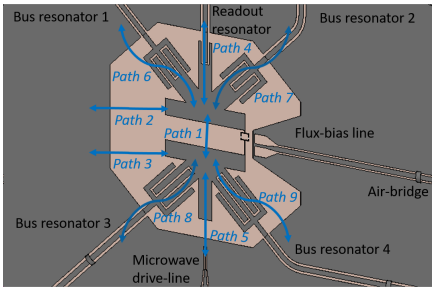

(a) Starmon transmon qubit.

Figure 4.1: Starmon II qubit structure [6]. The paths denote the charging and discharging paths of the capacitive components.

The first step to design a chip layout is to model the basic cell model of a qubit in a physical geometry. Using the basic model, layout or peripherals such as resonators, surrounding the transmon can be built with the required design parameters. All the theoretical capacitive parameters of a qubit unit cell design are converted to the physical implementation by constructing the appropriate geometry. These parameters can be implemented on a FEM 3D qubit model and from the implemented qubit geometry, the circuit parameters can be extracted by using a FEM simulation to verify and redesign. For example, during the design of a qubit unit cell, the capacitance used for coupling with the bus resonators needs to be characterized, which is necessary for designing the coupling strengths between two qubits. This is implemented in the physical geometry by changing the physical dimensions at the junction of the qubit and the bus resonator to arrive at the required theoretical capacitance. The physical geometry that is employed in the Starmon qubit is shown in figure 4.1. The charging islands across the Josephson's junction are marked across "Path 1". Path "2" and "3" denotes the charging and discharging of the capacitance between charging island 1, 2 and ground respectively. The Paths "4", "5" represent the capacitive paths between the charging islands and the readout resonator and microwave drive line. Paths "6", "7", "8" and "9" represent the capacitive paths between the charging islands and the bus resonators that is used primarily for inter qubit coupling.

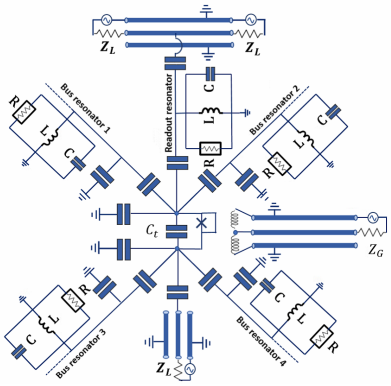

Figure 4.2: Starmon II transmon qubit equivalent lumped element circuit model [6].

The equivalent circuit model of figure 4.1 is shown in figure 4.2. This circuit model does not consider the inductance offered by the qubit unit cell structures but restricts only to the capacitive impedances.

4.2. ESTIMATION OF PARAMETERS

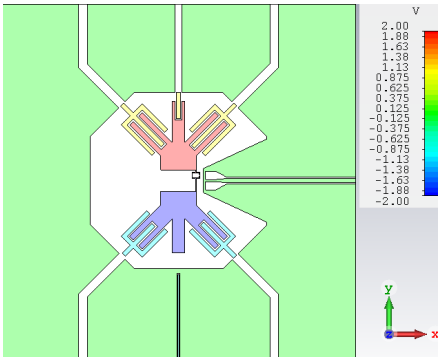

Figure 4.3: Starmon II qubit DC simulation model [6].

The components represented by "paths" in figure 4.1, has to be estimated from the physical structure. It is essential to extract the parameters from the physical geometry to understand the circuit parameter values that the physical structure can exhibit. The physical geometry can then be altered to exhibit the desired parameter value. In this work, 4 different qubit structures were analyzed and their parameters extracted. A method for circuit capacitance extraction is the FEM DC simulation. The electrostatic FEM solver is used to extract the capacitance matrix between the essential components, with each component excited with a different potential. A DC simulation setup is shown in figure 4.3. However, an analysis is also required to verify the results at GHz frequency range which is shown in appendix A. It can be found that the coupling capacitances from the

DC and microwave simulation are similar. However, in this work, the values for capacitances to model the lumped element circuit model were done with DC simulation results.

4.3. LUMPED ELEMENT CIRCUIT MODEL

The lumped element circuit model of a qubit system is constructed using the unit cell of a qubit shown in figure 4.2. The components such as resonators and the measurement circuitry is built around the qubit unit cell using the transmission line models. A physical S7 layout and its equivalent lumped element circuit model is shown in figure 4.4. Using the lumped element circuit layout, system parameters such as bus resonances, Q_c, can be analyzed through analytic methods or numerical analysis. In this section, the parameter extraction of the system loaded bus resonances using numerical methods is discussed. The procedure to extract the resonances of various components using a numerical method by circuit simulation is

a. Construct the layout according to the design

b. Generate the S parameters for the circuitry using the measurement circuitry i.e., by using ports on hanger 1 and 2.

c. Extract the resonances from S parameters from the ports across the hangers, for instance S_{13} or S_{14}.

The S parameters computed between hanger 1 and hanger 2, would show the resonances of various resonant circuits inside the chip. The resonant components that are found are the qubits, the readout resonators and the bus resonators, whose resonances are components of the Hamiltonian of the quantum system.

The inductance used in the scope of this work to model the Josephson's junction is 10 nH and the capacitive components used to model the qubit unit cell are extracted from the DC simulation. It is shown later in this chapter, that the results due to this model is inaccurate on comparing with the results on measuring a fabricated chip of the equivalent design. This error is due to neglecting the inductive components offered by the qubit unit cell elements. For instance, the green colored elements in figure 4.5 are part of the bus resonator. The change in dimension of the physical geometry of the resonator at the qubit-bus interaction joint will change the effective characteristic impedance of the resonator. This change is captured only by a capacitive term in the model and the inductive component is neglected. Such approximations would lead to inaccuracies in loaded bus resonance estimation.

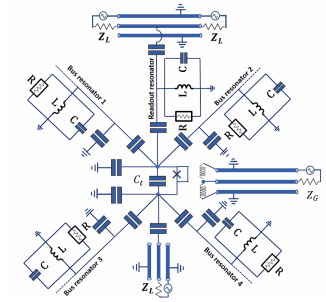

(a)

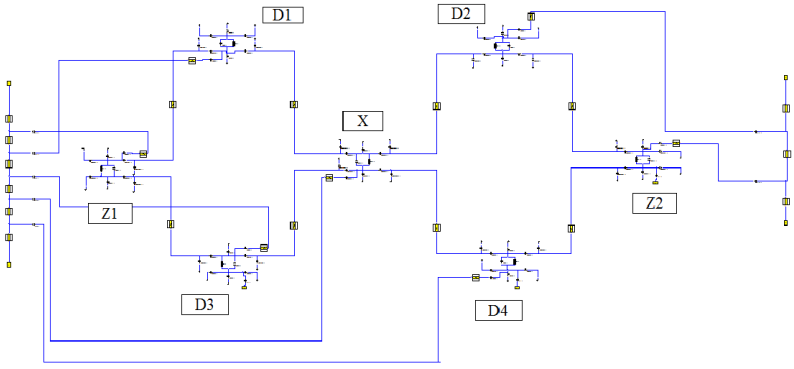

(b)

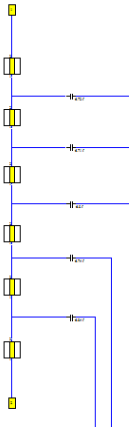

(c)

Figure 4.4: . a. Lumped element unit cell model. b. Equivalent S7 circuit built with lumped element model. c. Equivalent measurement circuitry (hanger 1) of the S7 chip.

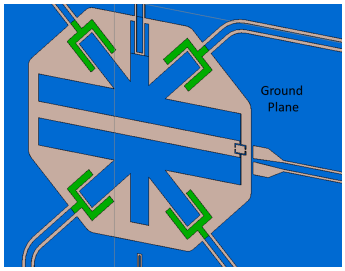

Figure 4.5: The structures marked with green are used to couple the charging islands to the bus resonators. Either they can be considered as part of the resonator or be approximated to be a capacitive structure with respect to the ground plane.

4.4. HYBRID FEM CIRCUIT MODEL

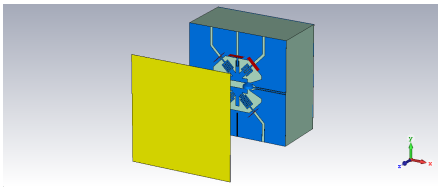

(a)

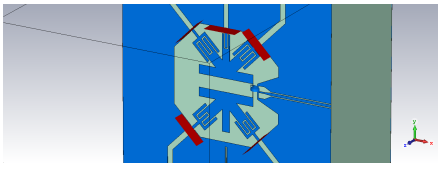

(b)

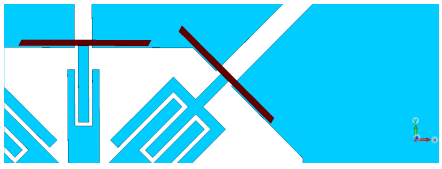

(c)

Figure 4.6: 3D FEM qubit model unit cell construction. 5 waveguide ports are placed at the interfaces to bus resonators and readout resonator. By performing FEM simulation, the characteristics of the unit cell can be obtained. This unit cell of a qubit can be used as a block, that can be used in circuit simulation. a. 3D model qubit unit cell with shin. b. 3D model qubit unit cell without shin. c. Waveguide ports placed in the 3D model qubit unit cell.

In order to improve the accuracy of the equivalent circuit model of a physical layout, a hybrid model of a circuit layout built with qubit FEM unit cells interconnected with standard circuit components is analyzed in this section. The measurement circuitry and the resonator components are modelled by circuit elements and numerical calculation by circuit simulation can be done on it. The FEM unit cell would be able to capture the inductive and capacitive effects of the unit cell physical structures at microwave frequencies. Using such a model, would be more accurate than the lumped element model and the computation is fast compared to a full chip FEM simulation. A typical FEM simulation of a full chip for a S7 chip can take a high amount of computational resources and time to complete. Whereas, the hybrid circuit simulation can take few seconds to minutes to compute the output based on the resolution of the frequency band.

The circuit block of a qubit unit cell can be extracted from 3D FEM model by using waveguide ports at the unit cell interfaces for connections to the peripherals such as resonator circuits. By design, the Starmon qubit has interfaces to connect to 4 bus resonators, a readout resonator and a microwave drive line. In this work, the microwave drive line port is neglected. Precautions must be taken to construct the size of the waveguide ports, which can have an influence on port impedance and the modes that will be propagated through the ports. The placement of ports on the qubit unit cell is shown in figure 4.6.

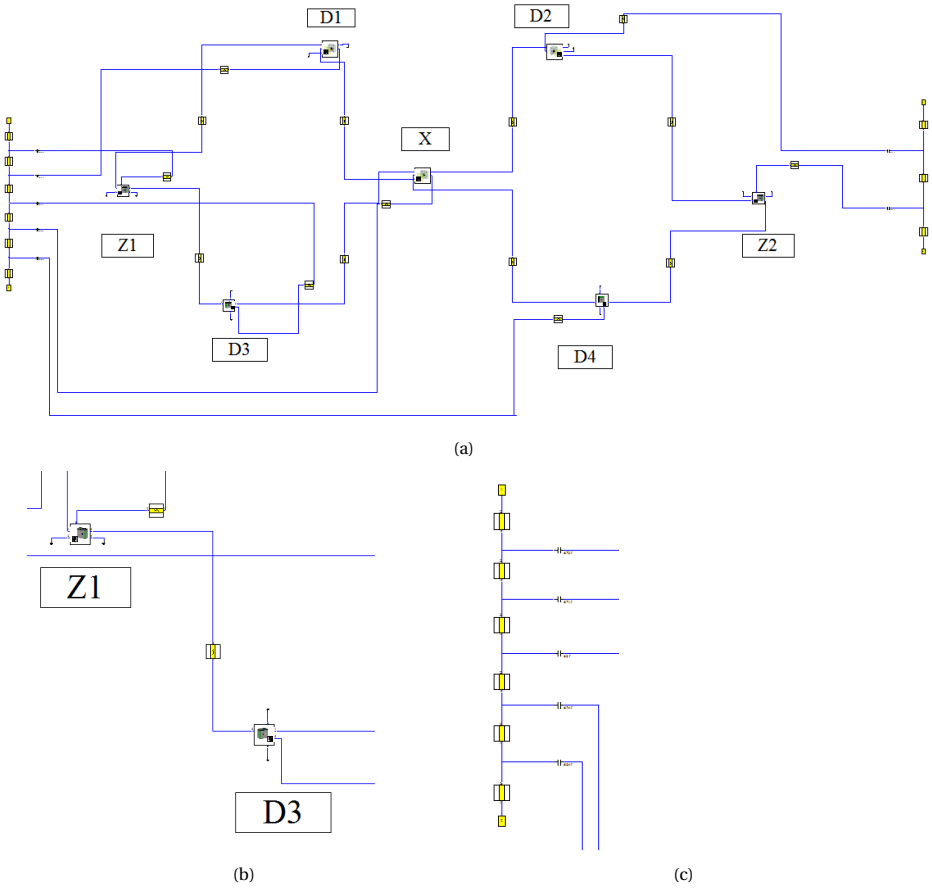

Figure 4.7: a. S7 layout constructed with a hybrid model. The measurement circuit that consists of transmission line for the feed line, readout resonators and bus resonators are constructed with standard circuit models. The qubit unit cells are provided as a circuit block, which is the output of unit cell FEM computation. b. Circuitry between two qubit unit cells. c. Measurement circuit that shows the feed line and the readout resonator capacitances.

4.5. PHASE VELOCITY ESTIMATION IN HANGER RESONATORS

An electromagnetic wave, propagating in the z direction can be represented as

$$\vec{x}(x,y,z) = \left(\vec{x_t}(x,y) + \vec{x_z}(x,y)\hat{z}\right) e^{-j\beta z}$$

where β is the propagation constant, $\vec{x_t}$ and $\vec{x_z}\hat{z}$ are the transverse and longitudinal components. If this is the case, then the analysis of a structure can be done using the transmission line theory. According to [16], the superconducting CPW lines, due to its structure and surface impedance does not support a pure TEM mode, but however to a Quasi-TEM mode, in which the modes that are not TEM are much smaller. Hence, in this analysis, transmission line theory is used, which is an approximation. The phase velocity is the rate at which a phase point in the wave changes in space with respect to time or is the velocity with which a phase point in a wave propagates. The phase velocity of a propagating wave in a transmission line is given by [23],

$$v_p = \frac{\omega}{\beta} \qquad\qquad \beta = \omega\sqrt{LC}$$

or it can also be written as

$$v_p = \frac{1}{\sqrt{LC}}$$

where L and C are the inductance and capacitance offered by the transmission line per unit length. In case of superconductors, the surface impedance contributes to the inductance, namely kinetic inductance. Hence, the inductance that is offered by the transmission line consists of $L = L_g + L_k$, L_g is the geometrical inductance of CPW line physical structure and L_k is the kinetic inductance due of the superconducting material.

$$v_p = \frac{1}{\sqrt{(L_m + L_k)C}}$$

For a half wave resonator, the phase velocity is given by [13]

$$v_p = f_0 2l$$

where $2l$ equal to the λ_0 is the resonant mode wavelength of the half wave resonator and f_0 is the unloaded frequency. The phase velocity can be considered as a quantity that is a takes into account the physical construction of the CPW and the superconducting material property. It can be used to determine the CPW line length of a resonator corresponding to the required unloaded resonance frequency. It is of interest to determine the phase velocity in a resonator on a fabricated chip. Methods to determine the phase velocity by estimating the unloaded resonances of readout resonators from measurements is discussed in the following section. The phase velocity determined from the readout resonators in a qubit system can be used to determine the unloaded resonances of the bus resonators constructed with a length l. This step is useful for building circuit models.

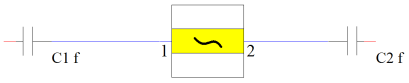

Figure 4.8: Half wavelength resonator with coupling capacitances

4.5.1. UNLOADED RESONANT FREQUENCY ESTIMATION FOR HALF WAVELENGTH RESONATOR WITH CAPACITANCE COUPLING

In order to estimate the unloaded resonant frequency from the measured or loaded resonant frequency of a resonator, first an analysis is done for a simple capacitively coupled, open circuited half wavelength transmission line resonator. The resonator circuit is shown in figure 4.8. The method to solve this problem can be found in [20]. During measurements of a circuit with half wavelength resonator with impedance loading on both ends using the S parameter, the resonance that is observed is the loaded resonance. This resonance of the half wavelength resonator is different than the resonance that is observed without any impedance loading. The impedance seen across both edges of a half wavelength resonator play a role in the loaded resonance. This implies that for deriving the loaded resonant frequency of a capacitively coupled half wavelength resonator shown in figure 4.8, the capacitive impedance of the circuit seen across the edges needs to be taken into account. At resonance, the imaginary component of the equivalent impedance of the circuit is zero. This can be written as

$$Z = -\frac{Z_0}{tan(\beta l)} - \frac{1}{\omega C_1} - \frac{1}{\omega C_2} = 0$$

Near the resonance frequency, $\beta l = \pi + \frac{\Delta\omega}{\omega}$. Also, since $\frac{\Delta\omega}{\omega}$ is very small, $\tan(\frac{\Delta\omega}{\omega}) = \frac{\Delta\omega}{\omega}$. $\Delta\omega$ accounts for the shift in the resonance frequency from the unloaded resonance. This leads to the equation being simplified as

$$\frac{-Z_0}{\frac{\Delta\omega}{\omega_{1/2}}} = \frac{1}{w_0 C_{eq}}$$

or

$$-Z_0 w_0 C_{eq} \omega_{1/2} = \Delta\omega$$

where $C_{eq} = \frac{C_1 C_2}{C_1 + C_2}$ and w_0 is the loaded frequency. Using the above expression, one can relate the loaded and unloaded resonant frequencies. $\Delta\omega$ has two possible solutions, $\omega_0 + \omega_{1/2}$ or $\omega_0 - \omega_{1/2}$. For capacitive loaded circuitry, the $\Delta\omega = \omega_0 - \omega_{1/2}$ needs to be considered. The inductive component offered by the half wavelength resonator churns out the capacitive components on loading, requiring the negative shift. The loaded resonance frequency is given by,

$$w_0 = \frac{w_{1/2}}{1 + Z_0 w_{1/2} C_{eq}}$$

and the unloaded resonant frequency is given by

$$w_{1/2} = \frac{w_0}{1 - Z_0 w_0 C_{eq}} \tag{4.1}$$

A capacitively coupled half wavelength readout resonator can be used for measuring the state of the qubit. The capacitance C_1 can be considered as the capacitance that is connected with the hanger or the feedline to the resonator and the capacitance C_2 arises due to the equivalent capacitive impedance seen from the edge of the resonator towards qubit. The configuration shown in figure 4.8 can be considered as the approximate model of the qubit measurement resonator circuitry for calculating the unloaded resonance.

4.5.2. ESTIMATION OF QUBIT READOUT RESONATOR RESONANT FREQUENCY

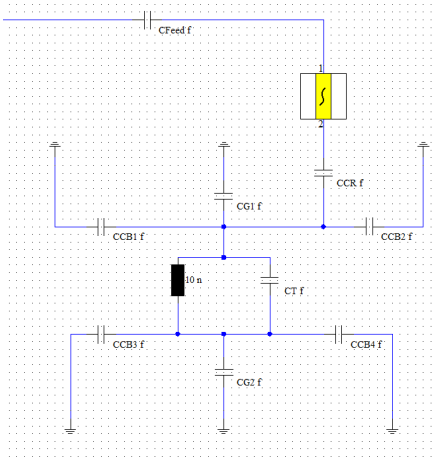

Figure 4.9: Readout Resonator Coupling

The readout resonator circuitry for a qubit is shown in figure 4.9. It consists of the readout resonator coupled with a capacitor C_{Feed} to the hanger and a capacitor C_{CR} to the qubit. This circuit is an approximation that restricts the circuit to the unit cell of the qubit. On solving the impedances towards the qubit end of the resonator, the impedances can be written as

$$Z_1 = \frac{j w_0 L_T}{1 - w_0^2 L_T C_T}$$

$$Z_2 = \frac{-j}{w_0 C_1}$$

where C_1 is the equivalent capacitance seen at the lower branch from the qubit junction, provided by the capacitances to the bus resonator interconnects. In figure 4.9, the

capacitance C_1 can be written as $C_1 = CCB3 + CCB4 + CG2$. C_T and L_T are the qubit junction capacitance and inductance respectively.

$$Z_3 = \frac{-j}{w_0 C_2}$$

where C_2 is the equivalent capacitance seen at the upper branch from the qubit junction, provided by the capacitances to the bus resonator interconnects. In figure 4.9, the capacitance C_2 can be written as $C_2 = CCB1 + CCB2 + CG1$. If Z_1, Z_2 and Z_3 are known, then the equivalent impedance Z_4 can be written as

$$Z_4 = \frac{(Z_1 + Z_2)Z_3}{Z_1 + Z_2 + Z_3}$$

At resonance, the imaginary component of the total circuit impedance is 0. This can be written as

$$Z = -\frac{Z_0}{tan(\beta l)} - \frac{1}{\omega C_{Feed}} - \frac{1}{\omega C_{CR}} + imag(Z_4) = 0$$

Let

$$A = \frac{1}{\omega C_{Feed}} + \frac{1}{\omega C_{CR}} - imag(Z_4)$$

At resonance, $\beta l = \pi + \frac{\Delta\omega}{\omega}$. $\frac{\Delta\omega}{\omega}$ is very small leads to $\tan(\frac{\Delta\omega}{\omega}) = \frac{\Delta\omega}{\omega}$. On similar arguments to the previous section regarding the shift in loaded resonance from unloaded, the resonant frequency can be written as

$$w_{1/2} = \frac{A\, w_0}{A - Z_0} \tag{4.2}$$

4.5.3. S7 CHIP PHASE VELOCITY ESTIMATION USING NUMERICAL METHOD

In order to obtain the phase velocity, the unloaded frequency needs to be determined. This can be achieved by first making an equivalent layout using the circuit model. The unloaded resonant frequency is tuned in the circuit model such that in the circuit simulation, the loaded resonant frequency is the same as the frequency measured in the fabricated S7 chip. Using such a technique, the phase velocity can be determined, since the length of the resonator line is known. This method does not restrict to an approximation of a qubit unit cell as described in the previous section. As the qubit system scales to a larger circuit, it is easier to resorting to the numerical method. The table 4.1, shows the length of the resonator, the measured readout resonant frequency and the equivalent unloaded resonant frequency extracted using this numerical method.

The unloaded resonant frequencies for readout resonators computed from the model expressed in equation 4.1 using the capacitance that is connected to the resonator and feedline as C_1 and the capacitance from resonator to qubit as C_2 is termed as method 1, method 2 computed from equation 4.2, and from the hybrid simulation (numerical method) are tabulated in table 4.1. It can be observed that both the approximate analytical methods 1,2 show a difference with respect to the numerical method, with method

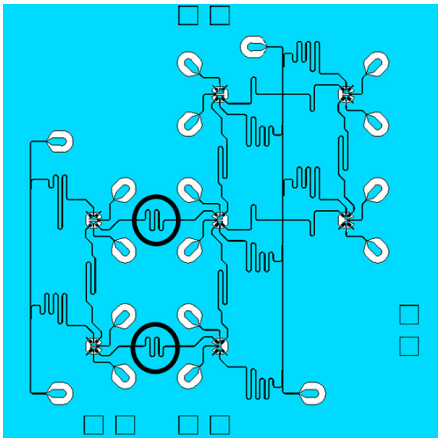

Figure 4.10: Curved structures on S7 readout resonator. This chip is designed, fabricated and measured by Intel and QuTech (DiCarlo Lab).

2 performing better than method 1. This stems from the approximation that is used. In method 1, only the nearest capacitance to the resonator is taken into account, whereas in method 2 the approximation is restricted to the qubit unit cell. It can be observed from the table 4.1 that the phase velocity in the resonators of equal length are not the same, i,e., the unloaded resonant frequencies vary in order of MHz, i.e. 9.2 MHz (D1, D2) and 4.1 MHz (Z1, Z2) for two cases. This could be due to the curved structure of the readout resonator design and uneven height of the film. This is illustrated in figure 4.10. The average phase velocity of the physical S7 chip that is taken as a reference is found to be 9.03599e7 m/s. There could be an error in this numerical method, if the capacitance from the resonator to the feed line is not accurately determined. Inaccuracies in the capacitance estimation will determine the accuracy of phase velocity determination. Phase velocity can be extracted more be reliably when a quarter wavelength test resonator is used on the chip, which is very weakly coupled to the feed line. The measured resonance for such a resonator can be considered as the unloaded resonance, which can be used to calculate the phase velocity.

Phase Velocity determination from Measurements using Equivalent Simulation Model						
Qubit readout resonator	Measured readout resonator frequency (GHz)	Unloaded readout resonator frequency using numerical method from section 4.5.3 (GHz)	Unloaded readout resonator frequency using method 1 from section 4.5.1 (GHz)	Unloaded readout resonator frequency using method 2 from section 4.5.2 (GHz)	Length of readout resonator (um)	Phase velocity 10^7(m/s)
Z2	7.464	7.5795	7.5203	7.5358	5962.26	9.0382
D2	7.5	7.6288	7.5568	7.5753	5924.24	9.039
D1	7.494	7.6251	7.5477	7.5661	5924.24	9.0346
Z1	7.46	7.5712	7.5162	7.5317	5962.26	9.0283
X	7.407	7.5318	7.4784	7.4799	6000.76	9.0393
D3	7.363	7.4793	7.4177	7.4331	6039.76	9.0346
D4	7.321	7.4334	7.3757	7.3757	6079.28	9.0379

Table 4.1: Qubit phase velocity determination

4.6. ANALYSIS OF BUS RESONANCES

As demonstrated in the phase velocity estimation problem in the section 4.5.3, the loaded resonance of a capacitively coupled open circuited transmission line depends on the equivalent impedance seen across the edges. For a bus resonator, the circuitry seen at both edges are qubits, which are coupled to other resonant circuits. A set of unloaded resonances used in a surface code 7 chip is shown in figure 4.11. The typical design is that the frequency regime of qubit resonances is between 4.9 GHz to 6.7 GHz, the readout resonances is between 7 GHz to 8 GHz and the bus resonances is higher than both the other circuitry, 8 GHz to 9 GHz.

To target various qubit operations, such as two-qubit gate time, it is important to target the coupling strengths between the qubits. This coupling strength depends on the loaded resonance frequency of the buses. However, it becomes a challenge to accurately predict the bus resonance frequency of individual bus resonators when the circuit has many buses closely spaced in the frequency spectrum. This is due to inter dependence of the resonant frequencies of each resonator on another.

For a chip implementing a surface code, each bus resonator has a maximum immediate 6 bus resonator neighbors. The resonators are designed to have a frequency spacing of 50 MHz. Each resonator has four impedance regimes, shown in figure 4.11, namely,

a. a low inductive impedance regime.

b. a highly inductive impedance regime.

c. a low capacitive impedance regime.

d. a high capacitive impedance regime.

Near the resonances, there could be a either a large impedance due to a large induc-

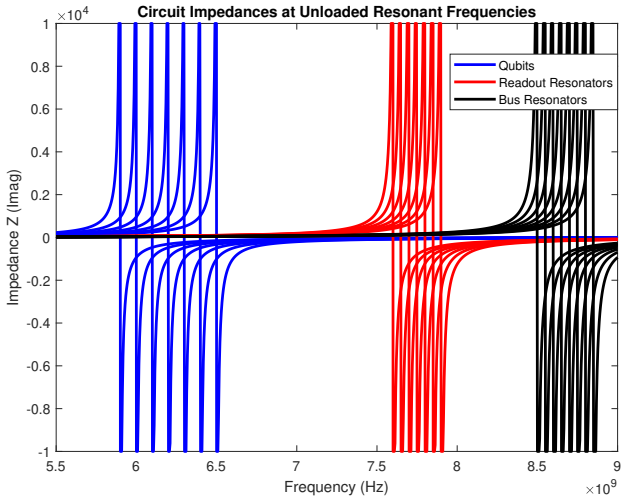

Figure 4.11: Resonances in a S7 Chip

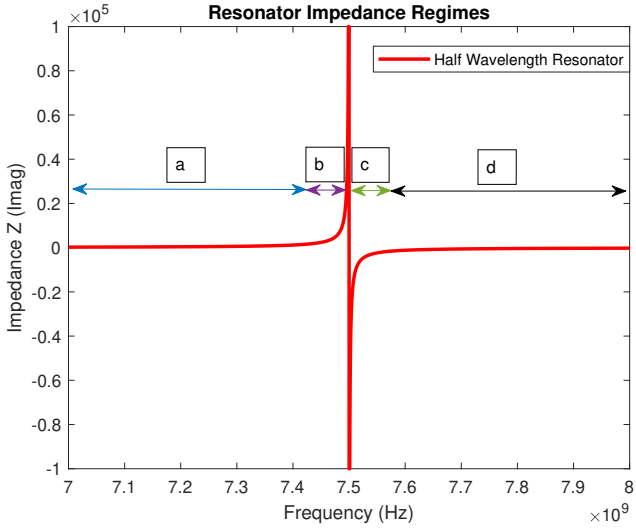

Figure 4.12: Resonance regimes of a half wavelength resonator. a. Low inductive regime - low impedance. b. High inductive regime - high impedance. c. Low capacitance regime - high impedance. d. High capacitance regime - low impedance.

tive impedance or a large capacitive load due to a very small equivalent capacitance.

In a surface code qubit circuitry, each bus resonator would have either one of the following combination of neighbors.

a. All bus resonator neighbors exhibit inductive regime impedance, i.e, bus resonator

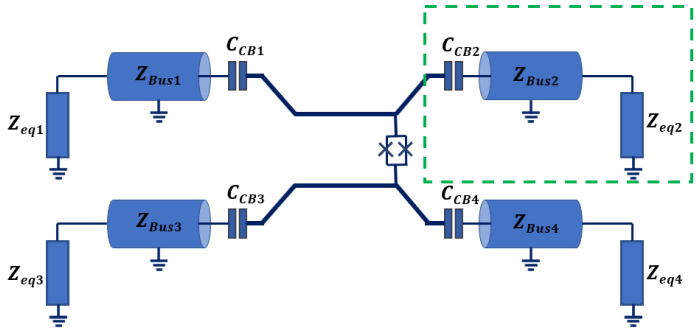

(a)

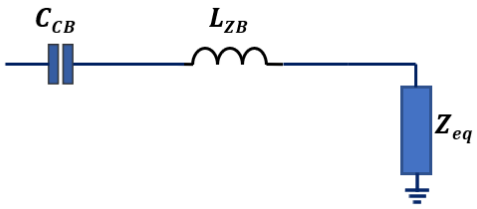

(b)

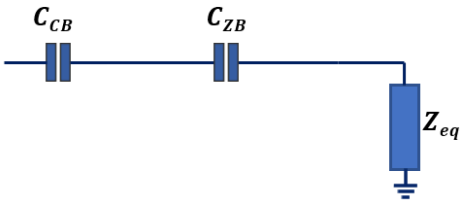

(c)

Figure 4.13: a. Impedance diagram seen from a qubit junction. The impedance across the edge of each resonator depends on the impedance offered by the neighboring resonators and its neigboring circuit. b. Equivalent inductive impedance offered by the resonator marked in figure 4.13a in the inductive regime. The resonance impedance regimes are described in figure 4.12. This inductive component can change the effective impedance seen at the edge of the resonator. c. Equivalent capacitive impedance offered by the resonator marked in figure 4.13a in the capacitive impedance regime.

neighbors operate at higher frequency

b. Few bus resonator neighbors exhibit inductive regime impedance and few resonator neighbor exhibit a high capacitive impedance

c. All bus resonator neighbors exhibit capacitive regime impedance, i.e, bus resonator neighbors operate at lower frequency

In figure 4.13, the impedances seen by a qubit junction is shown. Based on the reso-

nance frequency of the neighboring resonator, each resonator faces either a capacitive or inductive impedance at its edges. The impedance loading at the edges of each resonator, determines the loaded resonance frequency of each resonator. Since each bus resonator is placed at resonances that are close by in frequency to neighboring resonators in a surface code qubit, each resonator is predominantly affected by neighboring bus resonators. It is possible to analytically estimate easily when the impedance exhibited by the neighboring resonator is capacitive. However, it becomes more difficult to estimate the resonance with a neighbor bus resonator exhibiting high inductive impedance. This is because the effective impedance, including the impedance of the neighboring circuitry, is difficult to be computed if the exact bus inductive impedance is not known. In case of capacitive regimes, an upper bound approximation can be made. Furthermore, since each circuit is dependent on each other for the loaded resonances, it becomes a necessity to build an accurate circuit model. For frequencies, at much greater or lesser than the resonance frequency, marked by regimes "a" and "d" in figure 4.12, the impedance offered by the resonator is minimal. In these regimes, the impedance of the surface code qubit circuitry is almost not influenced by the adjacent resonators impedances.

To demonstrate the impedance regimes, a hybrid simulation for few different conditions is shown in the following section. The simulation conditions that are considered are

A. Resonance estimation with standalone half wavelength test resonator

B. Resonance estimation with capacitive loads at edges of the test resonator.

C. Resonance estimation with qubit circuitry at edges (capacitive loading) of the test resonator.

D. Resonance estimation of a test resonator connected with qubits at its edges. The qubit circuitry is connected with 6 other neighboring bus resonances at inductive regime (operating at higher resonances).

E. Same setup as case D, but with the qubit circuitry connected with 6 other neighboring bus resonances at capacitive regime (operating at lower resonances).

F. Resonance estimation of a test resonator with an interconnected qubit circuitry layout.

The test resonator described is a half wavelength resonator with a unloaded resonance of 8.5 GHz in the simulation cases. In case A, there is no loading effect which can be seen from figure 4.14a. On adding a coupling capacitance of 20 fF at the edges of the resonator in case B, the Z parameters show that the resonance has moved down to a range of 8.2 GHz to 8.3 GHz from 8.5 GHz.

In case C, the test resonator is loaded with qubits on either ends. The impedance offered by a standalone qubit with resonance at around 5 GHz to 6 GHz, at 8 GHz and above, is highly capacitive in nature. This can be inferred from the resonance regimes of a parallel LC oscillator circuitry. On connecting the resonator with a setup shown in figure 4.16a, i.e., edges connected with qubits, the loaded resonance is shifted further down, to a range of 7.95 GHz to 8 GHz. The next case D, E is constructed with the qubits connected to half wavelength resonators at its interface edges, with the test resonator between two qubits. This setup is shown in figure 4.17a. The resonators that is connected at the edges of the resonators are simulated with all of them operating at slightly higher resonant frequency than the test resonator, i,e, 8.6 GHz for case D, and then simulated

at lower resonant frequency at 7.9 GHz for case E. At slightly higher frequency, the resonators exhibit highly inductive impedance with respect to the test resonator resonance, and at lower frequency, the resonators exhibit capacitive impedance with respect to the test resonator. It can be seen that the impact is that the resonance of the test resonator is shifted to a range of 7.9 GHz to 7.95 GHz in case E, i.e., for the inductive regime case. The resonance of the test resonator is observed to be at a lower frequency, than the previous case of only having to connect with the qubit. The inductive component is seen to decrease the impedance (higher effective capacitance) offered by the capacitive qubit unit cell, which has caused the larger shift. However, in the capacitive regime case E, the simulation results show that the resonance of the test resonator is between 8 GHz to 8.1 GHz. This is because the net capacitive loading seen across the edges is lower than the previous case. The last case that is analyzed in this section is for a typical qubit circuitry shown in 4.18a. The unloaded resonances of each of the resonators were at 8.5 GHz. The loaded resonance is spread between 7.8 GHz to 8.1 GHz. It can be inferred that each of the bus resonators have an interaction with each other. In this case, all the resonators have moved down in frequency of its loaded resonances significantly from its unloaded resonances. The resonator that sees the inductive impedance of all its neighbors would be the one that is shifted the most, whereas the resonator that sees capacitive loading by its neighboring resonators would have shifted the minimal. The results of all the simulation cases collectively is shown in figure 4.19.

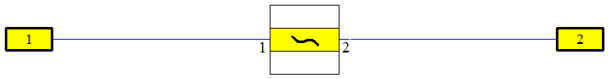

(a)

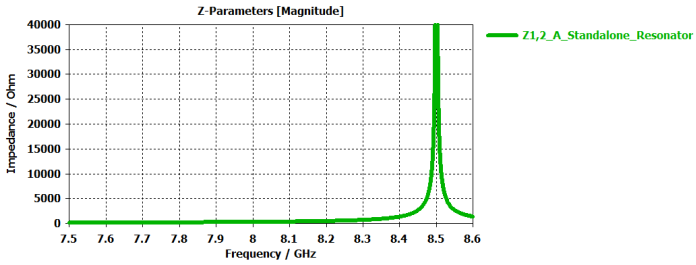

(b)

Figure 4.14: a. Simulation setup for case with half wavelength resonator (case A). b. Z_{12} of the simulation.

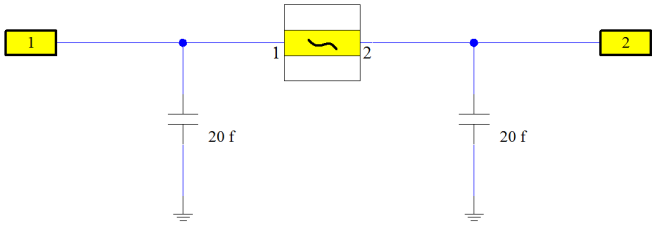

(a)

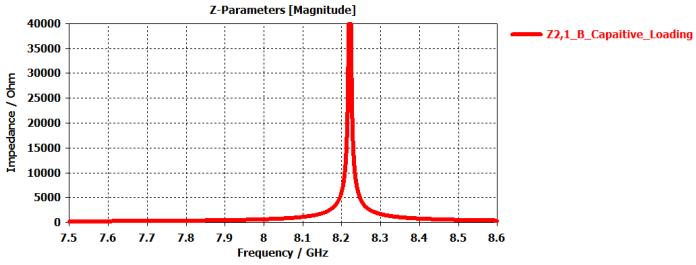

(b)

Figure 4.15: a. Simulation setup for case with half wavelength resonator connected with capacitive loading at its edges (case B). b. Z_{12} of the simulation.

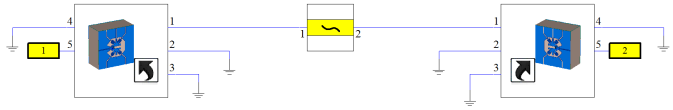

(a)

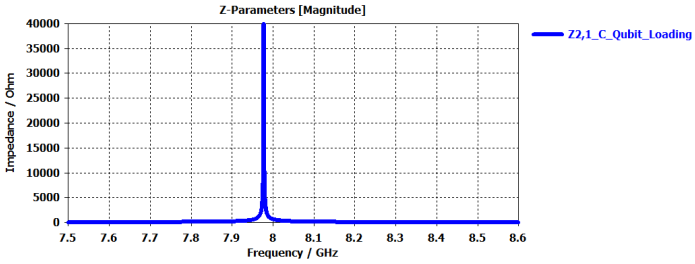

(b)

Figure 4.16: a. Simulation setup for case with half wavelength resonator connected with qubit unit cell loading at its edges (case C). b. Z_{12} of the simulation.

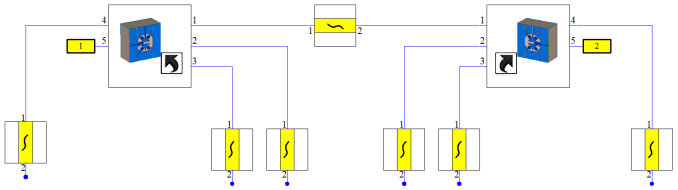

(a)

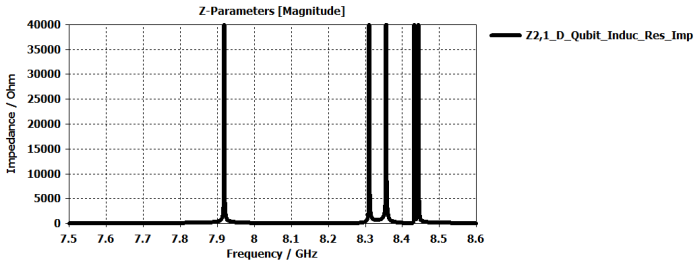

(b)

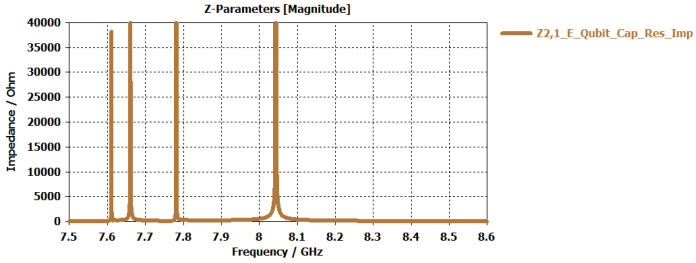

(c)

Figure 4.17: a. Simulation setup for case with half wavelength resonator connected with qubit unit cell loading at its edges with other resonators providing a inductive loading (8.6 GHz resonances) and then a capacitive loading (7.9 GHz resonances) (case D and E) respectively. b. Z_{12} of the simulation for case D. c. Z_{12} of the simulation for case E.

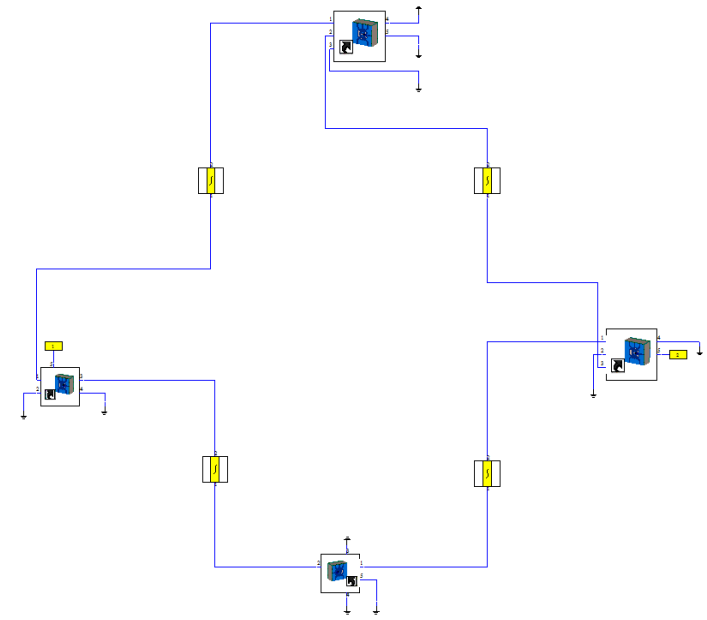

(a)

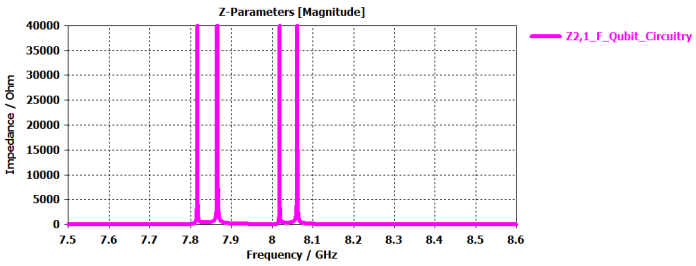

(b)

Figure 4.18: a. Simulation setup with circuitry constructed with multiple qubits. All the half wavelength resonators operate at 8.5 GHz (case F). b. Z_{12} of the simulation.

4.6.1. ESTIMATION OF BUS RESONANCES OF A S7 CHIP

In this section, a comparison between the proposed models and a physically implemented chip is verified. The first step is to determine the phase velocity of the readout resonators, which is explained in the previous section 4.5.3. Since, the physical dimension of the CPW structure in 2D plane (transverse plane of propagation) of the readout resonators and the bus resonators are the same, results in same inductance and capacitance per unit length of these resonators. This implies that the same phase velocity can be used to determine the unloaded frequency of the bus resonators by using the follow-

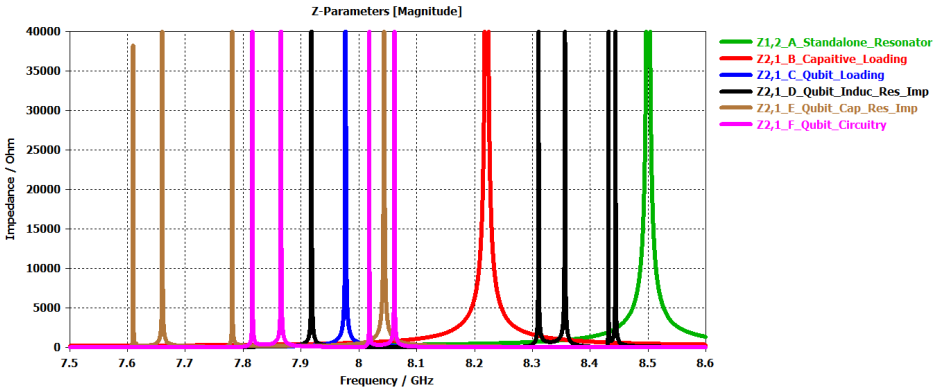

Figure 4.19: Resonator resonances for simulation setups shown in figure 4.18. In each of the case, the unloaded frequency of the resonator under test is at 8.5 GHz. It can be seen that there is no shift for case A. On adding a capacitive load in case B, there is a shift in the loaded resonant frequency. In case C, the loaded resonance is further shifted down, because the qubit loading is more capacitive. For Case D and E, the shift down due to the inductive loading is more than the capacitive loading. There are multiple resonances for case D and E, the loaded resonance corresponding to the resonator under analysis is between 7.9 GHz to 8 GHz for the inductive loading analysis and between 8 to 8.1 GHz for the capacitive loading analysis. In case F, all the resonators appear to have shifted down from an unloaded resonance of 8.5 GHz.

ing relationship

$$f_0 = \frac{v_p}{2l}$$

where f_0, v_p, l are the unloaded resonant frequency, phase velocity and length of the conductor respectively. The phase velocity is estimated to be 9.0315e7 m/s. The corresponding unloaded resonant frequencies computed from the phase velocity are tabulated in table 4.2. These unloaded resonant frequencies are used in the S7 chip layout constructed with lumped element circuit model and hybrid circuit model using which numerical computations are made.

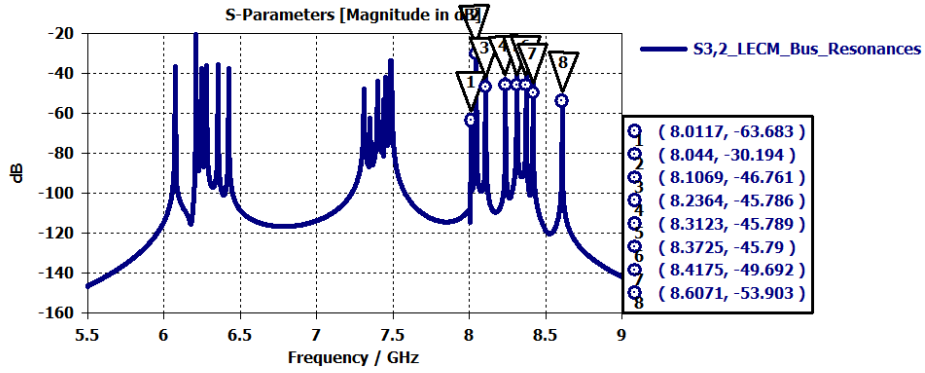

Figure 4.20: Resonances computed by numerical computation using lumped element circuit model

Targetted Unloaded Bus Resonances		
Qubit bus resonator	Length of bus resonator (um)	Unloaded bus resonator frequency (GHz)
D1_X	5150.41	8.76778
D1_Z1	5169.39	8.73559
D2_X	5251.26	8.5994
D2_Z2	5141.83	8.78242
D3_X	5003.76	9.0248
D3_Z1	5096.65	8.8603
D4_X	5110.56	8.8362
D4_Z2	5070.42	8.9061

Table 4.2: Targetted unloaded bus resonances for the corresponding length of the resonator used in the reference S7 circuit layout model. The phase velocity calculated from section 4.5.3 is used to calculate the unloaded resonance frequency.

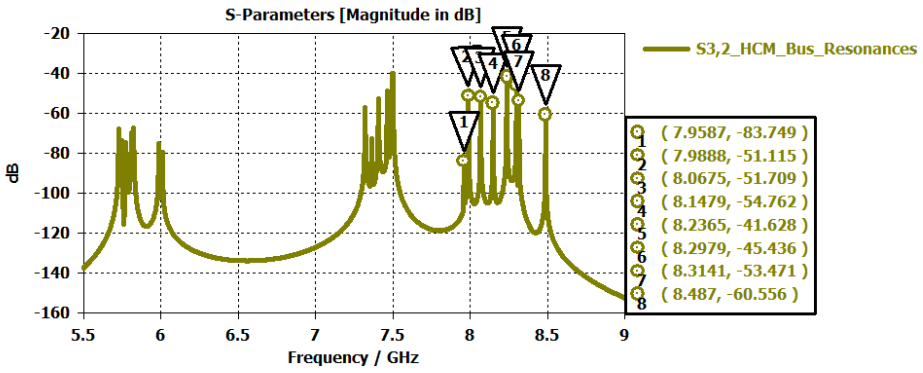

Figure 4.21: Resonances computed by numerical computation using hybrid circuit model

Comparison of Bus Resonances predicted by models with measured results			
Qubit to qubit bus	Numerical computation of bus resonances using lumped element circuit model (GHz)	Numerical computation of bus resonances using hybrid circuit model (GHz)	Measured bus resonances from fabricated chip (GHz)
D4_X	8.0117	7.9587	7.843
D2_X	8.044	7.9888	7.941
D1_Z1	8.1069	8.0675	7.986
D3_Z1	8.2364	8.1479	8.031
D4_Z2	8.3123	8.2365	8.14
D2_Z2	8.3725	8.2979	8.19
D1_X	8.4172	8.3141	8.234
D3_X	8.6071	8.487	8.32

Table 4.3: Comparison of resonances computed numerical methods using the two models with measured results.

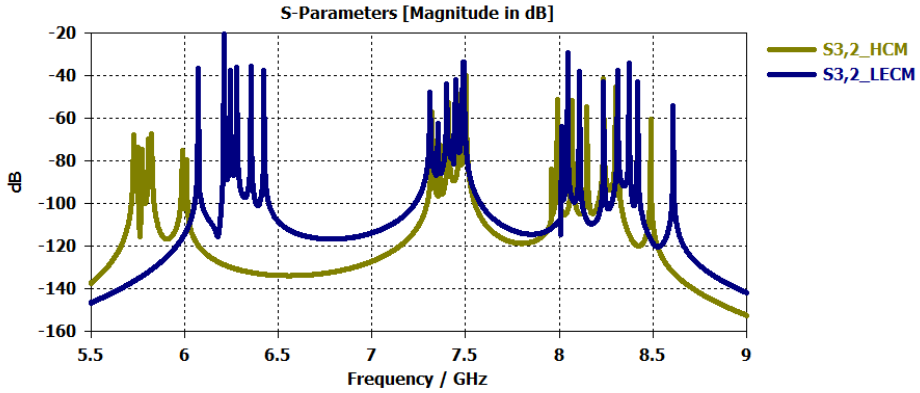

Figure 4.22: Comparison of resonances computed numerically by the two models. For the same Josephson's junction inductance used in the two models, the qubit resonances are found in a different frequency range. This difference can be attributed to the geometrical and kinetic inductive components being considered in the hybrid circuit model.

The plots of the S parameters between hanger 1 and 2, numerically computed using the lumped element and hybrid circuit model is shown in figure 4.22. It can be observed that the range of resonances of the qubits differ on choosing the same Josephson's junction inductance. This difference is due to the inclusion of the inductive components in the hybrid circuit model. It can be observed that the spread of the bus resonances computed by hybrid model is closer to the measured results than the other model. The errors in detecting the minimum difference in the first bus resonance peak from measurement and computed results are 168.7 MHz and 115.7 MHz using lumped element and hybrid

circuit models respectively. This can be inferred in table 4.3.

The spread of the bus resonances computed with the lumped element and hybrid circuit models are 595.4 MHz and 528.3 MHz. This compares with the spread in the measured resonances in the equivalent fabricated chip of having 477 MHz in spread. Out of both the models constructed, the hybrid circuit model numerical calculation provides the best results.

The readout resonances predicted by both the models, tend to lie in similar range of resonances. Hence, for readout resonance prediction, the lumped element circuit model, which uses approximate model of the qubit unit cell is sufficient. Whereas, for the bus resonance prediction, one needs to use a sophisticated hybrid circuit model for accurate prediction or a 3D full chip FEM simulation. Although, it should be noted that the lumped element circuit model provides an approximate solution for bus resonance prediction. It can be concluded that hybrid circuit model provided the most accurate model. The errors resulting from the lumped element circuit model is that the approximation of the qubit unit cell does not consider the circuit inductive components offered by the charging islands and neighboring CPW structures. The geometrical, kinetic inductive components along with the capacitive components are considered in the hybrid circuit model, which makes the difference.

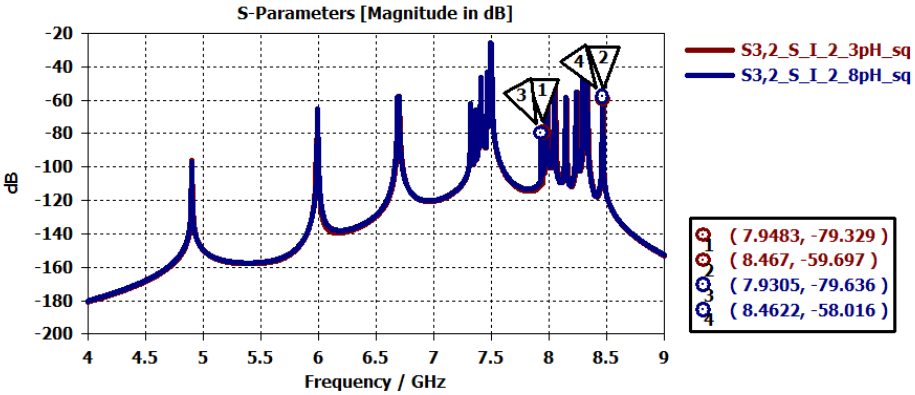

Figure 4.23: Bus resonances computed numerically by using hybrid circuit model for different film property

The qubits in the surface code are not operated at same frequencies. The qubits D1, D2 are targeted at 6.7 GHz, D3, D4 are targeted at 4.9 GHz, Z1, Z2 and X are targeted at 6 GHz. From previous section, the hybrid circuit model was considered to be the best model. Hence, in this section an analysis is done by operating the qubits at the mentioned frequencies, varying the film property and comparing with measurements. The inductive part of surface impedance or L_s in this case, of the measured S7 chip is estimated to be between 2.3 pH/sq to 2.8 pH/sq from measurements. The numerical results of the hybrid model computed with L_s of 2.3 pH/sq, 2.8 pH/sq are shown in figure 4.23 and tabulated in table 4.4.

The average difference between the bus resonances that is measured and the hybrid circuit model predicted resonances is 100.7 MHz and 90.7 MHz for L_s set at 2.3 pH/sq

Comparison of Bus Resonances predicted by Hybrid Model with Surface Impedance Variation				
Qubit to qubit bus	Bus length (um)	Bus resonances (GHz), L_s - 2.3 pH/sq	Bus resonances (GHz), L_s - 2.8 pH/sq	Measured bus resonances from fabricated chip (GHz)
D4_X	5110.56	7.9483	7.9305	7.843
D2_X	5251.26	7.9899	7.9771	7.941
D1_Z1	5169.39	8.0565	8.0449	7.986
D3_Z1	5096.65	8.1507	8.1412	8.031
D4_Z2	5070.42	8.2425	8.2326	8.14
D2_Z2	5141.83	8.301	8.294	8.19
D1_X	5150.41	8.3347	8.3284	8.234
D3_X	5003.76	8.467	8.4622	8.32

Table 4.4: Comparison of bus resonances numerically computed using the hybrid circuit model by changing the superconducting film property.

and 2.8 pH/sq respectively. This error could be the result of the approximations and inaccuracies in the model due to the following reasons.

a. This numerical computation was done on targetted qubit frequencies. However, in the fabricated physical chip the qubits were found operating at lower frequencies and one of them was not operating. This could influence the loaded resonances of the bus resonators.

b. Inaccurate determination of hanger to readout resonator capacitances. A small change in these capacitances could mean errors in the phase velocity calculation, which in turn gets reflected in the bus unloaded resonances.

c. Errors in surface impedance model.

d. Errors arising due to discretization and numerical errors in FEM simulation.

e. Errors in the fabrication process that results in alteration in the height of the CPW film used to build the qubit structures.

It should also be noted that the lengths of the bus resonators do not vary in a descending order, although their loaded resonances are ordered in an ascending order. This implies that arranging the bus resonances according to the unloaded resonances in a design does not imply that the loaded resonances are found to be in the same order. This change in order is due to the different asymmetric impedance loading on each bus resonators, with respect to each other.

To summarize, the chapter starts by describing a qubit unit cell that can be analyzed using a FEM model. The qubit unit cell serves as the basic block that engulfs several operating parameters in its design. It can be used to construct a larger circuitry that connects multiple qubits with each other along with the measurement circuitry to read the states of the qubits. The chapter then treats the estimation of phase velocity of the resonators in a qubit chip from measurements both by analytic and numerical methods. The estimation of loaded bus resonances in a qubit system is essential for designing the coupling strength. The problem was dealt with by analyzing and building circuit models

to numerically compute the bus resonances. On evaluation, a hybrid circuit model was found to be a good choice in determining the bus resonances of a multi qubit chip.

5

QC ANALYSIS

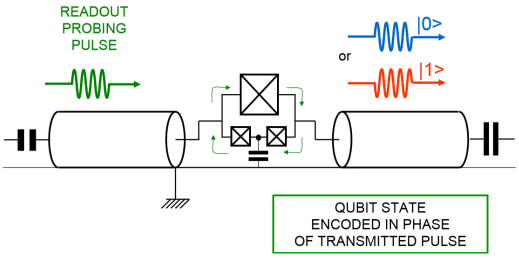

Figure 5.1: Transmon qubit measurement circuitry [21]. A probing pulse is pulsed from a microwave drive line and the state of the qubit can be measured from the readout resonator circuit.

The coupling quality factor is considered to be an important factor in the measurement of the qubit state using a readout resonator. It depends on the ratio of power stored in the resonator to the power dissipated per cycle. It is invariably called as the external or coupling quality factor of readout circuitry and abbreviated as Q_c in this document. The coupling quality of the measuring resonator circuitry affects the resolution and the measuring time of the qubit state. A larger Q_c would provide a good resolution of the measurements and vice versa. However, a larger Q_c has a tradeoff, which results in a larger measurement time. This can have impacts because the coherence of a qubit can change on long measurement time [22]. Hence, an optimal value must be engineered for Q_c. The measurement circuit is such that the qubit is coupled to a readout resonator capacitively, which in turn is capacitively connected to a feed line. This feed line is connected to external measurement circuit, from which microwave pulses can be read. In order to read the state of the qubit, microwave pulses are applied and the state of the qubit is encoded in the phase of the outgoing signal. Measurement of the phase and amplitude of the signal can be used to infer the state [4]. Also, the ac Stark effect can cause a shift in the resonator frequency depending on the state of the qubit, which can be used

to observe the state of qubit. The pulses are applied to the qubit using a microwave driveline. A measurement setup of a qubit is shown in figure 5.1.

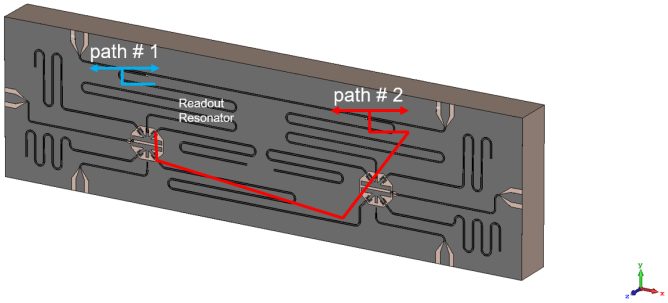

Figure 5.2: Energy leakage paths for the readout resonator circuitry. The path 1 (marked in blue) denotes the primary leakage path, whereas the path 2 (marked in red) denotes the secondary leakage path. FEM model [19].

The coupling quality factor depends primarily on the energy leaked through the capacitance connected to the feed line, i.e., path 1 marked in figure **??**, if the equivalent impedance seen by the resonator from the edge towards the qubit is very high and imaginary in nature. In this case, the energy leaked to the qubit circuit side in one half of cycle is returned back in the following half cycle, considering a lossless circuit. However, under certain conditions significant energy can also be leaked via path 2 marked in figure **??**, which is via the qubit circuitry side seen by the readout resonator. This leaked energy is lost in the measurement resistors through the feed line. The conditions that lead to such losses and factors that affects the Q_c extraction are discussed in this chapter. The term hanger in this chapter denotes the qubit measurement circuit that consists of a feed line that has readout resonator(s) "hanging" from it.

5.1. COUPLING QUALITY FACTOR

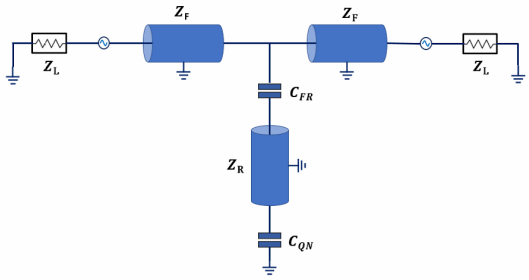

Figure 5.3: Equivalent circuit of starmon qubit readout measurement circuitry

This section attempts to analyze the coupling quality factor for the readout resonator. The readout resonator circuit shown in figure 5.3 is capacitively connected to a feed line on one end and the other end of the resonator is capacitively connected to the qubit. The quality factor of a resonator is given by the amount of time taken for the energy contained in the resonator to reach 1/e of its initial value, multiplied by the resonant frequency.

$$Q = \omega_n \tau_{1/e}$$

For a half wavelength resonator, the maxima of the standing wave is at its edges. Let V be the maxima of the standing wave. The energy that is contained in the capacitive component of the resonator is given by

$$E = \frac{C_l < V^2 >}{2}$$

where C_l is the capacitance of the resonator line. On taking the average of a sinusoidal standing wave inside the resonator, a factor of half is to be multiplied with the above expression. Since, the same amount of energy is to also stored in the inductive component, the total energy remains the same as the above expression. This is also explained in [20].

The power loss is given by considering the power lost though the measurement circuit. At microwave frequencies, the network connected to the readout resonator in the qubit side can be considered as capacitive. This is because in the readout resonator region of operation, the circuit components in the qubit system either exhibit a capacitive impedance or a low inductive impedance, which equivalently results in a capacitive impedance. Hence, the readout resonator can be considered to be connected to a feed line with a capacitive coupling at one end, the other end with a capacitance component that represents the qubit circuitry. If power is assumed to be leaked only from the edge connected to the feed line, then the power loss is given by

$$P =< I^2 > \frac{Z_0}{2}$$

where Z_0 is the impedance of the load on the measurement line, that is matched with the characteristic impedance of the feed line. This implies that the power leaked, is dissipated on these matched impedances. Since the feed line is terminated with two matched impedance loads on either end, the power loss can be rewritten as

$$P =< \left[\frac{V}{\frac{Z_0}{2} + \frac{1}{j\omega C_{FR}}} \right]^2 > \frac{Z_0}{2} \tag{5.1}$$

C_{FR} is the capacitance from the readout resonator to the feed line, marked in figure 5.3. Since $Z_0 << \frac{1}{j\omega C_{FR}}$ the power loss P can be written as

$$P =< [V j\omega C_{FR}]^2 > \frac{Z_0}{2}$$

The time taken for the resonator to reach 1/e of its energy is given by

$$\tau_{1/e} = \frac{E}{P} = \frac{C_l}{[(\omega_{1/2} C_{FR})^2 Z_0]}$$

At the nth resonance, for a half wavelength resonator of length l, having a mode that has v_p phase velocity and Z_l characteristic impedance [20],

$$\omega_n C_l = \frac{\omega_n l}{v_p Z_l} = \frac{2\pi l}{Z_l}$$

$$\omega_n C_l = \frac{n\pi l}{Z_l}$$

The coupling quality factor is given by

$$Q_c = \omega_n \tau_{1/e} = \frac{n\pi}{Z_l \omega_{1/2}^2 {C_{FR}}^2 Z_0}$$

where $\omega_{1/2}$ is the unloaded resonance frequency, which is explained in phase velocity section 4.5. A similar derivation can also be found in [20] for a capacitively coupled resonator circuit. It can be understood that Q_c is sensitive to the values taken by the capacitances of the coupling and frequency of the resonance. It is also affected by the characteristic impedance of the resonator and the feed line characteristic impedance.

5.2. QUBIT READOUT RESONATOR COUPLING QUALITY FACTOR ANALYSIS

As explained in the previous section, the quality factor of a readout resonator depends on the parameters such as the coupling capacitance and the characteristic impedance of the feed line and resonator. It can be shown that the quality factor of a over coupled resonator at loaded resonance f_r is given by

$$Q_c = \frac{f_r}{3dB\ BW}$$

This expression serves to extract the coupling quality factor on observing the readout resonator bandwidth in the measured S parameters in simulation results. In the following section(s), the plots conveying the S parameters of the readout resonator bandwidths implies the value of Q_c.

The parameters that can affect the quality factor for half wavelength readout resonators are

a. The lengths of the transmission line between them.

b. The inter qubit to qubit coupling bus resonators.

c. The Josephson's junction inductance of the qubits.

d. The impedance mismatch of the feed line measurement circuit.

It can be found that all of the above parameters have an impact on the Q_c of the readout resonator and the theme of this chapter works around them. In order to understand the impact of the circuit network, firstly, a simple 2 qubit layout is analyzed and later an analysis for a S7 qubit network is provided.

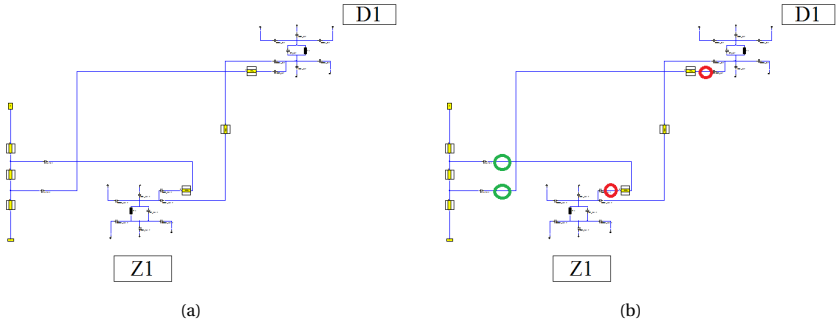

Figure 5.4: a. A 2 qubit equivalent lumped circuit model. b. A 2 qubit layout with edges marked. The green edges represent the edge towards the feed line and the red towards the qubit.

5.3. 2 QUBIT MODEL

A simple 2 qubit model is constructed, as shown in Fig 5.4, is constructed to understand the factors that affects the Q_c. The specifications of each of the qubit are according to the Starmon qubit. To make the discussion clear, the resonator edges are marked in the Figure 5.4b. Edge 1 (green) is close to the feed line and edge 2 (red) is closer to the qubit. Circuit simulations were carried out for the various parameter changes such as

a. Change in the bus resonator frequency that connects the qubits.

b. Change in Josephson's junction inductance.

c. Change in inter hanger length.

d. Impedance mismatch between the feed line and the measuring circuit.

At certain conditions of the above a, b parameters, the effect of the inter hanger length becomes prominent. The effect of impedance mismatch is that resonance curves can be distorted and the effective impedance of the measurement circuit changes. This affects the extraction of Q_c as well as the value of Q_c. All the above parameters are explained in detail in the following sections.

Before the discussion on the different parameters that can change the Q_c of the system, the basic principle behind it is discussed. Consider a readout resonator shown in figure 5.3 with a capacitive joints at its edges. It can be considered as a resonator with only a capacitive loading to the feed line and open circuited at the edge corresponding to the qubit circuitry. This consideration is valid as long as the impedance seen from the edge of the resonator towards the qubit circuitry is very large. However, in a qubit system, one can expect the presence of multiple resonators and often with resonances close to each other. As explained earlier in section 4.6, there are four resonance regimes of a resonator, low inductive, highly inductive, low capacitive and higly capacitive regimes. In the region of highly inductive regime of a resonator (close to resonance), one can expect the inductive component to churn out the capacitive components and change the equivalent capacitance at the edge of the open circuited transmission line. Therefore, it can be understood that the inductive regimes can have an influence in reducing the impedance seen at the edge of the readout resonator. An effective reduction in the impedance can allow a leakage of current from the edge away from the feed line of a readout resonator, through the qubit circuitry, into the neighboring readout resonator(s) and

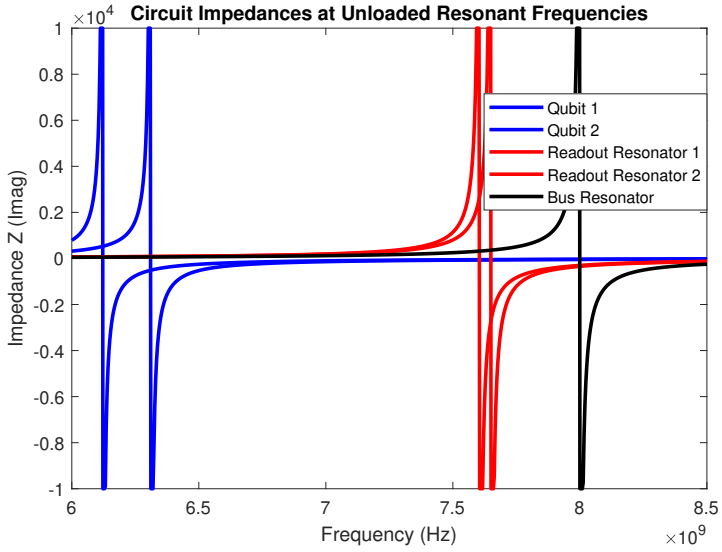

Figure 5.5: Impedances of Resonators in a 2 Qubit System

essentially lost in the measurement impedance circuitry. This conveys that the external or coupling quality factor of a readout resonator can be influenced by the neighboring resonant circuits, under certain conditions. To summarize, if the impedance seen by the edge of the readout resonator away from feed line is significantly imaginary and large, then the readout resonator can be approximated as a resonator with open circuit, at the edge away from the feed line. However, this approximation is no longer valid if a change in impedance allows a leakage of current from the edge of the resonator at the qubit interface to the feed line.

5.3.1. IMPACT OF BUS RESONANCE FREQUENCY

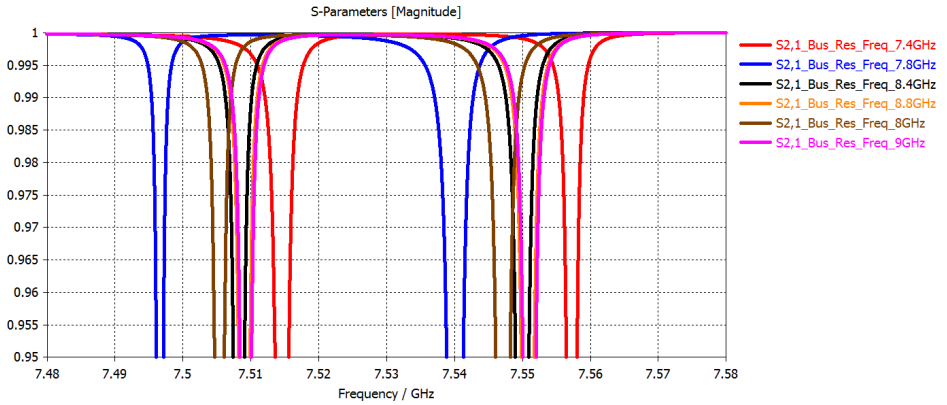

(a)

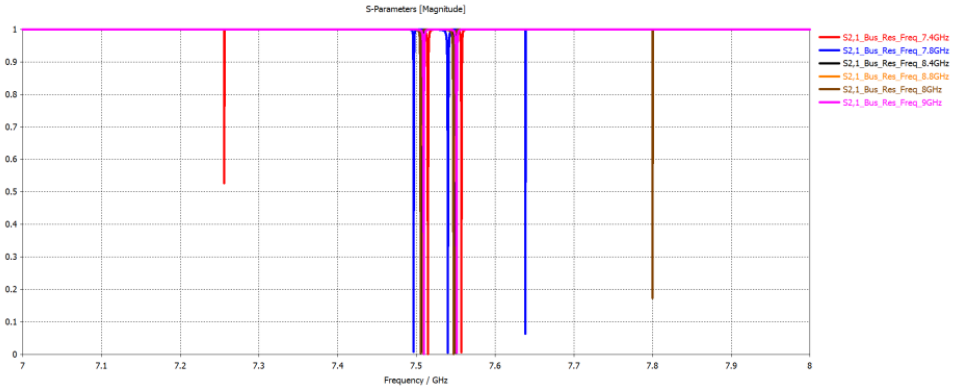

(b)

Figure 5.6: a. Bandwidth of hanger resonances for cases with different bus unloaded frequencies. The inter hanger length is taken as 2100um. The bandwidth of the resonances are clearly affected for the simulation case with the bus unloaded resonance at 7.8 GHz. b. Hanger, bus resonances. The bus resonances for certain simulation cases are observed outside the frequency band of 7.48 GHz to 7.58 GHz in figure 5.6.

In order to understand the impact of the bus resonator between the qubits on the Q_c, the impedance behind edge 2, needs to be understood. The network behind the resonator can be approximated as a capacitive network. If it was of very low capacitance, the readout hanger resonators can be approximated as standalone resonators because of large impedance seen from edge 2. However, the bus resonators found attached to the qubit can influence the impedance of the network to a certain extent. The impedance of a bus resonator, which is an open circuited transmission line can approximately be written as,

$$Z_{in} \approx -\frac{Z_0}{tan(\beta l)}$$

which is in the case of lossless condition. It can be found that if the resonance frequency of the readout resonator is significantly less (atleast 100 MHz) than the bus resonance, then the inductive impedance offered by the bus resonator is considerably less. However, as the resonant frequency of the readout resonator becomes close to the bus resonance (but less than bus resonance), the inductive component offered by the bus resonator becomes larger. This cancels out the capacitance of the network and the effective impedance of the circuit becomes smaller. This can cause the edge 2 of the resonator circuit to have an influence the power loss per cycle of the readout resonator, that can affect the Q_c. A certain amount of current can flow from edge 2 of the readout resonator and flows through the neighboring readout resonator into the measurement feed line.
The characteristics of the readout resonators bandwidth of the 2 qubit network is shown in figure 5.6. It can be observed that the bus resonance frequency plays a role on the width of the bandwidth of the readout resonator resonance. It can be observed that as the bus resonance is brought closer, the bandwidth of the two readout resonators becomes highly asymmetrical. As the bus resonance is kept further away (1GHz) from the readout resonators, the bandwidth of the readout resonators appear not be affected significantly. Since there was not a perfect symmetry in resonance curves observed, it implies that there will be a small leaked current even though the bus resonators are placed at much higher frequency than the readout resonators. The order of currents leaked from both edges in two different bus resonance condition can be noted from an analysis found in appendix B. The relationship between the bandwidth of the resonance and the Q_c was explained earlier in this chapter. It can be observed that as the bus resonance is brought closer, the quality factor of one of the resonator improves and the other degrades. On changing the inter-hanger length when the bus resonances are closer, there is a swap in the bandwidths as shown in figure 5.7. This is a result of superposition of the currents from both edges of the readout resonator on the feed line.

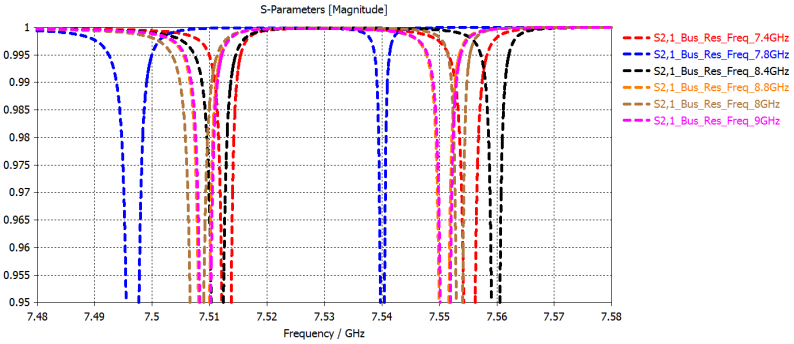

(a)

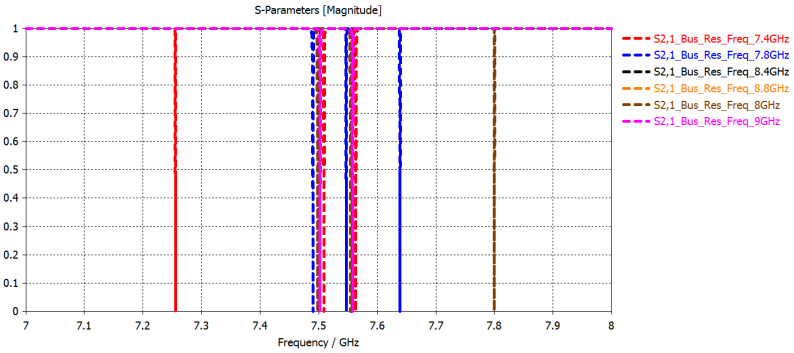

(b)

Figure 5.7: a. Bandwidth of hanger resonances, simulated with inter hanger length 6300um. b. Hanger and bus resonances observed. The hanger resonances are found between the frequency band of 7.48 GHz to 7.57 GHz. The bus resonances are shown in figure 5.7 for certain simulation cases.

5.3.2. EFFECT OF FLUX ON JOSEPHSON'S JUNCTION

The Josephson's junction inductance is varied in a qubit, using flux to change the operating frequency of the qubit. It is of interest to understand the influence on the Q_c by the operating frequency of the qubit, since the operating regime can be tuned. It can be understood that the qubit can be modelled as an LC parallel network. The impedance offered by a parallel LC circuit has four impedance regimes, which depends on the frequencies with respect to the resonant frequency. As explained in the previous section, if a large inductance is offered by the qubit, it can tune out the capacitance seen from edge 2. This can cause the impedance to drop and hence activate a path of current flow that can affect Q_c. However, if the impedance offered by the qubit is of capacitive in nature, i.e., the resonant frequency is less than the readout resonator, then the Q_c should not be affected significantly, as in contrast to the highly inductive regime.

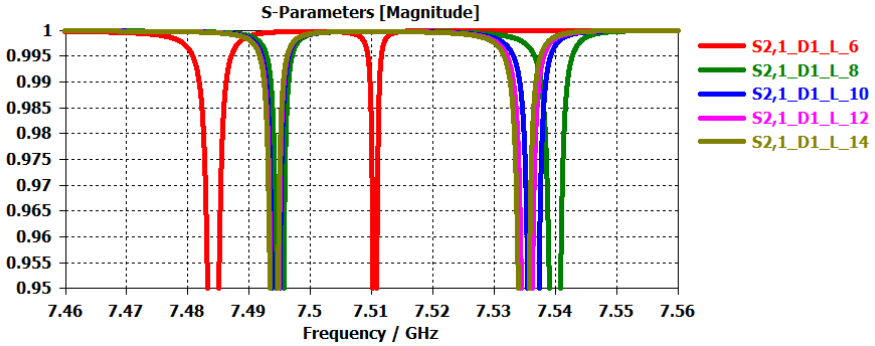

(a)

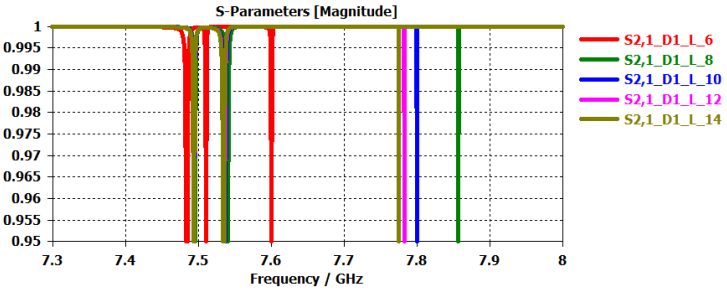

(b)

Figure 5.8: a. Bandwidth of hanger resonances for different Josephson's junction inductances. The unloaded bus resonance is kept at 8 GHz. b. Resonances of qubit, readout resonator and bus resonator. The qubit resonance is observed near 7.6 GHz for the simulation case of junction inductance at 6 nH. The resonances observed between 7.48 GHz to 7.55 GHz are of readout resonances. The resonances observed between 7.75 GHz to 7.9 GHz are the bus resonances.

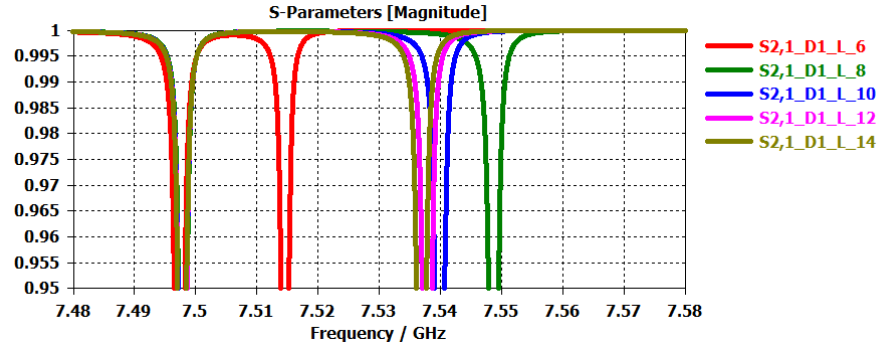

(a)

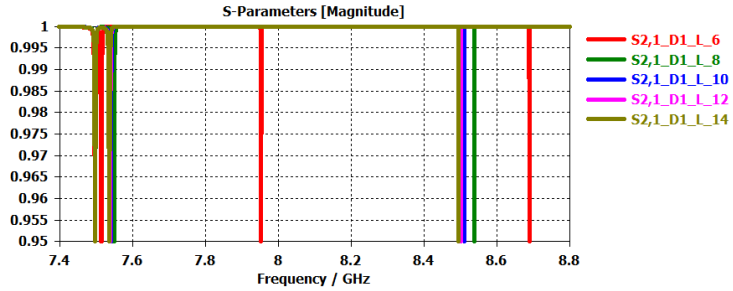

(b)

Figure 5.9: a. Bandwidth of hanger resonances for different Josephson's junction inductances. The unloaded bus resonance is kept at 8.8 GHz. b. Resonances of qubit, readout resonator and bus resonator. The qubit resonance is observed between 7.8 GHz to 8 GHz for the simulation case of junction inductance at 6 nH. The resonances observed between 7.48 GHz to 7.56 GHz are of readout resonances. The resonances observed between 8.4 GHz to 8.8 GHz are the bus resonances.

From simulation plots shown in figure 5.8, it can be found that there is a significant effect on Q_c, when the qubit is operated at frequencies greater than the readout resonator. This effect is more prominent when the bus resonator used for qubit to qubit coupling resonates close to the readout resonator as shown in figure 5.8a and figure 5.9a. This situation activates the path between readout resonator 1 and 2, and can cause a leakage in power from edge 2. This effect can be noted from the difference in the bandwidth of the readout resonators when the unloaded resonant frequency of bus resonator is designed at 8 GHz and 8.8 GHz respectively. In case of unloaded 8 GHz bus resonance, the asymmetry in the bandwidth of the readout resonators resonance is prominent compared to the similar condition at 8.8 GHz unloaded bus resonance case. This is because of the combined inductive impedance due to the qubit and the bus resonator. The inductive regime of the bus resonator being more prominant at 8 GHz unloaded resonance than at 8.8 GHz on the readout resonator frequency causes an increased asymmetry. It must be understood that although keeping the bus resonance further apart (as in 8.8 GHz case), if the qubit resonance is operated at higher frequencies of qubits, there would be an effect on Q_c. However, this is taken care of in the design by operating the qubits at resonant frequencies less than the readout resonator resonance.

5.3.3. INTER HANGER LENGTH IMPACT

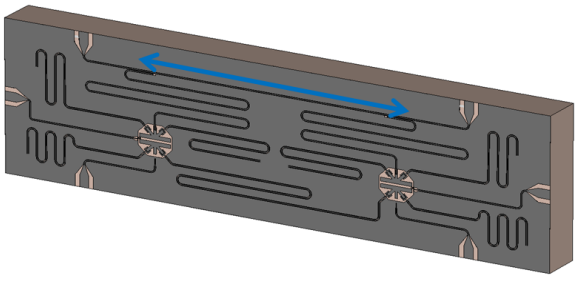

Figure 5.10: Inter hanger or inter readout resonator length on the feed line, marked (in blue) for a 2 qubit [19] system.

The readout resonators for a qubit system is typically designed to be situated on different positions of the feed line as shown in figure 5.10. For two sinusoidal signals that originate at two different coordinates along the same dimension, can be rewritten as the two signals with phase differences. The same principal can be used in this analysis. The signals that originate at different coordinates of z, can be rewritten as a delayed version, w.r.t the signal at the origin. This can be written as

$$V(z) = \sum_i V_i^+ e^{-j\beta_i(z-z_i)} + \sum_i V_i^- e^{j\beta_i(z+z_i)}$$

$$I(z) = \sum_i I_i e^{-j\beta_i(z-z_i)} + \sum_i I_i e^{j\beta_i(z+z_i)}$$

where z_0 is the origin and can be taken as reference hanger location, whereas z_i can be considered as the length between the reference hanger and to the considered hanger distance. It can be noted that the phase difference induced by the location of the hanger can impact if the amplitude of the signals originating is significant. This effect due superposition can influence the power loss. In case the signals are sourced from the both edges in the readout resonator, the same frequency components can constructively interfere or destructively interfere, affecting the Q_c. A demonstration of this effect is documented in Appendix B.

From simulation, it can be observed as shown in figure 5.11 that the change in line length has an impact on the bandwidth of the resonance. In order to understand or relate the wavelength of the waves in the feed line, first a brief discussion is made relating the wavelength and effective dielectric permittivity. For a CPW line placed on an infinitely thick dielectric substrate of permittivity ϵ_r, the effective dielectric permittivity is given by [17]

$$\epsilon_{eff}^{CPW} = \frac{1}{2}(\epsilon_r + 1)$$

The dielectric permittivity of the substrate was found to be as 11.45 from measurements and the corresponding effective dielectric permittivity can be found as 6.2250. Since the CPW lines support TEM propagation, the transmission line theory can be used. The wavelength propagating in the feed line can be found as

$$\lambda = \frac{c}{\sqrt{\epsilon_{eff}^{CPW}} f_r}$$

where c is the velocity of propagation in free space and f_r is the resonant frequency of the readout resonator. On substituting the relevant parameters into the above equation, the wavelength is found to be of the order 15.9 mm for a resonator frequency of 7.54 GHz. Simulations for two different inter-hanger lengths of 2.1 mm and 6.3 mm were chosen to show a demonstration of the effect of superposition.

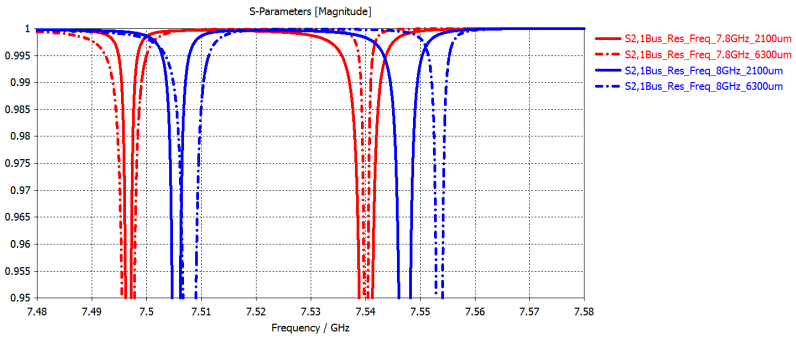

Figure 5.11: Bandwidth of hanger resonances with bus resonance variation for different feed line length

It can be noted that in figure 5.11, on changing the inter hanger length, the bandwidth of the resonances swap. This is prominent as the bus resonator between the qubits resonates closer to the readout resonances. As the bus resonator is brought closer to the readout circuitry, the magnitude of the current leaked from edge 2 becomes significant and the effective magnitude of the current passing through the measurement resistors changes according to the inter hanger lengths. The same frequency components leaked from edge 1 and 2, could constructively or destructively interfere and contribute to the Q_c, appropriately. This is the reason for the swap in the bandwidths of the individual readout resonators as the hanger lengths are changed.

5.3.4. IMPEDANCE MISMATCH BETWEEN THE FEED LINE AND THE MEASURING CIRCUIT

The transmission line theory conveys that there would be reflections at a mismatched boundary. During measurements, although the termination is set at the designed characteristic impedance of the feed line, there would be a mismatch. The mismatch could be due to the physical connections or difference in characteristic impedance of feedline and external measurement circuit. This causes part of the voltage signals to be reflected back and would cause a standing wave in the feed line. It distorts the bandwidth curve

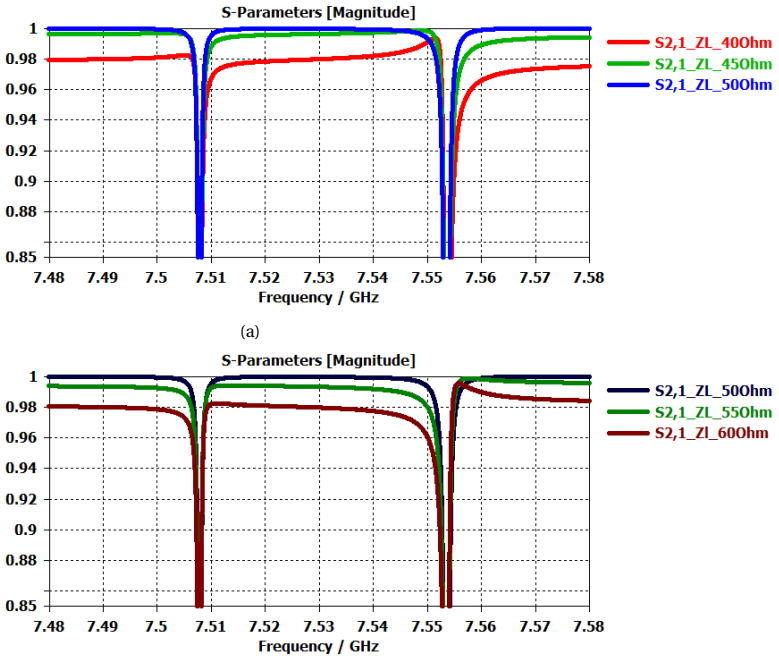

Figure 5.12: Bandwidth of hanger resonances on feed line impedance mismatch. a. Port impedances (port 1 and 2) set at lower impedance than the feed line. The characteristic impedance of the feed line is set at 40 Ω. b. Port impedances set at higher impedance than feed line characteristic impedance (40 Ω).

in S parameters of the readout resonators. This effect is demonstrated using simulation shown in figure 5.12, by setting termination impedances at lower and higher impedance than the characteristic impedance of the feed line. As it can be observed the bandwidth of the resonances are distorted, which can affect the Q_c extraction. A high mismatch can distort the S parameter curve to a large extent and vice versa. Since the mismatch will change the input impedance of the transmission line, the Q_c will also be affected. This aspect is discussed in detail in section 5.5.

5.4. Q_c SIMULATION ANALYSIS OF A S7 LAYOUT

In order to understand the circuit parameters that affects the Q_c of a larger circuit, a Starmon S7 hybrid layout was chosen. It is shown in figure 5.13. This circuit model is larger than the simplified model used in the previous section. The previous section conveys that the targeting of bus resonances has a major impact on Q_c. Hence, this section attempts to understand the same on the S7 layout. It should be noted that there are a disproportional number of readout resonators on the two measurement feed lines. From Q_c measurements on a fabricated chip, it was puzzling to observe that although each of the readout resonator design were symmetrical, each readout resonator had a Q_c that was not the same. The measurements are tabulated in table 5.1. As explained in previ-

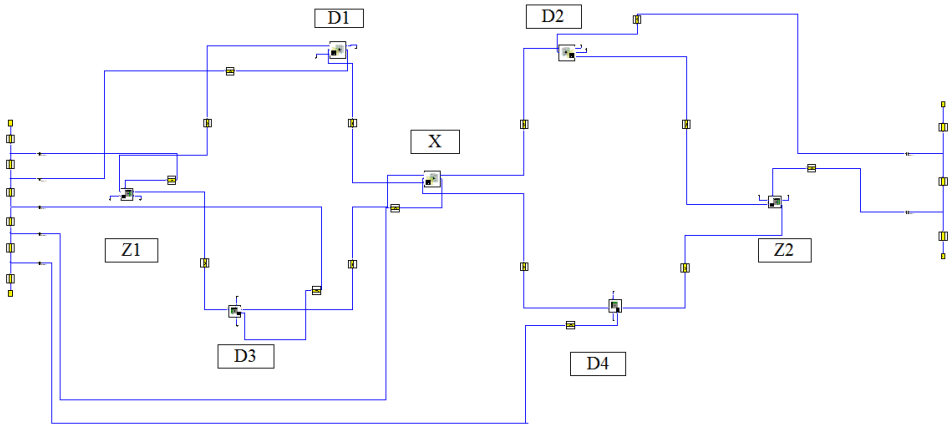

Figure 5.13: S7 layout used for analysing Qc

ous sections, Q_c depends on the hanger capacitances. Although each of the resonators in the fabricated chip were designed to have similar capacitances adjusted slightly from each other, with respect to their individual resonant frequencies to provide the same Q_c. It can be noted that on hanger 1, the Q_c is almost in similar range, except one. On the other hand, on hanger 2, there is a difference between the Q_c of the two readout resonators compared to hanger 1. The readout resonators and bus resonators measured in this chip are tabulated in table 4.1 and 4.3. The minimal frequency distance between the bus resonators and readout resonators is found to be 343 MHz. In the following section, an exploration of the impact of the hanger resonator bandwidths by the back circuit (qubit network) is carried out by varying the bus resonances. Also, the impact of the measurement mismatch effect on the bandwidth of the resonance is studied.

Qc Measurement from a S7 Chip		
Hanger	Qubit Readout Resonator	Measured Qc
Hanger1	D1	15000
Hanger1	Z1	31000
Hanger1	X	21000
Hanger1	D3	21000
Hanger1	D4	23000
Hanger2	D2	25000
Hanger2	Z2	9700

Table 5.1: Q_c measurement from a S7 chip designed to have similar or equal Q_c

5.4.1. EFFECT OF BUS RESONATORS ON Q_c FOR A S7 CIRCUIT

It was shown in the previous section that the bus resonances can have an effect on the Q_c of the readout resonators. This drives the problem statement of understanding the effect of bus resonance on a larger network such as a S7. In this section, the effect of the placement of the bus resonance on a frequency scale, with respect to the readout resonators is studied.

In designing superconducting resonators, often if the material property is not accurately determined, then the fabricated chip would exhibit resonances at global shifted frequencies than intended. This is because of errors in determining the kinetic inductance component offered by the superconducting material. Also, the height and width of the circuitry can vary in localized areas due to fabrication process. This can also cause a change in the geometrical inductance and capacitances of the circuitry, which in turn affects the resonances. If the minimal frequency gap between the readout resonances and the bus resonances that can have a minimal impact on Q_c is known, then the designers can target the bus resonances accordingly with the required slack.

In order to determine the influence of Q_c on the minimal frequency gap between the readout resonances and the bus resonances, a parametric sweep was conducted at selected intervals. By design, the readout resonators are designed to be at a frequency below the bus resonances. The minimal frequency gap is calculated by taking the frequency distance between the highest readout resonance and the least bus resonance frequency. The bus resonances are initially kept at the targeted frequency and then linearly varied globally to come close or move further apart from the readout resonances. Since the Q_c is proportional to the bandwidth of the resonance, it is observed on each iteration of the parametric sweep.

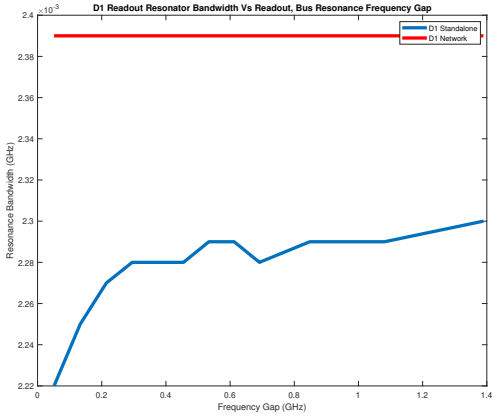

(a)

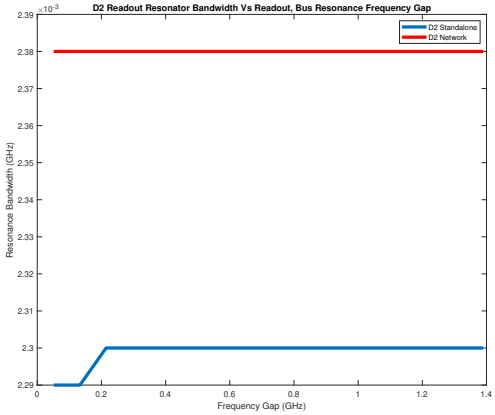
D2 Readout Resonator Bandwidth Vs Readout, Bus Resonance Frequency Gap
×10^-3
D2 Standalone
D2 Network
Resonance Bandwidth (GHz)
Frequency Gap (GHz)

(b)

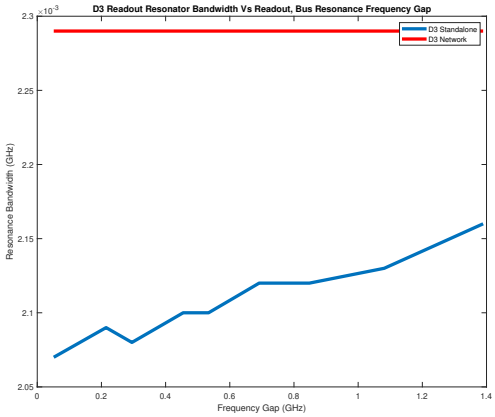
D3 Readout Resonator Bandwidth Vs Readout, Bus Resonance Frequency Gap
×10^-3
D3 Standalone
D3 Network
Resonance Bandwidth (GHz)
Frequency Gap (GHz)

(c)

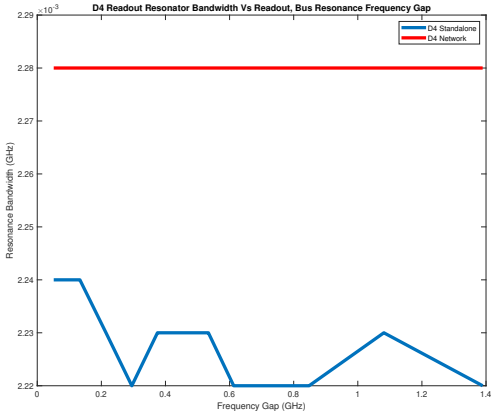
D4 Readout Resonator Bandwidth Vs Readout, Bus Resonance Frequency Gap
×10^-3
D4 Standalone
D4 Network
Resonance Bandwidth (GHz)
Frequency Gap (GHz)

(d)

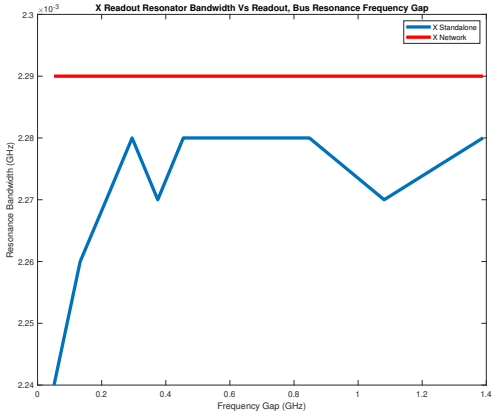

(e)

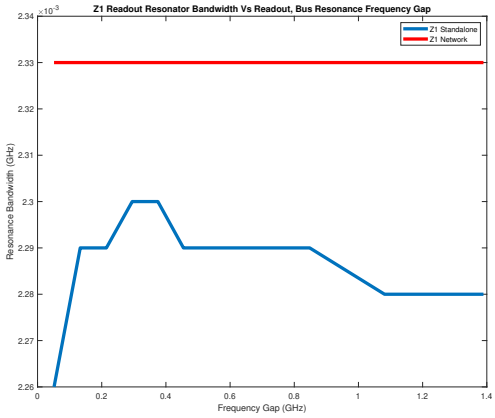

(f)

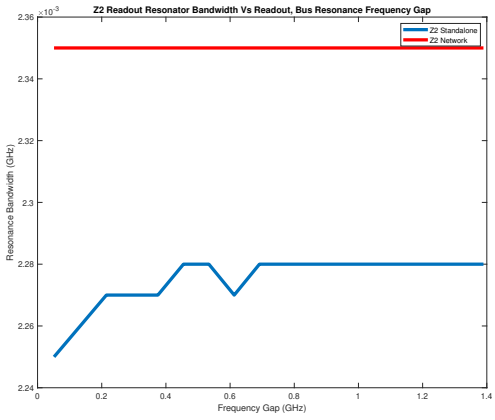

(g)

Figure 5.14: a,b,c,d,e,f,g are the plot of the bandwidth of the qubit readout resonance versus the minimal frequency gap between the readout resonators and the bus resonators. The bandwidth recorded in the figures are observed at .98 of $|S_{12}|$. It can be observed that a frequency gap less than 100 MHz will start impacting the resonance bandwidth.

It can be observed from figure 5.14, that as the frequency gap between the readout and bus resonators become smaller than 100 MHz, there is an impact. Beyond 400 MHz gap, the bandwidth appears to not have a significant change, but does not converge towards the standalone resonance condition. This is because there is a current, which is small that is leaked from the readout resonator edge towards the qubit. This cannot be totally reduced by moving the bus resonances much higher in design. This implies that the impedance seen from the edge of the resonator towards the qubit is large but finite. This effective impedance allows a small current to leak to the feed line through the neighboring readout resonator(s) connected on the same feed line.
It is of interest to understand the impact of the inter hanger lengths with respect to the circuit bus resonances. On observing figure 5.14, it can be understood that there can be an impact on the Q_c of readout resonators as the frequency gap between the bus and readout resonators becomes less. An analysis on the impact of the change in the inter-hanger lengths is needed to understand its effect on the resonance bandwidth characteristics. Two cases are studied. In case 1, the inter-hanger lengths on hanger 1 are 4000 um, 2500 um, 1850 um, 2200 um and the inter-hanger length on hanger 2 is 4000 um. This can be treated as inter-hanger length combination 1. This was the standard inter-hanger lengths used in the S7 chip used as a reference in this work. A new combination termed as inter-hanger length combination 2 has on hanger 1, the inter-hanger lengths as 6500 um, 8500 um, 4850 um, 6200 um and on hanger 2, the inter hanger length as 7000 um. Simulation results for targeted bus resonances of 460 MHz apart from readout resonances and a shifted bus resonance of 20 MHz apart from readout resonances are shown in figure 5.15.

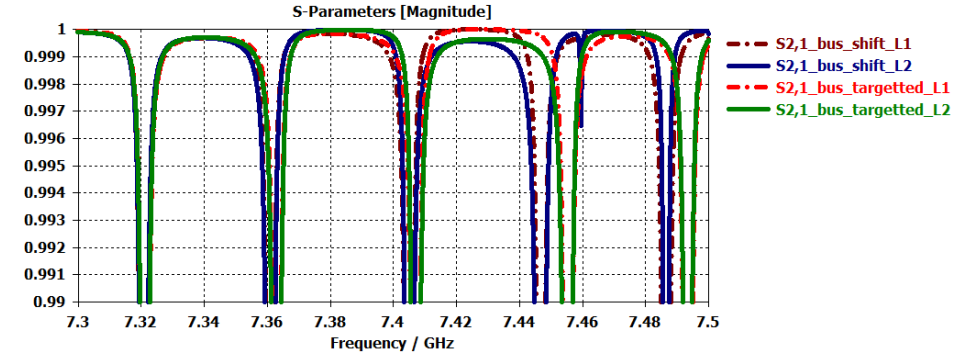

(a)

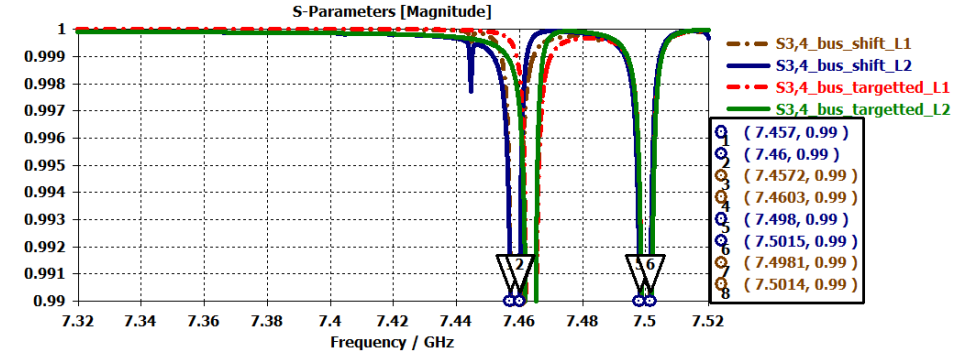

(b)

Figure 5.15: Readout resonances for targeted bus resonances of 460 MHz apart and with a global bus resonances shift that is 20 MHz apart between readout resonances and bus resonances. L1 and L2 denotes the inter hanger line length combination. a. Hanger 1 resonances. On observing the 4th and 5th resonances, one can observe that there is a swap between the bandwidths on changing inter hanger line length combination L1 and L2. This is a result of superposition of the waves on the hanger feed line. Also, it can be noted that the bandwidth of the bus shifted condition is different than the targeted condition, predominantly on resonance 4 and 5. b. Hanger 2 resonances. It can be observed that there is a swap in the bandwidth of the resonance bandwidths between both the resonances as the line length is swapped.

It can be observed that there is a swap in the bandwidths of the readout resonances on hanger 1 and 2 on changing the inter-hanger length combinations. This shows that there is a current leakage from the back circuit into the feed line. It can be understood that inter hanger lengths can cause a increase or decrease in the Q_c due to the superposition principle, in the bus shifted condition.
To summarize, the bus resonances does not change the Q_c unless they are brought in frequency close to the readout resonators by 100 MHz or less. The asymmetry in the measurements of the physical chip does not explain the difference because there was 343 MHz in resonance frequency.

5.5. EFFECT OF MISMATCHED IMPEDANCE ON MEASUREMENT CIRCUITRY

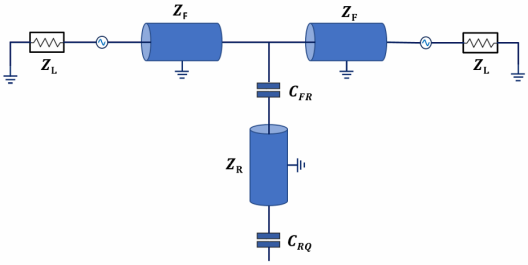

(a)

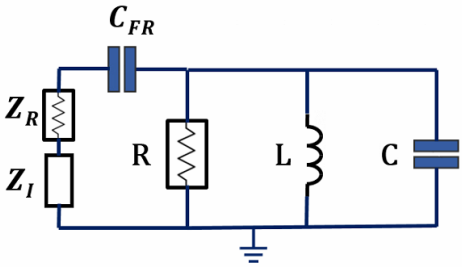

(b)

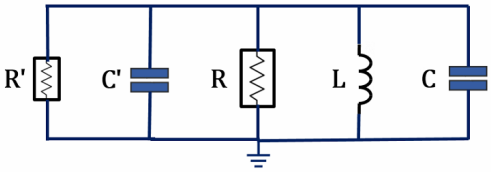

(c)

Figure 5.16: a. Circuit diagram of a single half wavelength readout resonator on a feed line. b. The equivalent circuit diagram of the single half wavelength readout resonator at resonance. c. A Norton equivalent circuitry of the single half wavelength readout resonator from figure 5.16b at resonance.

An impedance mismatch on the measurement circuitry can cause reflections in the boundary, which can distort the resonance curves. Hence, an investigation into the effects of the impedance mismatch is conducted in this section. A typical measurement circuitry of a qubit is shown in figure 5.16 for which the following parameters are defined. β is the propagation constant of the feed line, l_1, l_2 are the lengths of the feed line on either side of the readout resonator, Z_F, Z_L are the characteristic impedance of the feed line and the matched load of measurement circuitry respectively, Y is the admittance of the readout

resonator. In the case of unmatched condition the input impedance of the measurement line with equal line lengths on both sides, can be written in terms of real and imaginary components as

$$Z_R = \frac{{Z_F}^2 Z_L}{2}\left\{\frac{1+\tan^2(\beta l)}{{Z_F}^2 + {Z_L}^2\tan^2(\beta l)}\right\}$$

$$Z_I = \frac{Z_0}{2}\left\{\frac{Z_F^2 - Z_L^2}{\frac{Z_F^2}{\tan(\beta l)} + Z_L^2\tan(\beta l)}\right\}$$

In order to analyse the circuit further, the series impedance in figure 5.16b, consisting of the resistive component Z_R and the imaginary components $Z_I + \frac{1}{j\omega C_{FR}}$ can be converted in terms of Norton equivalent parallel circuit shown in figure 5.16c. The terms R, L and C in the figure 5.16 are defined in the section 3.5.4. The quality factor Q of the series circuit to be transformed can be found as the ratio $\frac{Z_I - \frac{1}{\omega C_{FR}}}{Z_R}$, which allows the reactive component of such a transformation to be given as $\left[Z_I - \frac{1}{\omega C_{FR}}\right]\frac{Q^2+1}{Q^2}$. If the quality factor Q is high, it can be seen that the series to parallel conversion of the imaginary impedance is the same. The resistive R' in figure 5.16c can be calculated as $Z_R(Q^2+1)$, which will be a large component if Q is large.

Under certain conditions, it can be shown that the transformed imaginary component can be represented by only the capacitive component C_{FR}, i.e., $C' = C_{FR}$. This is valid for a C_{FR} range of order $1e^{-15}$, a feed line characteristic impedance range of 40 to 50 Ohm and the mismatch to be ± 10 Ohm, which are typical parameters in a qubit design. It is because the equivalent capacitive component that can be represented from the transmission line imaginary impedance due to mismatch is large. A smaller valued capacitance typically designed for C_{FR} dominates over the larger capacitance in series. Taking these factors into consideration, the resonance condition of the of the circuitry in figure 5.16c is given by $\frac{1}{\sqrt{L(C+C')}}$.

However, it is not the case always in which the imaginary component of the transform can be represented by C_{FR}. It can be shown for a feed line impedance of 400 Ohm, Z_L of 10 Ohm, line length of 3900 um constructed with a dielectric permittivity of 6.25, the resonance changes from a setup with matched impedance. This shows that the imaginary component induced by the mismatch, can affect the equivalent capacitance, which in turn affects the resonance frequency.

The change in Z_R in the case of mismatched impedance can affect the Q_c. An increase in the resistive component can result in the dissipation of more power and vice versa. For special cases of half wavelength and quarter wavelength of the transmission line, the input impedance changes to Z_L and $\frac{Z_F^2}{Z_L}$. Since there is a change in resistance (real part of transmission line input impedance) the Q_c will be affected in case of a mismatch in measurement circuit. This will depend on the length of the line from the resonator to the mismatched load.

The S_{21} of the circuit shown in figure 5.16 can be written as

$$S_{21} = \frac{2}{2\cos(\beta l_1 + \beta l_2) + (\frac{Z_F}{Z_L} + \frac{Z_L}{Z_F})\, j \sin(\beta l_1 + \beta l_2) + Y_{fact}} \tag{5.2}$$

$$Y_{fact} = Y\left(jZ_F \sin(\beta l_1)\cos(\beta l_2) - \frac{Z_F^2}{Z_L}\sin(\beta l_1)\sin(\beta l_2) + Z_L \cos(\beta l_1)\cos(\beta l_2) + jZ_F \cos(\beta l_1)\sin(\beta l_2)\right)$$

In case of a perfect match between the feed line and the measurement circuitry, the S_{21} can be written as

$$S_{21} = \frac{2}{2\cos(\beta l_1 + \beta l_2) + 2j\sin(\beta l_1 + \beta l_2) + Z_F Y(\cos(\beta l_1 + \beta l_2) + j\sin(\beta l_1 + \beta l_2))} \tag{5.3}$$

The S_{21} relationships are derived in appendix C. At resonance for a lossless resonator, in a perfectly matched measurement system, the S_{21} tends to zero because the denominator of equation 5.3 becomes very large due to the admittance Y tending to a large value. At frequencies further away from resonance, the magnitude of S_{21} can be found to be close to or 1, since Y is zero or very small value. A description of Y is found in appendix C. In the case of mismatch, at frequencies further away from resonance, there will be a distortion due to the factors $\frac{Z_L}{Z_F}$ and $\frac{Z_F}{Z_L}$. This will affect the bandwidth starting from the edges of the resonance bandwidth. As the mismatch is increased, a larger portion of the resonance curve will be affected. If there are losses, then at resonance, Y will no longer be a large value. This implies that with attenuation losses, the depth of the resonance bandwidth will be affected by the impedance mismatch. This can be inferred from equation 5.2. In the case of mismatch, the line lengths on either side of the resonator will play a role, both in lossy and lossless condition. A special case of considering the total length of line to be half wavelength (or even multiples) of the resonator's resonance frequency on the line results in the cancelation of the term $(\frac{Z_F}{Z_L} + \frac{Z_L}{Z_F})\, j \sin(\beta l_1 + \beta l_2)$ in equation 5.2. The product of propagation constant and line length results in π, which cancels the sine term. This ensures that as $Y = 0$, there is no distortion. However, as $Y \to 0$, the component due to Y_{fact} in equation 5.2, still plays a role in altering the bandwidth. Similarly, a significant distortion can be observed if the feed line length is quarter wavelength (or odd multiples) of the resonator's resonance frequency. This stems from the product of propagation constant and line length results in $\frac{\pi}{2}$.

The simulations for arbitrary inter-hanger lengths were conducted for hangers under lossless and lossy conditions. The lossy condition needs to be understood because in measurements of a fabricated chip, one does not see the minima of the S parameters at 0, which implies losses. The simulation involves varying the inter-hanger lengths arbitrarily to understand the effects of the mismatch in the resonances. In the simulation, 3 different line combinations of inter hanger lengths were chosen such that the total length of the hanger 1 and 2 in feed line was less than 12 mm and 8 mm respectively. The line lengths used in the simulations are comparible to the wavelengths, i.e., the transmission line used has a permittivity of 6.25 for which a length of 8000 um corresponds to the half wavelength of a 7.5 GHz resonance frequency.

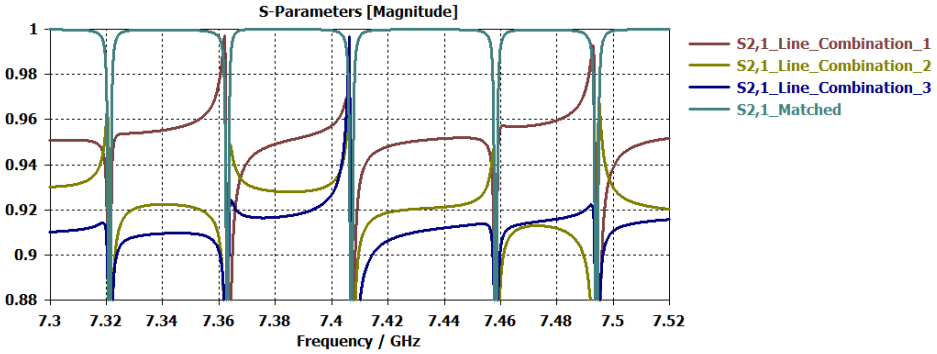

(a)

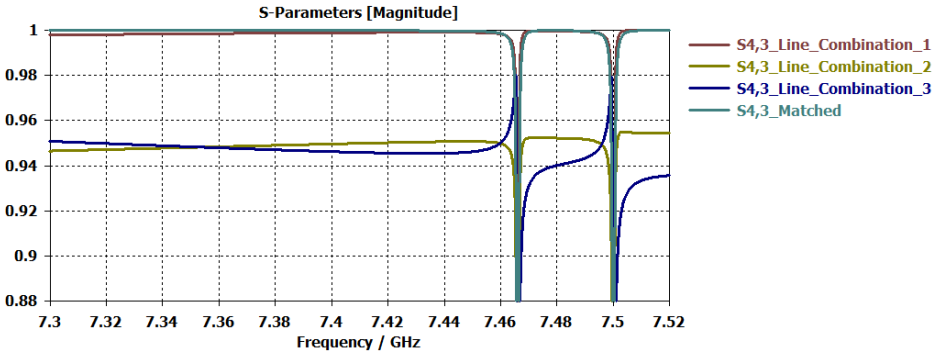

(b)

Figure 5.17: a. Hanger 1 resonances for different inter-hanger lengths in a lossless resonator circuit. b. Hanger 2 resonances for different inter-hanger lengths in a lossless resonator circuit.

It can be observed in figure 5.17, there are distortions on the resonance curve at the edges for the lossless condition. But the resonance depth is not affected, since the admittance of the resonator circuitry at the resonance is very high in lossless condition. This is as predicted by equation 5.3.

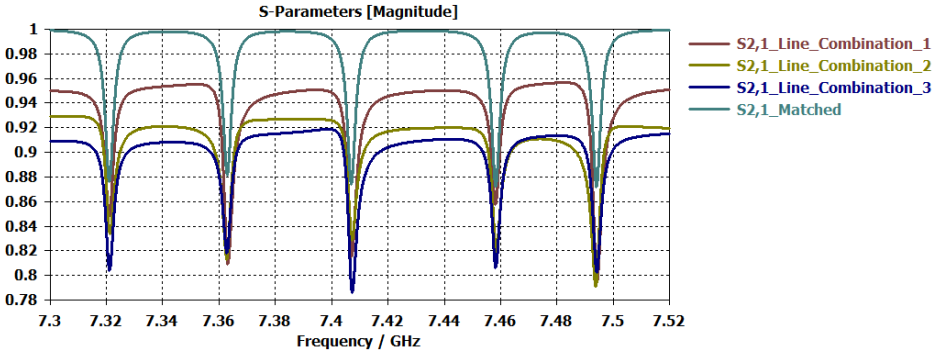

(a)

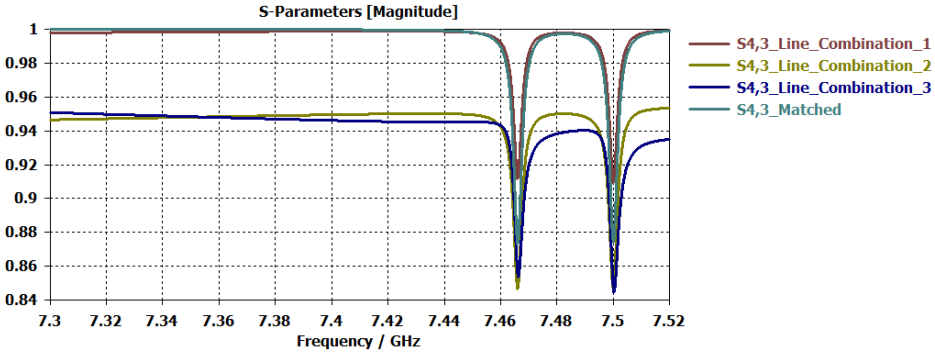

(b)

Figure 5.18: The attenuation constant in the resonators were kept high i.e., 1, to understand the impact of measurement mismatch during lossy condition on the resonance curves. a. Hanger 1 resonances for different inter hanger lengths. b. Hanger 2 resonances for different inter hanger lengths

In case of mismatch of impedance for a lossy resonator circuit, there are distortions on the resonance curve at the edges as well as on the depth of the resonance curve, shown in figure 5.18 for different line combinations. The change in depth can be a result of the distortion as well as the change in Q_c. Q_c will affect the depth in poor internal quality factor condition. Since the mismatch can affect the Q_c as well as distort the S parameters, it could be the reason that affects the Q_c extraction in the measurement chip. In hanger 2, the line combination 1 in figure 5.18b had the feed line length equal to half wavelength of the resonance (8000 um). It can be seen that the distortion is minimal at the edges, however the bandwidth is affected with respect to the matched condition. This change in bandwidth is a result of the term Y_{fact} in equation 5.2, which suffers a change due to impedance mismatch and dependent on line length on either sides of the resonator. The change in bandwidth is a result of change in Q_c. The line combination 1 in 5.18b refers to a line half wavelength condition. The input impedance seen by the resonator in this line combination case is smaller than the matched condition. This results in an increase in Q_c and hence the bandwidth size was found to be reduced in figure 5.18b, line combination 1.

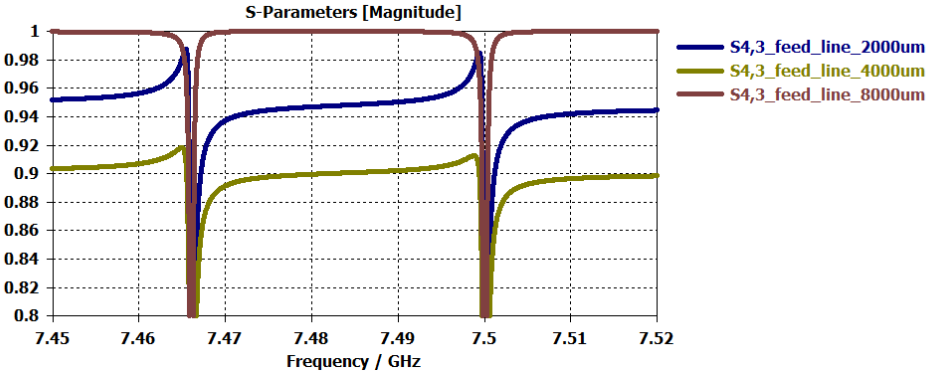

(a)

Figure 5.19: Simulation results of a mismatched hanger 2 resonances (lossless condition), with total measurement line length (sum of feed line and the connecting measurement lines) varied from 2000 um, 4000 um and 8000 um. The dielectric permittivity of the transmission lines in simulation was chosen to be 6.25, results in a wavelength of 16 mm travelling in it at a frequency of 7.5 GHz.

The simulation results of special cases of the total line lengths of quater wavelength, half wavelengths are shown in figure 5.19. It can be seen that there is minimal distortion at the edges of the resonance for half wavelength line length. In this simulation the line is constructed with a transmission line of permittivity of 6.25 for which the length of 8000 um corresponds to the half wavelength of a 7.5 GHz resonance frequency. It can also be observed from figure 5.19 that the change in the height of the resonance curve is most for the quarter wavelength case.

To summarize, the measurement circuitry of a qubit system could suffer an impedance mismatch. This will result in standing waves that can distort the resonance curves of the readout resonators. It can be inferred that the asymmetrical results observed in Q_c for readout resonators on both hangers from the fabricated surface 7 chip can be attributed to the different line lengths under the mismatched impedance condition. Different feed line lengths on both hangers would have resulted in distorting the resonance curves in a different manner as well as changed the Q_c. This attributed to the errors in the Q_c extraction process, resulting in asymmetrical Q_c values found in table 5.1.

5.6. HANGER CAPACITANCE EXTRACTION USING S PARAMETERS

The capacitance between the readout resonator and the feedline is of importance to target the Q_c. In this section for extraction of the hanger capacitance using S parameters is treated. A 3D FEM model of the hanger is constructed and ports are placed at the feed line interfaces and on the readout resonator shown in figure 5.21, using which parameter extaction can be done by simulations. The characteristic impedance of the feedline and the resonator may or may not be the same. Extraction for both these conditions are discussed in the following sections.

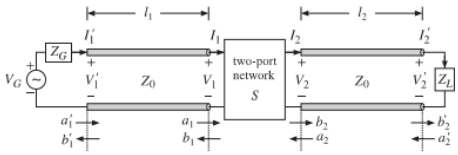

Figure 5.20: S Parameter Test Setup [24]

A typical representation of a linear two port system is shown in 5.20, from [24]. In order to characterize a linear 2 port circuit, several circuit characteristics were developed such as impedance matrix, admittance matrix, transfer matrix and scattering matrix. It is of importance to understand them because they are useful in parameter extraction process. If an impedance model of a circuitry is known, the equivalent parameters in the circuit can be extracted from S parameters. Some fundamental relationships such as impedance matrix, transfer matrix and scattering matrix for the two port network is given by

$$\begin{bmatrix} V_1 \\ V_2 \end{bmatrix} = \begin{bmatrix} Z_{11} & Z_{12} \\ Z_{21} & Z_{22} \end{bmatrix} \begin{bmatrix} I_1 \\ -I_2 \end{bmatrix}$$

$$\begin{bmatrix} V_1 \\ I_1 \end{bmatrix} = \begin{bmatrix} A & B \\ C & D \end{bmatrix} \begin{bmatrix} V_2 \\ I_2 \end{bmatrix}$$

$$\begin{bmatrix} b_1 \\ b_2 \end{bmatrix} = \begin{bmatrix} S_{11} & S_{12} \\ S_{21} & S_{22} \end{bmatrix} \begin{bmatrix} a_1 \\ a_2 \end{bmatrix}$$

5.7. ESTIMATION OF CAPACITANCE OF COUPLING WITH EQUAL PORT CHARACTERISTIC IMPEDANCES

The parameter extraction of the hanger capacitance for the same characteristic impedance exhibited by the resonator and the feed line is discussed here. In order to derive S_{31}, the second port shown in figure 5.21 is to be terminated by a characteristic impedance Z_0. The circuit equivalent representation using only two port is shown in 5.22. Substituting the values for Z_1 as 0, Z_2 as $j\omega C$ and Z_3 as Z_0 in the ABCD matrix, one can deduce the following relationship.

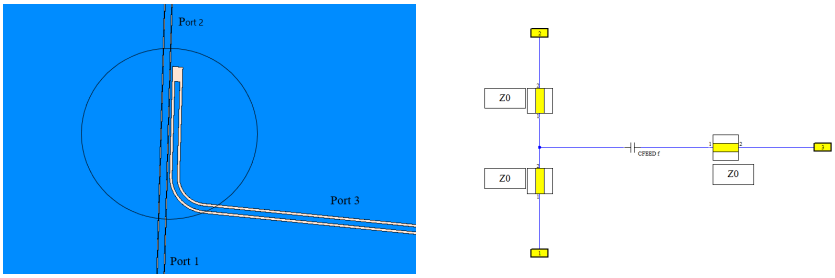

Figure 5.21: Readout resonator coupling with matched characteristic impedance Z_0 on port 1,2 and 3.

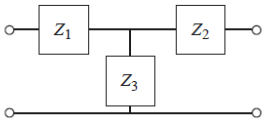

$$A = 1 + \frac{Z_1}{Z_3} \qquad B = Z_1 + Z_2 + \frac{Z_1 Z_2}{Z_3}$$
$$C = \frac{1}{Z_3} \qquad D = 1 + \frac{Z_2}{Z_3}$$

Figure 5.22: Pi Model [23] used in readout resonator coupling S parameter modelling

5

$$S_{31} = \frac{j\omega C Z_0}{\frac{3}{2} j\omega C Z_0 + 1}$$

$$C = \frac{S_{31}}{(1 - \frac{3S_{31}}{2}) i\omega Z_0}$$

This relationship is also found in [27].

5.8. ESTIMATION OF CAPACITANCE OF COUPLING WITH UNEQUAL PORT CHARACTERISTIC IMPEDANCES

5.8.1. 2 PORTS WITH UNEQUAL CHARACTERISTIC IMPEDANCES

First the derivation is done for two ports and then it is applied in the context of 3 ports as in 5.23. In order to deduce this relationship, one needs to consider the travelling wave variables a_1, a_2, b_1 and b_2. They are defined as follows

$$a_1 = \frac{V_1 + Z_0 I_1}{2\sqrt{Z_0}} \qquad b_1 = \frac{V_1 - Z_0 I_1}{2\sqrt{Z_0}}$$

$$a_2 = \frac{V_2 - Z_1 I_2}{2\sqrt{Z_1}} \qquad b_2 = \frac{V_2 + Z_1 I_2}{2\sqrt{Z_1}}$$

where Z_0 and Z_1 are the characteristic impedances of port 1 and port 2. The port 2 characteristic impedance can be written in terms of port 1 characteristic impedance by a factorized manner, i.e., $Z_1 = nZ_0$. Evaluating the expression leads to the following,

$$a = \frac{V + Z_0 I}{2\sqrt{Z_0}} \qquad b = \frac{V - Z_0 I}{2\sqrt{Z_0}}$$

where

$$V = \begin{bmatrix} V_1 \\ \frac{V_2}{\sqrt{n}} \end{bmatrix}$$

$$I = \begin{bmatrix} I_1 \\ -\sqrt{n} I_2 \end{bmatrix}$$

From the impedance matrix defined above, the matrix can be rewritten as

$$\begin{bmatrix} V_1 \\ \frac{V_2}{\sqrt{2}} \end{bmatrix} = \begin{bmatrix} Z_{11} & \frac{Z_{12}}{\sqrt{n}} \\ \frac{Z_{21}}{\sqrt{n}} & \frac{Z_{22}}{n} \end{bmatrix} \begin{bmatrix} I_1 \\ -\sqrt{n} I_2 \end{bmatrix}$$

$$a = \frac{V + Z_0 I}{2\sqrt{Z_0}} = \frac{(Z' + Z_0 \boldsymbol{I}) I}{2\sqrt{Z_0}}$$

or

$$I = 2\sqrt{Z_0}(Z' + Z_0 \boldsymbol{I})^{-1} a$$

$$b = \frac{V - Z_0 I}{2\sqrt{Z_0}} = \frac{(Z' - Z_0 \boldsymbol{I}) I}{2\sqrt{Z_0}}$$

where $\boldsymbol{I}$ is an identity matrix. By definition **b = S a**. Rewriting the above equation leads for the expression of S parameter matrix being defined as

$$S' = (Z' - Z_0 \boldsymbol{I})(Z' + Z_0 \boldsymbol{I})^{-1}$$

On expanding the equation, it can be found that the coefficients of S'_{12} and S'_{21} are given by

$$S'_{12} = \frac{2\sqrt{n} Z_{12} Z_0}{D'} \qquad S'_{21} = \frac{2\sqrt{n} Z_{21} Z_0}{D'}$$

where

$$D' = Z_{11} Z_{22} + Z_{22} Z_0 + Z_1 Z_{11} + Z_1 Z_0 - Z_{12} Z_{21}$$

which is very similar to the factor derived for the standard configuration of Z_0 characteristic impedance on both ports, given by

$$D = Z_{11} Z_{22} + Z_{22} Z_0 + Z_0 Z_{11} + Z_0^2 - Z_{12} Z_{21}$$

In the readout resonator of qubit, Z_{12} and Z_{22} are large components and hence, the above expression approximates to

$$S'_{12} \approx \sqrt{n} S_{12} \qquad S'_{21} \approx \sqrt{n} S_{21}$$

5.8.2. COUPLING CAPACITANCE ESTIMATE USING 3 PORTS

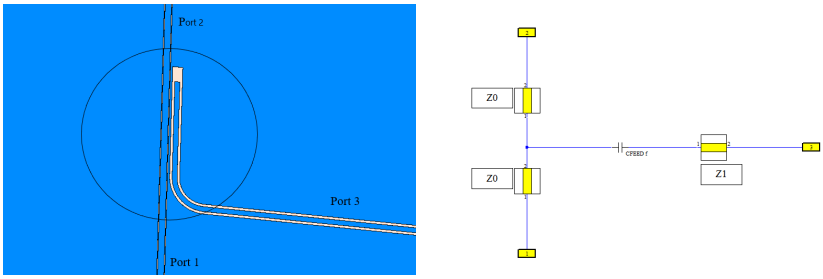

Figure 5.23: Readout resonator coupling with matched characteristic impedance Z_0 on port 1,2 and Z_1 on port 3

The coupling capacitance for the configuration shown in 5.23, can be derived as in the previous section by first converting the three ports into two port configuration. This can be done with terminating the port 2 with Z_0. It can be observed from previously derived equation $S'_{13} \approx \sqrt{n}S_{13}$ and $S'_{31} \approx \sqrt{n}S_{31}$, can be substituted in the previous section's result to obtain the capacitance using S_{31} as

$$C = \frac{S_{31}}{(1 - \frac{3S_{31}}{2\sqrt{n}})i\omega Z_0\sqrt{n}}$$

5.8.3. SIMULATION RESULTS

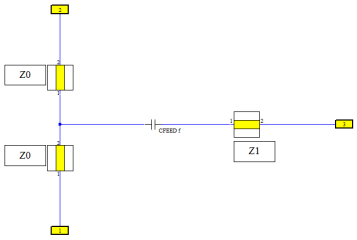

Figure 5.24: Readout resonator coupling circuit simulation setup

The setup used in circuit simulation was a simple hanger connected on the feed line and three ports connected to each ends as shown in 5.24. The S Parameters extracted from the simulation is used to extract the capacitance of the hanger coupling. In table 5.2, the simulation results are tabulated. The values of Z_0 and Z_1 are taken as 50 and 65 Ohm respectively, for the simulation. It can be observed that there is a 14% error on the capacitance extraction in case the normalization derived in the previous section is not considered.

Extracted Capacitance (C) of Hanger Coupling			
Reference capacitance (fF)	C extraction with normalization (fF)	C extraction without normalization (fF)	Error in C estimate without normalization(%)
1	1	1.1402	14.02
2	2.0002	2.2806	14.03
3	3.0004	3.421	14.03
4	4.0006	4.5615	14.04
5	5.001	5.7021	14.04
6	6.0011	6.8429	14.05

Table 5.2: Results of extracted capacitances using circuit simulation model

6

CONCLUSION

Certain parameters of a quantum device can be determined in a classical manner. It can be demonstrated that the physical quantum device can be equivalently modelled in circuit theory and analysis can be done. To extract the parameters, an equivalent FEM model needs to be constructed and the circuit parameters can be extracted. These parameters on extraction can be used to construct lumped element models, using which qubit systems can be analyzed.

Electromagnetic simulations are required to understand and design surface code circuit consisting many qubits and resonators. Within this thesis work, a hybrid simulation approach is investigated which can be very useful to analyze, design and optimize large surface code circuits. Qubit unit cell has complex structures and parasitic couplings which are difficult to be modelled fully with equivalent lumped element circuit simulations. In our hybrid model we used full-wave simulation models for the qubit unit cells and circuit components interconnecting them. As the surface code increases, the size of the qubit system increases which consumes a large amount of computational resources and time for a full wave simulation of the entire chip. Hybrid circuit simulations involving qubit unit cell blocks connected with circuit models of resonators and transmission lines, is scalable and can provide good results for estimating bus resonances in very less computational time. This can be very useful to simulate large systems, which might take considerable computational efforts. The qubit unit cells are precomputed, duplicated in the layout and changes in the circuit models used in the qubit peripherals does not need the qubit unit cells to be re-simulated. This is advantageous in a large qubit system design phase. Although, this simulation cannot provide information such as cross talk between qubits, it can be used to provide useful information such as bus resonances and resonator phase velocity.

An extensive work was done to understand the conditions that can affect the external quality factor or coupling quality factor of the readout resonators. It can be inferred that the coupling quality factor is affected primarily by feed line impedance, the resonator characteristic impedance, the capacitance between the readout resonator and the feed line, and largely independant of the back circuit if the bus resonators are designed at

loaded frequencies higher than the readout resonators (at least 100 MHz). However, the coupling quality factor can also be affected by the back circuit, if the bus resonances come close, but higher than the readout resonators. In this case, the back circuit will allow a leakage of current from the resonator to the feed line via its neighboring resonator circuit and eventually lost in feed line matched circuit. The inter-hanger lengths between the readout resonators will play a role in this case on the Q_c, due to the superposition of the current from the corresponding readout resonator and the current leaked through the back circuit into the feed line from neighboring resonators.

Also, if the qubits operate at a higher frequency than the readout resonators, the qubit circuit can influence the Q_c. Nevertheless, the qubits will not be designed to operate higher than the readout resonators. The impedance mismatch between the hanger feed line and the external measurement circuit will distort the resonant curves on the S parameters output and also affect the Q_c based on the feed line length. This can create a challenge in quality factor design and extraction.

Finally, it can be observed that the capacitance extraction between the hanger feed line and the readout resonators using S parameters depends on the characteristic impedance of both the feed line and the readout resonator. A correction factor needs to be applied to the S parameters in order to extract the capacitance accurately, if there is a difference in the characteristic impedance between the lines.

A

Microwave Estimation of Circuit Parameters

The circuit parameter, coupling capacitance is primarily estimated in this section. Coupling capacitances have an impact on the coupling factor "g" and also on the loaded resonant frequency of the bus resonators. It would be interesting to determine whether the capacitance at DC simulation is also relevant at microwave frequencies. Also, the charging islands are modelled as a transmission line with effective characteristic impedance Z_0 because the CPW structure can support TEM or Quasi TEM mode, although the structure is asymmetric. This can be used to understand the characteristic impedance exhibited by the segment of superconductor. The first step in parameter estimation is to determine the model. The model that is used for the analysis is shown in figure A.1. The extraction is done separately for the upper and lower segments. Ports are placed at the edges of the charging islands and the edge of the bus resonator interface. The ABCD matrix for such a circuitry can be modelled by cascading a transmission line, a Y model, Z model and a Y model. These standard models can be found in [23]. It can be derived that the B parameter be written as,

$$B = jZ_0 \sin\beta l + \frac{1}{j\omega C_C}\cos\beta l$$

where Cc is the coupling capacitance to be extracted. β is the propagation constant of the TEM wave in the charging island segment or the transmission line and l is the length of the line. It should be noted that there is an asymmetry in the structure connected to Port 1 in figure A.1a. We assume to find the effective transmission line solution. By using Taylor series and since the charging island segments are small, one can approximate the sinusoidal signals as

$$\cos\beta l \approx 1 - \frac{\beta l^2}{2} + \frac{\beta l^2}{4!}$$

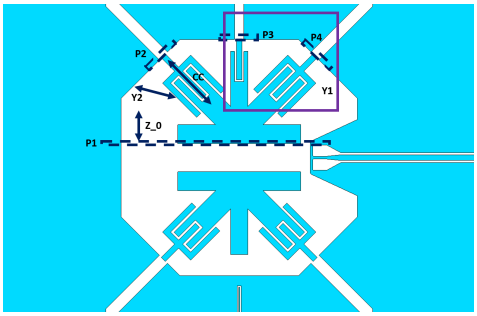

(a)

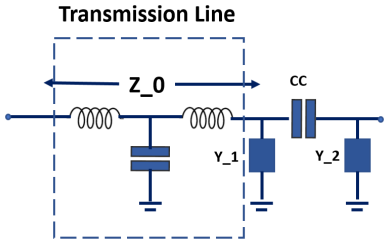

(b)

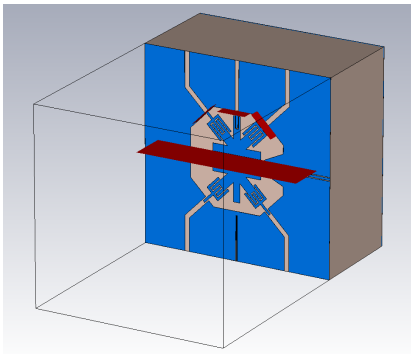

(c)

Figure A.1: Microwave estimation of coupling joints. a. Qubit structure decomposition into impedances. This decomposition is considering the parameters between port 1 (P1) and port 2 (P2). A similar model can be constructed for simulations between port 1, port 3, port 1 and port 4, equivalently. b. Equivalent circuit model for the qubit structure shown in figure A.1a. c. Microwave setup in CST to perform FEM simulation.

$$\sin \beta l \approx \beta l - \frac{\beta l^3}{3!}$$

The charging islands can be considered as an open circuited transmission line. The length l of the open circuited transmission line can be understood as half wavelength, which can be written as $l = \frac{\lambda_r}{2}$. Since a TEM mode is considered to be propagated, the

propagation constant can be written as $\beta = \frac{2\pi}{\lambda}$. The wavelength λ_r can be rewritten as $\lambda_r = \frac{2\pi}{\omega_r\sqrt{L_l C_l}}$. Hence, the product βl can be found as

$$\beta l = \frac{\pi\omega}{\omega_r}$$

On writing out the equation, it can be found that the B parameter can be rewritten as,

$$B' = \Big(\frac{\pi^4}{4!C_C\omega_r} + \frac{Z_0\pi^4}{3!\omega_r}\Big)\omega^4 - \Big(\frac{\pi^2}{2C_C\omega_r} + \frac{Z_0\pi}{\omega_r}\Big)\omega^2 + \frac{1}{C_C}$$

where B' is jωB. This can be solved by constructing a matrix and inverting it. If A is the unknown, and the order of polynomial is ordered in a decreasing order in the equations,

$$WA = B'$$

or

$$A = W^{-1}B'$$

The coupling capacitance can be readily got as

$$C_c = \frac{1}{A(3)}$$

However, the Z_0 and ω_r are unknowns. Using A(1) and A(2), one can write ω_r as a polynomial and solve it. On extracting the roots, one of the root might be the solution that lead to a feasible Z_0.

$$24A(1)C_c\omega_r^4 + 4A(2)\pi^2 C_c\omega_r^2 + 1\pi^4 = 0$$

On finding a solution for ω_r , the effective characteristic impedance can be found to be

$$Z_0 = -\Big(A(2)\frac{\omega_r}{\pi} + \frac{\pi}{2\omega_r C_c}\Big)$$

The mode that is excited on port 1 i.e., at the charging islands is of QTEM of nature, whereas on the bus resonator interface, the mode that is excited is of TEM in nature. Care must be taken to ensure that the port dimensions allow propagation modes to be excited for simulations. It can be noted that the capacitances that is calculated using microwave simulations is approximately the same as the DC simulation case.

A

Qubit Parameter Extraction using Microwave Simulation			
Qubit	Parameter between Nearest Charging Island to Mentioned Component	Capacitance - DC Simulation (fF)	Capacitance - Micro-wave Simulation (fF)
H	CCB1	36.05	36.907
H	CCB2	36.1	36.707
H	CCB3	29.8	29.667
H	CCB4	29.3	29.469
H	CCR	12.59	13.427
L	CCB1	42.9	44.021
L	CCB2	43.06	43.711
L	CCB3	35.6	35.8508
L	CCB4	35.65	35.705
L	CCR	11.05	11.5634
M1	CCB1	33.04	31.555
M1	CCB2	32.83	31.245
M1	CCB3	45.34	42.822
M1	CCB4	45.15	42.509
M1	CCR	11.16	10.855
M2	CCB1	49.66	51.338
M2	CCB2	49.74	50.598
M2	CCB3	24.6	30.445
M2	CCB4	24.66	30.179
M2	CCR	11.07	12.0188

Table A.1: Results of Extracted Capacitances using Microwave Simulation

B

Circuit Analysis of Readout Resonator Qc of a 2 Qubit System

In order to analyze the Q_c of the readout resonator, first an introduction to the nature of a resonant parallel circuit behavior is made. The half wavelength resonator can be modelled as a parallel LC network. Assuming that the losses are very minimal in the superconductor, we restrict to a LC network. From Kirchhoff's current law, the network equations can be written as,

$$\frac{1}{L}\int_0^t v(s)ds + C\frac{\partial v(t)}{\partial t} = 0$$

or

$$\frac{\partial^2 v(t)}{\partial^2 t} + \frac{1}{LC}v(t) = 0$$

On resonance, the frequency can be taken as $\omega_0 = \frac{1}{LC}$.

$$\frac{\partial^2 v(t)}{\partial^2 t} + \omega_0^2 v(t) = 0$$

The solution to such an equation can be given as

$$v(t) = A_1 e^{j\omega_0 t} + A_2 e^{-j\omega_0 t}$$

The above equations convey that the voltage across a parallel LC network is given by a combination of two complex exponentials or a cosine function, if $A_1 = A_2$. Since a half wave length resonator is a open circuited line, this voltage is considered to be at one of the terminals. For a sinusoidal signal, that is is delayed or advanced by half wavelength

corresponds to a phase difference of π, with respect to the reference signal. Hence, the voltage signal at the other end can be represented as

$$v(t) = A_1 e^{j(\omega_0 t - \pi)} + A_2 e^{-j(\omega_0 t + \pi)}$$

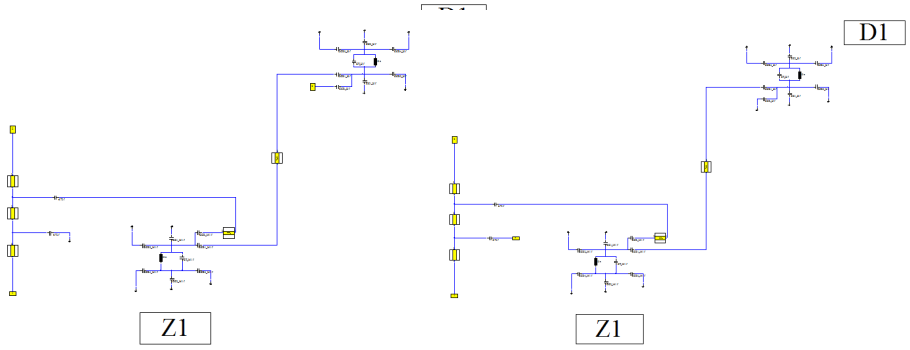

(a) Voltage source at edge 1 represented with S parameter port

(b) Voltage source at edge 2 represented with S parameter port

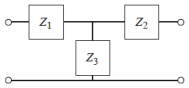

$$A = 1 + \frac{Z_1}{Z_3} \qquad B = Z_1 + Z_2 + \frac{Z_1 Z_2}{Z_3}$$

$$C = \frac{1}{Z_3} \qquad D = 1 + \frac{Z_2}{Z_3}$$

(c) Equivalent impedance model

Figure B.1: Voltage source model of hanger resonators

In order to study the 2 qubit model, with two voltage sources due to the standing wave inside the resonator, a circuit setup is shown in figure B.1, was analyzed in simulation by using S parameters. In order to do so, the resonator is removed and a port is added to one end at a time, while the other end is grounded. This is illustrated in figure B.1a and B.1b. Using S parameters, the equivalent star network as shown in figure B.1c, can be constructed. The star network can be used to determine the currents and power lost in the measurement circuit. Terminating the edge of the hanger in the equivalent star network with the matched impedance, the currents due to the source can be found. This procedure is repeated for the other end of the resonator as well. Then, by using superposition, the power dissipated at the both ends of the hanger is calculated. It can be found that the power loss is given by

$$Power\ Loss = (\frac{I_1 I_1^*}{2} + \frac{I_2 I_2^*}{2} + I_1 I_2^*)$$

Similarly, the same procedure is carried out for the other resonator as well.

Qc Analysis at Bus Resonance 7.8 GHz				
Parameters	7.49GHz 2100um	7.54GHz 2100um	7.49GHz 6300um	7.54GHz 6300um
Current Source 1 P1 (Magnitude) (A)	1.0265e-04	1.06E-004	2.93E-004	3.10E-004
Current Source 1 P2 (A)	2.8820e-04	2.92E-004	3.08E-004	2.93E-004
Current Source 2 P1 (A)	5.3988e-05	1.05E-004	8.25E-005	1.06E-004
Current Source 2 P2 (A)	1.9648e-05	3.72E-005	7.78E-005	1.11E-004
Power Loss (W)	1.8632e-06	3.82E-006	7.24E-006	1.86E-006
Bandwidth (Hz)	3.4400e+05	8.0000e+05	7.4000e+05	2.5700e+05
Theoretical Q from S parameters Q_c	2.1773e+04	9425	1.0122e+04	2.9339e+04
Calculated Q_c	3.3723e+04	1.6448e+04	8.6784e+03	3.3781e+04

Table B.1: Circuit parameters at unloaded bus resonance on 7.8 GHz

Qc Analysis at Bus Resonance 8.8 GHz		
Parameters	7.5091 GHz 6300um	7.5508 GHz 6300um
Current Source 2 P1 (A) (Magnitude)	2.93E-004	3.10E-004
Current Source 2 P2 (A)	3.09E-004	2.93E-004
Current Source 1 P1 (A)	1.18E-005	1.14E-005
Current Source 1 P2 (A)	1.11E-005	1.20E-005
Power Loss (W)	4.8833e-06	4.1963e-06
Bandwidth (Hz)	6.5000e+05	5.7000e+05
Theoretical Q from S parameters	1.1552e+04	1.3247e+04
Calculated Q	1.2867e+04	1.4960e+04

Table B.2: Circuit parameters at unloaded bus resonance on 8.8 GHz

The tables B.1 and B.2 illustrate the calculated currents using circuit theory from the above simulation setup as well as the power losses. P1 and P2 refer to the measurement edges of the hanger circuit or can be called the S parameter ports. It can be observed that at unloaded bus resonance 7.8 GHz, there is a greater influence of edge 2 of the readout resonator. It can be observed that the current leaked per cycle from edge 2 is comparable with edge 1. It can be noted that due to superposition, one of the resonant

curves has a much narrower bandwidth than the other. It can also be noted that the order of current from edge 2 varies by only a factor 10 at 8.8 GHz bus resonance w.r.t 7.8 GHz bus resonance. This explains the reason for the slight asymmetry of the resonance bandwidth observed in the S Parameters for the 8.8 GHz bus resonance condition.

For calculating the Q_c [20], the energy stored in the line can be given as

$$E = \frac{C_l < V >^2}{2}$$

The power loss calculated in the above section is needs to be multiplied by a factor of $\frac{<V>^2}{2}$, if the current was calculated from the resistance with a unit magnitude voltage. This leads to the quality factor to be calculated as

$$Q_c = \frac{C_l < V >^2}{2\, Power Loss}$$

It can be derived for the 1st order resonance of a half wavelength resonator [20],

$$\omega_r C_l = \frac{\pi}{Z_l}$$

This allows the coupling quality factor to be calculated for this analysis to be written as

$$Q_c = \frac{\pi}{Power\ Loss\, Z_l}$$

In the table B.1 and B.2, the Q_c is calculated from S parameters by $\frac{f_r}{3dB\, Bandwidth}$ and compared with the above Q_c relationship calculated with the power loss calculated specifically by the above method.

C

Effect of Impedance Mismatch in the Measurement Circuitry

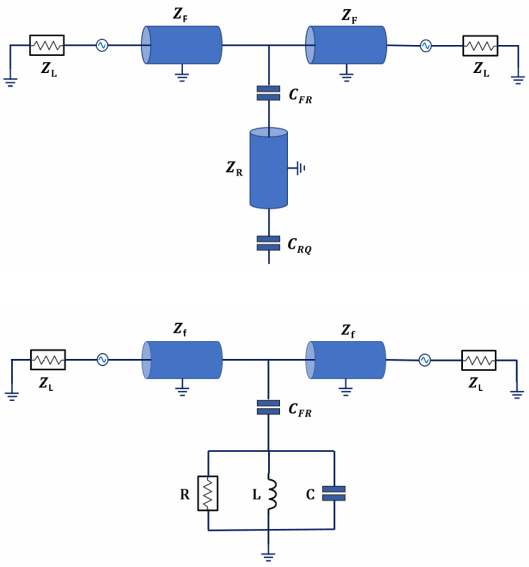

Figure C.1: a. Circuit diagram of a single half wavelength readout resonator on a feed line. b. Equivalent circuitry of a half wavelength readout resonator on a feed line at resonance.

In order to fully understand the effects of feed line mismatch, a investigation into the S parameters of the qubit readout resonator is first treated. A single open circuited transmission line on a feed line, which is typical for a qubit measurement circuitry is shown in figure C.1. Let β be the propagation constant on the feed line, l_1 and l_2 be the feed line

lengths on either side of the resonator. The feed line has a characteristic impedance of Z_f, but the termination is considered to be set at Z_L. This formulation allows an analysis of the case of an impedance mismatch.

The resonator can be replaced by an RLC parallel circuitry at frequencies near the resonance condition. The entire circuit can be analyzed in 2 port cascaded system by considering a cascade connection of a lossless transmission line of length l_1, with a admittance load Y and then a transmission line of length l_2. The ABCD matrix coefficients can be written as

$$A = \cos(\beta l_1)\cos(\beta l_2) + jZ_f \sin(\beta l_1)(Y\cos(\beta l_2) + jY_f \sin(\beta l_2))$$

$$B = Z_f\, j\cos(\beta l_1)\sin(\beta l_2) + jZ_f \sin(\beta l_1)(Y\, jZ_f \sin(\beta l_2) + \cos(\beta l_2))$$

$$C = Y_f\, j\sin(\beta l_1)\cos(\beta l_2) + \cos(\beta l_1)(Y\cos(\beta l_2) + jY_f \sin(\beta l_2))$$

$$D = -\sin(\beta l_1)\sin(\beta l_2) + \cos(\beta l_1)(Y\, jZ_f \sin(\beta l_2) + \cos(\beta l_2))$$

The S_{21} for the equivalent two port network can be written in terms of the ABCD [23] matrix coefficients as follows.

$$S_{21} = \frac{2}{A + B/Z_L + CZ_L + D} \tag{C.1}$$

The factor Z_L in the above equation plays a role in the characteristic of S_{21} response of the circuit. If Z_L is equal to Z_f, then there is perfect matching between the feed line and the measurement circuitry. Before investigating the S_{21} further, the admittance component Y is discussed. The impedance of the resonator near resonance can be written as [13]

$$Z_{LCR} = \left(\frac{1}{j\omega L_n} + j\omega C + \frac{1}{R}\right)^{-1}$$

where the inductive, capacitive and resistive components are given by

$$L = \frac{2L_l l}{n^2\pi^2}$$

$$C = \frac{C_l l}{2}$$

$$R = \frac{Z_l}{\alpha l}$$

where C_l is the capacitance per unit length of the transmission line, L_l is the inductance per unit length, l is the length of the resonator, n is the order of resonance and α is the attenuation constant. Since the resonator is capacitively coupled by C_{FR}, the equivalent admittance can be written as

$$Y = \frac{j\omega C_{FR}\left(\frac{1}{j\omega L_n} + j\omega C + \frac{1}{R}\right)}{\left(\frac{1}{j\omega L_n} + j\omega C + j\omega C_{FR} + \frac{1}{R}\right)}$$

The admittance at resonance tends to infinity for a lossless circuit since $R \to \infty$ for a lossless line and the terms $\frac{1}{j\omega L_n} + j\omega C + j\omega C_{FR}$ becomes zero. This condition for resonance is valid as long as the imaginary components arising in the impedance of the measurement line due to the mismatch is negligible. However, the admittance at frequencies further away from the resonance tends to zero because of the large impedance offered by the low capacitively coupled open circuited transmission line. The S_{21} can be written as

$$S_{21} = \frac{2}{2\cos(\beta l_1 + \beta l_2) + (\frac{Z_f}{Z_L} + \frac{Z_L}{Z_f})\, j \sin(\beta l_1 + \beta l_2) + Y_{fact}} \tag{C.2}$$

$$Y_{fact} = Y\left(j Z_f \sin(\beta l_1)\cos(\beta l_2) - \frac{Z_f^2}{Z_L}\sin(\beta l_1)\sin(\beta l_2) + Z_L \cos(\beta l_1)\cos(\beta l_2) + j Z_f \cos(\beta l_1)\sin(\beta l_2)\right)$$

In case of a perfect match between the feed line and the measurement circuitry, the S_{21} can be written as

$$S_{21} = \frac{2}{2\cos(\beta l_1 + \beta l_2) + 2j\sin(\beta l_1 + \beta l_2) + Z_L Y(\cos(\beta l_1 + \beta l_2) + j\sin(\beta l_1 + \beta l_2))} \tag{C.3}$$

REFERENCES

[1] Dickel, Christian
http://blog.qutech.nl/index.php/2017/08/13/how-to-make-artificial-atoms-out-of-electrical-

[2] L.M.K.Vandersypen,M.Steffen,G.Breyta,C.S.Yannoni,M.H.Sherwood,and I.L.Chuang *Experimental realization of Shor's quantum factoring algorithm using nuclear magnetic resonance*
Nature 414, 883-887 (2001)

[3] L. DiCarlo, J. M. Chow, J. M. Gambetta, Lev S. Bishop, B. R. Johnson, D. I. Schuster, J. Majer, A. Blais, L. Frunzio, S. M. Girvin, R. J. Schoelkopf *Demonstration of Two-Qubit Algorithms with a Superconducting Quantum Processor*
Nature volume 460, pages 240-244 (09 July 2009)

[4] Jens Koch, Terri M. Yu, Jay Gambetta, A. A. Houck, D. I. Schuster, J. Majer, Alexandre Blais, M. H. Devoret, S. M. Girvin, and R. J. Schoelkopf
Charge insensitive qubit design derived from the Cooper pair box
Phys. Rev. A 76, 042319, 12 October 2007
https://arxiv.org/abs/cond-mat/0703002v2,Accessed:21-8-2018

[5] J. Majer, J. M. Chow, J. M. Gambetta, Jens Koch, B. R. Johnson, J. A. Schreier, L. Frunzio, D. I. Schuster, A. A. Houck, A. Wallraff, A. Blais, M. H. Devoret, S. M. Girvin and R. J. Schoelkopf
Coupling superconducting qubits via a cavity bus
Nature volume 449, pages 443-447 (27 September 2007)
https://arxiv.org/abs/0709.2135

[6] N. Haider *Design and analysis of superconducting qubits for extensible surface coding*

[7] Martinis,John M. and Osborne,Kevin *Superconducting Qubits and the Physics of Josephson Junctions*
https://web.physics.ucsb.edu/ martinisgroup/classnotes/finland/LesHouchesJu
Accessed:21-8-2018

[8] Blomgren, Jakob (1998), Rev. Magnelind, Per(2005) *The Josephson Effect*
http://fy.chalmers.se/ delsing/LowTemp/Labbar/SQUIDlab-rev3.pdf

[9] Devoret M. H., Wallraff A. and Martinis J. M. *Superconducting Qubits: A Short Review*
https://qudev.phys.ethz.ch/content/courses/ASC04_SCqubits_Review.pdf,
Accessed:1-8-2018

[10] J. Clarke, A. I. Braginski (Eds.) *The SQUID Handbook. Vol. I Fundamentals and Technology of SQUIDs and SQUID Systems.*
2004, ISBN 3-527-40229-2

[11] Oliver, William D. *Superconducting Qubits Quantum Information Processing: Lecture Notes of the 44th IFF Spring School 2013, Ed: David P. DiVincenzo, Juelich, 2013*
http://equs.mit.edu/wp-content/uploads/2016/11/SC_qubits_Oliver_IFF_Spring_Scho
Accessed:1-8-2018

[12] Gershenfeld, Neil *Circuits, Transmission Lines, and Waveguides*
http://fab.cba.mit.edu/classes/862.16/notes/circuits.pdf:Accessed:5-10-2018

C

[13] M. Göppl,A. Fragner, M. Baur, R. Bianchetti, S. Filipp, J. M. Fink, P. J. Leek, G. Puebla, L. Steffen, and A. Wallraff *Coplanar waveguide resonators for circuit quantum electrodynamics*
JOURNAL OF APPLIED PHYSICS 104, 113904, 2008

[14] Mattis,D. C. and Bardeen, J. *Theory of the anomalous skin effect in normal and superconducting metals*
Phys. Rev., vol. 111, pp. 412-417, 1958.

[15] Mei, Kenneth K. and Liang, Guo-chun *Electromagnetics of Superconductors*
IEEE Transactions on Microwave Theory and Techniques (Volume: 39, Issue: 9, Sep 1991)

[16] Gao, Jiansong *The physics of superconducting microwave resonators*
https://thesis.library.caltech.edu/2530/, Accessed:20-11-2017

[17] Rainee N. Simons *Coplanar Waveguide Circuits, Components, and Systems.*
ISBN: 0-471-16121-7

[18] Watanabe, Koki et. al. *Kinetic Inductance of Superconducting Coplanar Waveguides*
Jpn. J. Appl. Phys. Vol 33 (1994) pp 5708-5712

[19] Beekman, Mark *Superconducting Transmon Qubit Chip Design and Characterization through Electromagnetic Analysis*
TU Delft Master Thesis

[20] Mazin, Benjamin A. *Microwave kinetic inductance detectors*
https://thesis.library.caltech.edu/3910/, Accessed:2-02-2018

[21] Devoret, Michel *Josephson Qubit Circuits And Their Readout*
http://qulab.eng.yale.edu/documents/talks/Devoret-APS_Tutorial_090316s.pdf, Accessed:8-06-2018

[22] Johnson, Jedediah Edward Jensen *Optimization of superconducting flux qubit readout using near-quantum-limited-amplifiers*
http://digitalassets.lib.berkeley.edu/etd/ucb/text/Johnson_berkeley_0028E_12597
Accessed:8-06-2018

[23] Pozar, David M. *Microwave Engineering*
Fourth Edition, ISBN 978-0-470-63155-3

[24] Orfanidis, Sophocles J. *S Parameters*
http://www.ece.rutgers.edu/ orfanidi/ewa/ch14.pdf,
Accessed:12-02-2018

[25] *Parallel LC*
http://mlg.eng.cam.ac.uk/mchutchon/ResonantCircuits.pdf,
Accessed:21-05-2018

[26] Fowler,Austin G., et all
Surface codes: Towards practical large-scale quantum computation

[27] Steen, Maikel van der
Modeling and characterization of superconducting coplanar
waveguide resonators for circuit QED. Bachelor Thesis, 28-07-2011